Technische Universität München
TUM School of Engineering and Design

Efficient Simulation of Flame Acceleration and Deflagration-to-Detonation Transition in Smooth Geometries

Christoph Herbert Wieland

Vollständiger Abdruck der von der TUM School of Engineering and Design der Technischen Universität München zur Erlangung des akademischen Grades eines

DOKTORS DER INGENIEURWISSENSCHAFTEN

genehmigten Dissertation.

Vorsitzender:
Prof. Dr.-Ing. Harald Klein
Prüfer der Dissertation:
Prof. Dr.-Ing. Thomas Sattelmayer
Prof. Dr.-Ing. habil. Markus Klein

Die Dissertation wurde am 06.12.2021 bei der Technischen Universität München eingereicht und durch die TUM School of Engineering and Design am 08.04.2022 angenommen.

Für Herbert

Vorwort

Diese Arbeit entstand in den Jahren 2018 bis 2021 im Rahmen meiner Tätigkeit als wissenschaftlicher Mitarbeiter am Lehrstuhl für Thermodynamik der Technischen Universität München. Sie wurde von der BASF gefördert.

Mein besonderer Dank gilt meinem Doktorvater Herrn Prof. Dr.-Ing. Thomas Sattelmayer für die Möglichkeit unter seiner Betreuung promovieren zu dürfen. Sein Input inspirierte mich stets zur Entwicklung und Umsetzung neuer Ideen, die maßgeblich zum Erfolg dieser Arbeit beigetragen haben. Ich bedanke mich auch für die mir gestatteten Freiräume, in denen ich mich während der Promotion weiterentwickeln konnte.

Herrn Professor Dr.-Ing. habil. Markus Klein danke ich für die freundliche Übernahme des Koreferates und Herrn Professor Dr.-Ing. Harald Klein für den Vorsitz bei der mündlichen Prüfung.

Den betreuenden Kollegen von BASF möchte ich ganz besonders für die stets sehr angenehme Atmosphäre und die produktiven Diskussionen danken, die maßgeblich zum Erfolg dieser Arbeit beigetragen haben. Hierbei sind vor allem Dr.-Ing Vera Hoferichter, Dr.-Ing Stefan Lipp, Dr.-Ing Florian Scharf und Dr. Hans-Peter Schildberg zu nennen.

Dr.-Ing. Christoph Hirsch möchte ich dafür danken, dass er nie den Glauben an einen erfolgreichen Projektabschluss aufgegeben hat und mir dafür immer wieder neue Denkanstöße gegeben hat.

Ein ganz besonderer Dank geht auch an meine Kolleginnen und Kollegen für die tolle Zeit am Lehrstuhl. Viele von ihnen zu Freunden geworden. Durch unzählige fachliche Diskussionen, Treffen und Partys in und außerhalb des Lehrstuhls habt ihr meine Zeit am Lehrstuhl unvergesslich gemacht. Ich möchte an dieser Stelle besonders der DDT Gruppe danken, die durch unzählige fachliche Diskussionen zum Erfolg dieser Arbeit beigetragen hat. Frau Helga Bassett und Frau Sigrid Schulz-Reichwald danke ich für die Unterstützung bei sämtlichen organisatorischen Angelegenheiten.

Dr.-Ing. Thomas Hofmeister, Daniel Heilbronn und Simon Tartsch danke ich

für das Korrigieren dieser Dissertation, wodurch die Qualität noch einmal deutlich gesteigert wurde.

Weiterhin danke ich den Studenten und wissenschaftlichen Hilfskräften für ihren Einsatz und die Unterstützung. Besonders hervorheben möchte ich hierbei Anik Shah, der mich über einen langen Zeitraum tatkräftig unterstützt hat.

Jonas Nitzler und Jannik Petermann gebührt ebenfalls ein besonderer Dank. Ohne eure Unterstützung und Motivation während unserer langen gemeinsamen Reise durch Studium und Promotion wäre ich nicht so weit gekommen.

Liebe Lina, du hast mich immer unterstützt und auch in schwierigen Zeiten an mich geglaubt. Dafür danke ich Dir von ganzem Herzen!

Zuletzt bedanke ich mich bei meiner Familie, die mir immer zur Seite steht. Ihr habt mir über all die Jahre eure bedingungslose Unterstützung zukommen lassen. Euch habe ich alles zu verdanken!

München, im Mai 2022 Christoph Wieland

Kurzfassung

Die Risikoanalyse möglicher Unfallszenarien mit Flammenbeschleunigung und Deflagrations-Detonations-Übergang (DDT) ist ein zentraler Aspekt in der chemischen und verfahrenstechnischen Industrie. Die große Vielfalt an Prozessbedingungen lässt keine umfassenden experimentellen Untersuchungen zu, was den Bedarf für ein effizientes numerisches Verfahren schafft. In dieser Arbeit wird ein hybrider druck-/ dichte-basierter Solver vorgestellt, der sowohl die deflagrative Flammenbeschleunigung als auch den DDT und die Detonationsausbreitung nach einer schwachen Zündung simulieren kann. Dieser Solver basiert auf den Arbeiten von Ettner [43] und Hasslberger [62] und verwendet unteraufgelöste Gitter in Kombination mit einem Reaktionsfortschrittsvariablen Ansatz, um die Rechenzeiten zu minimieren. Für die Simulation der initialen inkompressiblen Beschleunigungsphase wird der druckbasierte Solver verwendet, bis die Flamme das kompressible Regime der schnellen Flammen und der Übergang zum dichtebasierten Solver erfolgt. Das Verbrennungsmodell enthält einen Deflagrationsquellterm, welcher mittels einer turbulenten Flammengeschwindigkeit (TFC) geschlossen wird. Der Detonationsquellterm beruht auf einer quadratischen Wärmefreisetzungsfunktion. Die Validierung des vorgestellten numerischen Ansatzes erfolgt anhand von experimentell bestimmten DDT-Positionen und Druckdaten für stöchiometrische $H_2/O_2/N_2$ und $C_2H_4/O_2/N_2$ Gemische in glatten Rohren und einer 20 l Kugel. Der Schwerpunkt der aktuellen Untersuchungen liegt auf der korrekten Vorhersage des globalen Flammenausbreitungsverhaltens, der DDT-Position und der Identifikation kritischer Bedingungen für das Auftreten einer Detonation. Für die im Rahmen dieser Arbeit betrachteten Fälle wird eine gute Übereinstimmung beobachtet. Darüber hinaus können wesentliche Aspekte der Flammenausbreitung, wie die Bildung einer tulpenförmigen Flamme, im Rahmen der unteraufgelösten Gitter reproduziert werden.

Abstract

Risk analysis of potential accident scenarios involving flame acceleration and deflagration-to-detonation transition (DDT) is a central aspect in chemical and process engineering. The large variety of process conditions does not allow for comprehensive experimental investigations, which increases the need for an efficient numerical simulation tool. In this work, a hybrid pressure-/density-based solver is presented, which is capable of simulating deflagrative flame acceleration as well as DDT and detonation propagation after a weak ignition. This solver is based on the works of Ettner [43] and Hasslberger [62] and uses under-resolved grids in combination with a reaction progress variable approach in order to minimise the computational costs. For the simulation of the initial incompressible acceleration stage, the pressure-based solver is used until the flame velocity reaches the compressible regime of fast flames and transition to the density-based solver is realised. The combustion model incorporates a deflagration source term, formulated in terms of a turbulent flame speed closure (TFC) model. The detonation source term is based on a quadratic heat release function. Validation of the presented numerical approach is carried out by means of experimental DDT locations and pressure data for stoichiometric $H_2/O_2/N_2$ and $C_2H_4/O_2/N_2$ mixtures in smooth pipes and a 20 l sphere. The focus of the current investigations is to correctly predict the global flame propagation behaviour, the DDT location and to identify critical conditions for the onset of a detonation. Good agreement is observed for the cases considered in this thesis. In addition, essential aspects of flame propagation like the tulip flame formation can be reproduced within the framework of under-resolved grids.

Contents

List of Figures

List of Tables

Nomenclature

Latin letters

a	Speed of sound [m/s]
a	Thermal diffusivity [m^2/s]
A	Material specific sutherland coefficient [$kg/msK^{0.5}$]
c	Reaction progress variable [-]
c_p	Specific heat capacity [J/kg-K]
C	Model constant [-]
D	Detonation velocity [m/s]
D	Diffusion coefficient [m^2/s]
e	Specific internal energy [J/kg]
E_A	Activation energy [J]
F	Burning velocity model parameter [-]
F	Convective flux [m^3/s]
G	Quenching factor [-]
g	Quenching rate [1/s]
g	Gravitational acceleration [m/s^2]
H	Heaviside function [-]
h	Specific enthalpy [J/kg]
k	Specific turbulent kinetic energy [m^2/s^2]
K	Flame stretch [1/s]
l	Length scale [m]
m	Mass [kg]
M	Molar mass [kg/kmol]
n	Count variable [-]
N	Count variable [-]

p	Pressure [N/m^2]
q	Specific heat [J/kg]
q	Diffusive flux [W/m^2]
Q	Dimensionless heat [-]
R	Specific gas constant [J/kgK]
S	Burning velocity [m/s]
t	Time [s]
T	Temperature [K]
u	Flow velocity [m/s]
v	Flame-tip velocity [m/s]
x, y, z	Cartesian coordinates [m]
X	Mole fraction [-]
Y	Mass fraction [-]
y	Wall distance [m]
y^+	Dimensionless wall distance [-]

Greek letters

α	Temperature coefficient laminar flame speed [-]
α	Model parameter transition criterion [-]
β	Pressure coefficient laminar flame speed [-]
Γ	Pseudo diffusivity [kg/ms]
δ_{ij}	Kronecker delta [-]
ϵ	Dissipation rate of turbulent kinetic energy [J/kgs]
θ	Pressure criterion [-]
Θ	Thermicity [1/s]
κ	Curvature [1/m]
κ	Isentropic coefficient [-]
λ	Heat condictivity [W/mK]
λ	Detonation cell width [m]
μ	Dynamic viscosity [kg/ms]
ν	Kinematic viscosity [m^2/s]
ξ	Weighting factor [-]

Ξ	Flame wrinkling factor [-]
σ	Expansion ratio [-]
σ	Standard deviation [-]
τ	Viscous stress [N/m^2]
τ	Auto-ignition precursor [-]
τ	Transition time [s]
ϕ	Equivalence ratio [-]
ϕ	General variable [-]
ψ	General variable [-]
Ω	Computational domain [-]
$\dot{\omega}$	Source term [kg/m^{3}s]
ω	Angular eddy frequency [1/s]

Superscripts

’	Fluctuation (Reynolds decomposition)
”	Fluctuation (Favre decomposition)
f	Formation
s	Sensible
T	Transposed

Subscripts

0	Initial
1	Pre-reaction
2	Post-reaction
AICC	Adiabatic isochoric complete combustion
b	Burnt
C_2H_4	Ethylene
CJ	Chapman-Jouguet
cr	Critical
def	Deflagration
det	Detonation
e	Educts

E	Excess
eff	Effective
eq	Equilibrium
D	Deficient
f	Face
H_2	Hydrogen
ign	Ignition
inst	Instability
L	Laminar
p	Isobar
pr	Products
ref	Reference
s	Sutherland
t	Total
T	Turbulent
Tay	Taylor
trans	Transition
u	Unburnt
vN	Von Neumann
x,y,z	Cartesian coordinates
δ	Reaction zone
η	Kolmogorov
ω	Eddy frequency
$\perp$	Orthogonally projected

Dimensionless numbers

CFL	Courant-Friedrichs-Lewy
Ka	Karlovitz
Le	Lewis
Ma	Mach
Pr	Prandtl
Re	Reynolds
Sc	Schmidt
Ze	Zeldovich

Abbreviations

0-D	Zero-dimensional
1-D	One-dimensional
3-D	Three-dimensional
AMR	Adaptive Mesh Refinement
BASF	Badische Anilin- und Sodafabrik
CEA	Atomic Energy and Alternative Energies Commission
CFD	Computational Fluid Dynamics
C_2H_4	Ethylene
CJ	Chapman-Jouguet
EBU	Eddy-Breakup model
EDC	Eddy-Dissipation Concept model
EDM	Eddy-Dissipation model
DDT	Deflagration-to-Detonation Transition
DNS	Direct Numerical Simulation
FVM	Finite Volume Method
H_2	Hydrogen
HLLC	Harten-Lax-van Leer Contact
KIT	Karlsruhe Institute of Technology
LD	Landau-Darrieus instability
LES	Large Eddy Simulation
N_2	Nitrogen
NASA	National Aeronautics and Space Administration
NIST	National Institute of Standards and Technology
O_2	Oxygen
OpenFOAM	Open Field Operation and Manipulation
PASR	Partially-Stirred-Reactor
PDF	Probability Density Function
PIMPLE	Pressure-Implicit Method for Pressure-Linked Equations
PISO	Pressure Implicit with Splitting of Operators
PSR	Perfectly-Stirred Reactor
RANS	Reynolds-Averaged Navier-Stokes
SIMPLE	Semi-Implicit Method for Pressure-Linked Equations
SST	Shear Stress Transport

SWACER	Shock Wave Amplification by Coherent Energy Release
TD	Thermal-diffusive instability
TFC	Turbulent Flame Speed Closure
URANS	Unsteady Reynolds-Averaged Navier-Stokes
ZND	Zeldovich-von Neumann-Döring

1 Introduction

1.1 Motivation

The chemical industry and process engineering represent one of the most important industry branches. In Germany alone, there are 25 chemical parks, employing more than 300.000 people [24], [50]. Within these parks, a wide variety of plants and processing steps exists, based on the matters involved and the resulting products.

Minor and serious accidents occur occasionally due to the use of highly sensitive combustible mixtures in many of the processing steps, which is one of the major challenges for plant design. Fig. 1.1 depicts the number of reportable incidents in Germany during the last 20 years, documented by the Umweltbundesamt [134]. On average, around 20 incidents happen per year in Germany, among which are also frequently serious explosion accidents as for example at BASF in 1921 [82], in 1948 [124] and in 2016 [123]. Also recently, an accident occurred at the Chempark Leverkusen in 2021 [152]. Furthermore, viewed globally, a strong detonation induced by chemicals appeared at the harbour in Beirut in 2020 [19]. Each accident caused numerous deaths and injuries. In addition, the surrounding area has been extensively destroyed. That explains why safety-related research and risk assessment are crucial aspects during the design process in order to protect the employees and the environment from the release of toxic substances. Moreover, from an economic perspective, cost-intensive production losses should be avoided.

The hazard potential for severe explosion accidents results from the use of gaseous mixtures which are within the explosive or even the detonative range.

Exemplary fuel mixtures such as hydrogen (H_2)/air or ethylene (C_2H_4)/air are

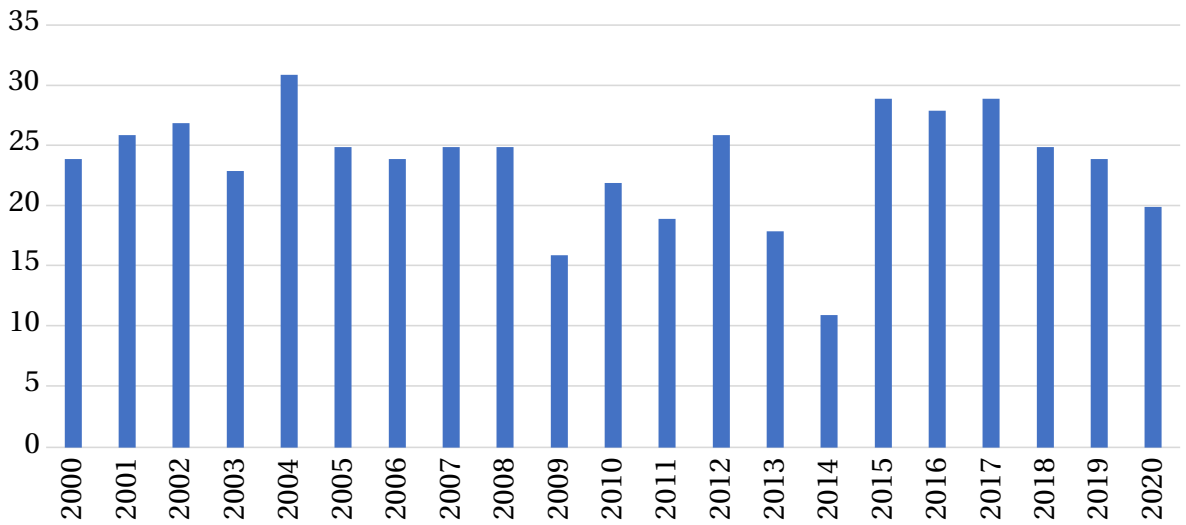

Figure 1.1: Reportable incidents in chemical and process industry plants (reproduced from [134]).

used. In that context, the possibility for effective ignition sources to occur in the plants poses a great threat for the employees in case of an accident. Therefore, analysis of flame acceleration, explosion processes and the hazardous deflagration-to-detonation transition (DDT) in particular is an important research aspect in chemical and process engineering. Corresponding investigations are carried out by means of experiments and theoretical methods [114], [115], [116]. However, the wide variety of mixtures, geometries and process conditions does not allow for a broadband experimental investigation of whether a DDT can be expected in a given plant section. Thus, risk analysis has to rely on reference experiments and best practice estimation methods to assess the DDT risk in the individual case. Hence, the methods shall be extended by means of Computational Fluid Dynamics (CFD) simulations to be able to reduce the amount of resource intense experiments and examine more potential accident scenarios.

Taking a closer look at the individual components of the plants, smooth pipe-like, cylindrical or spherical vessels can be considered as abstracted geometries of typical reactors and piping systems. For reasons of cost, provisions and protections against unwanted flame propagation and detonations [13], [22], [86] should be avoided if possible. Hence, the prediction of conditions critical for DDT and the detonation locations is a crucial aspect of safety engineering.

1.2 Problem Statement

The process of flame acceleration in a smooth pipe-like geometry after a so-called weak ignition, which may result in the hazardous DDT, is illustrated in Fig. 1.2. Initially, laminar flame propagation evolves, inducing a flow field and boundary layer ahead of the flame through the emitted pressure waves. Due to thermal expansion of the reaction products, a positive feedback loop, promoting flame acceleration, establishes. As a result of intrinsic flame instabilities like the Landau-Darrieus (LD) and thermal-diffusive (TD) instability, flame and flow velocities increase during the early acceleration stage. With increasing flame and flow velocities, transition from laminar to turbulent flow field occurs. Preconditioning of the fresh gas and turbulence-chemistry interaction in terms of turbulent flame wrinkling further intensify flame acceleration. In this early phase, most of the turbulence results from the boundary layer in smooth geometries.

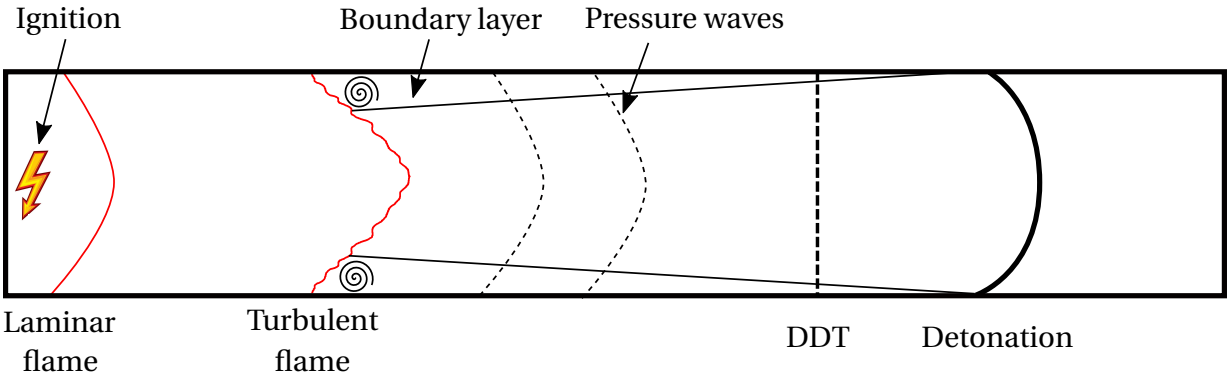

Figure 1.2: Schematic of flame acceleration in a smooth pipe.

During the subsequent regime of turbulent flame propagation, turbulence production in the bulk flow is enhanced through reflected pressure waves and the creation of shear layers close to the flame front. The associated strong flame acceleration can produce conditions critical for the onset of a detonation [86]. In addition, the faster the flame front propagates, the more important gas dynamic effects and the associated preconditioning of the fresh gas become due to accumulating pressure waves [25].

DDT itself is a complex phenomenon depending on several influencing pa-

rameters. The interaction of the turbulent flow field with the flame front as well as preconditioning due to gas dynamics determine whether significant auto-ignition effects start to take place and critical conditions for the onset are satisfied. Due to the number of involved physical processes and their complex interaction, this phenomenon exhibits a stochastic character [69].

In conclusion, evaluation whether DDT will occur is an extremely demanding issue for safety-related research due to the large number of individual phenomena involved. A more detailed explanation of flame acceleration and DDT will be given in Sec. 2.2. Two main criteria for the onset of a DDT have been defined from various experiments, including different geometries and dimensions. The so-called σ-criterion (Eq. 2.12) evaluates whether critical flame acceleration is achieved. A required precondition for DDT refers to the flame velocity which must reach a value in the order of the speed of sound of the reaction products a_{pr}. A second criterion, the so-called λ-criterion (Eq. 2.14), evaluates the likelihood of DDT to take place, if critical conditions are satisfied. However, both criteria have a limited range of validity and are therefore not generally applicable, considering the many mixtures and geometries involved in chemical processes. Hence, there exist various uncertainties regarding the evaluation of DDT in differing geometries and scales, which is why these criteria should not be used exclusively.

Due to the large dimensions of chemical plants, experiments to extend the range of applicability of these criteria are expensive and time consuming. Furthermore, rather simple geometrical configurations have to be used in most cases, having a limited validity for more complex geometries [43]. Another drawback of the λ-criterion concerns its ability to only predict the possibility of a DDT. No further information, neither on the location of the DDT nor on the occurring pressure loads can be derived. That is why an efficient and robust CFD solver for industrial application, capable of simulating the process of flame acceleration and DDT after weak ignition, shall be developed in this work. For that purpose, representative geometries of chemical plants are considered.

Direct initiation of detonation (strong ignition) is not a typical accident scenario in chemical plants as the required ignition energy is typically too large

and not provided by the occurring ignition sources. Thus, this scenario is not further considered in this thesis.

CFD simulations have been successfully established as a tool for safety analysis, particularly in the context of nuclear safety analysis [18]. For this purpose, Ettner [43] and Hasslberger [62] developed an OpenFOAM-based [141] solver which is capable of simulating the whole process of flame acceleration, DDT and stable detonation propagation on laboratory and industry-scale. For that purpose, under-resolved grids are used which allows large scale geometries to be simulated with reasonable computational costs. The focus of their investigations has been to correctly predict the global flame propagation behaviour and the DDT location. As both projects have been related to nuclear safety, only obstacle-laden geometries have been analysed. Hence, the turbulence level in the simulation domain increases strongly at an early stage due to the interaction of pressure waves with the obstacles. As a consequence, strong flame acceleration evolves. The numerical modelling accordingly concentrated on the fast flame regime.

Similar to Ettner [43] and Hasslberger [62], the objective of this work is to correctly predict the global flame propagation behaviour and the DDT location in smooth industrial-scale geometries without capturing all small-scale phenomena in the framework of under-resolved grids. On the contrary, in literature typically highly resolved simulations in smooth small-scale pipes or channels are carried out to study individual phenomena of the DDT process. Ivanov [69], [70] executed simulations of a stoichiometric H_2/O_2 mixture in smooth rectangular channels in order to study the influence of the channel dimension on flame acceleration. Han [59], [60] analysed the impact of the channel dimension on DDT for a stoichiomemtric C_2H_4/O_2 mixture in smooth rectangular channels of varying size. However, due to the limitation of this approach to small geometries and the large simulation runtimes, this method is not feasible for the current work.

Within this thesis, investigations on flame acceleration and DDT for stoichiometric $H_2/O_2/N_2$ and $C_2H_4/O_2/N_2$ mixtures in smooth geometries are carried out. As a chemical plant consists of various components, smooth pipes of varying size and a 20 l sphere are considered. Therefore, two different types

of flame propagation: quasi 1-D propagation in the smooth pipes and 3-D propagation in the spheres are used for the validation of the solver. Usage of smooth geometries implies a significantly lower level of turbulence during the early acceleration phase, slowing down flame acceleration. Thus, modelling of the incompressible stage of slow to medium fast flames becomes crucial. Simulation of this incompressible phase is accompanied by an accurate reproduction of the pressure rise ahead of the flame and turbulence creation in the boundary layer, being the main source of turbulence production in smooth geometries at this stage. Since the purely density-based solver architecture [62] shows deficits at computing slow flame propagation, a hybrid pressure-/ density-based approach to capture deflagrative flame acceleration is chosen for the current work. Moreover, compared to nuclear safety applications, only stoichiometric fuel-oxidizer mixtures are analysed, to focus on particularly safety-critical cases. This implies adjustment of detonation modelling [62] to the increased reactivity of the mixtures (Sec. 3.5.2).

1.3 Thesis Outline

After specifying the motivation, the problem statement and the goal of this thesis in the context of safety-related research in chemical and process engineering, chapter 2 introduces the fundamentals of combustion, turbulence-chemistry interaction and explosion processes. Solely the aspects required for understanding the modelling approach are outlined. Chapter 3 initially presents the simulation challenges and provides an overview on existing industrial-scale DDT solvers. In section 3.3, the fundamental governing equations are presented, followed by an explanation of the hybrid solver architecture, and the transition criterion between the two solution methods. This chapter closes by depicting the combustion model, starting with the modelling of the deflagration source term for H_2 and C_2H_4 mixtures. The essential difference refers to the calculation of the effective burning velocity S_{eff}. Subsequently, modelling of the detonation source term, based on the quadratic heat release function from Hasslberger [62], is described with a focus on its specific timescale. Some methodological aspects from Ettner [43] and Hasslberger [62]

are only briefly summarised, being elaborated in detail in their respective thesis. Chapter 4 covers the validation of the developed DDT solver in smooth pipes and a 20 l sphere for stoichiometric H_2 and C_2H_4 mixtures. The experimental validation data covers a broad range of initial conditions. A summary and some topics for further solver development are given in chapter 5.

2 Explosion Fundamentals

Flame acceleration and DDT have been studied for many years and several advances have been made in their understanding, published for example by Dorofeev [25]. The associated phenomena inherit two types of combustion: deflagration and detonation. Regarding deflagration, the propagation of the flame front results from the exchange of heat and species/radicals between reactants and products. In contrast, a detonation is driven by auto-ignition effects, initiated by shock compression of the fresh gas above the auto-ignition temperature. No further transport and mixing processes are required. Due to the incorporated shock wave, detonation propagation is solely possible at supersonic speed. The partly empirical and theoretical knowledge on these two combustion processes, turbulence-chemistry-interaction, flame acceleration, DDT and detonations will be reviewed in the following.

2.1 Laminar and Turbulent Burning Characteristics

Weak ignition of a combustible mixture is initially followed by laminar flame propagation. This phase is characterised by the laminar flame speed S_L, which is one of the fundamental thermodynamic combustion characteristics. It determines the velocity at which an unstretched laminar flame propagates with respect to the incoming fresh gas flow [133]. S_L can be derived experimentally or i.e. from Cantera [57] simulations with appropriate reaction mechanisms. Within the scope of this thesis, polynomial expressions (Eqs. 3.59, 3.61, 3.63, 3.65), based on experimental data and Cantera [57] calculations, are used.

A characteristic laminar length scale, the laminar flame thickness l_L, is obtained from dimensional analysis [89]

$$l_\mathrm{L} = \frac{a_\mathrm{u}}{{S_\mathrm{L}}^2}, \tag{2.1}$$

where a_u is the unburnt thermal diffusivity. l_L extends over the preheat and the reaction zone [126]. Combining S_L and l_L yields a timescale of laminar combustion t_L [89]

$$t_\mathrm{L} = \frac{l_\mathrm{L}}{S_\mathrm{L}}. \tag{2.2}$$

A propagating flame initiates a gas flow ahead by emitting pressure waves. Classification of the flow as laminar or turbulent is realised using the Reynolds number Re, given by [109]

$$\mathrm{Re} = \frac{u\,l}{\nu}. \tag{2.3}$$

This quantity describes the ratio of inertia and friction forces by means of the flow velocity u, a characteristic length scale l, i.e. the pipe diameter, and the kinematic viscosity ν. If a problem-specific value of Re is exceeded, laminar-turbulent transition takes place. Turbulent flow is characterised by vortices of various size and an irregular, anisotropic, chaotic and unsteady nature. According to Reynolds-averaging (Eq. 3.14), the turbulent velocity is divided into an average velocity $\overline{u}$ and the so-called turbulent velocity fluctuations u' [109].

Assuming isotropic turbulence, u' can be calculated from the turbulent kinetic energy k (Eq. 3.26) [109]

$$u' = \sqrt{\frac{2}{3}k}, \tag{2.4}$$

which represents the total amount of energy contained in the full spectrum of turbulent structures. k is produced at the largest scales of motion and transferred to the smaller scales within the energy cascade. At the smallest scales, k is dissipated into internal energy by viscous forces [109].

The largest vortices are characterised by the length scale l_T [109]

$$l_T = \frac{u'^3}{\epsilon}, \tag{2.5}$$

which is defined as the ratio between u'^3 and the turbulent dissipation rate ϵ. Similar to t_L, a turbulent timescale t_T is formulated as

$$t_T = \frac{l_T}{u'}. \tag{2.6}$$

The scales of the smallest eddies, at which the turbulent energy is dissipated, is determined based on the work of Kolmogorov [80], [81]. The size l_η of this so-called Kolmogorov-scales is estimated as

$$l_\eta = \left(\frac{\nu^3}{\epsilon}\right)^{\frac{1}{4}}. \tag{2.7}$$

In addition, the Kolmogorov timescale t_η read

$$t_\eta = \left(\frac{\nu}{\epsilon}\right)^{\frac{1}{2}}. \tag{2.8}$$

Turbulence strongly affects premixed combustion. Different forms of turbulence-chemistry interaction exist due to the fact that turbulent and chemical processes might take place on various length and timescales. For the classification of distinct regimes of premixed combustion, turbulence-chemistry-interaction is categorised by several characteristic non-dimensional numbers [106]. First, the turbulent Reynolds number Re_T is defined analogue to Eq. 2.3 as [106]

$$\mathrm{Re}_T = \frac{u' l_T}{\nu}, \tag{2.9}$$

where u and l are replaced by the turbulent quantities u' and l_T. With increasing values for Re_T, the influence of molecular heat and mass transfer decreases

in comparison to turbulent mixing processes.

The Karlovitz number Ka compares the laminar (chemical) timescales with the timescales of the smallest turbulent structures [106]

$$\mathrm{Ka} = \frac{t_\mathrm{L}}{t_\eta}. \tag{2.10}$$

A second Karlovitz number Ka_δ is given by [106]

$$\mathrm{Ka}_\delta = \frac{t_\delta}{t_\eta} = \left(\frac{l_\delta}{l_\eta}\right)^2 \approx 0.01\mathrm{Ka}, \tag{2.11}$$

which solely considers the thickness of the heat release zone l_δ instead of l_L. For H_2 as well as hydrocarbon mixtures, $l_\delta \approx 0.1 l_\mathrm{L}$ [106].

Based on these characteristic numbers, different regimes of premixed turbulent combustion have been defined by Borghi [14] as illustrated in Fig. 2.1. Description within the scope of this thesis follows the modifications of Peters [106].

The combustion regimes in Fig. 2.1 can be characterised as follows [106]:

- **Laminar flames**: $\mathrm{Re}_\mathrm{T} < 1$ indicates that the flow field comprises no turbulence and therefore no interaction of the flow with the flame front is possible.
- **Wrinkled flamelets**: Due to the fact that u' is smaller than S_L, the vortices cannot effectively interact with the laminar flame front and solely slight wrinkling occurs.
- **Corrugated flamelets**: In this regime, Ka< 1 and $\mathrm{Re}_\mathrm{T} > 1$, but l_η is still larger than the flame structure which remains quasi-steady. Chemical interaction is excluded. As $u' > \mathrm{S}_L$, the flame front is wrinkled by the turbulent vortices.
- **Thin reaction zones**: Ka > 1 denotes that the size of the smallest vortices is below the laminar flame thickness which can therefore interact with

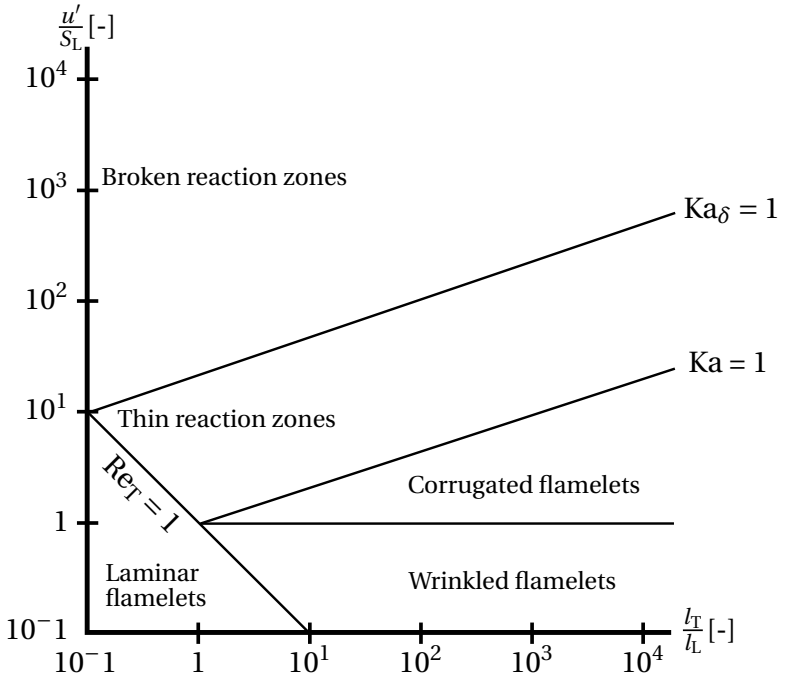

Figure 2.1: Regime diagram of turbulent premixed combustion according to Peters [106].

the preheat zone, resulting in thickening of the flame front. Moreover, mixing is intensified, increasing the turbulent burning velocity S_T. However, the vortices are still larger than the reaction zone and thus this zone remains thin and the flamelets keep a 1-D character.

- **Broken reaction zones**: Kolmogorov eddies are smaller than the width of the reaction zone and are consequently able to perturbate this zone. As a result, chemistry can be influenced by turbulence, leading, i.e. to local extinction effects (quenching). The compact flame structure is replaced by multiple burning pockets.

In the context of flame acceleration and explosion processes, the regimes are passed through in an upwards direction, caused by an increasing turbulence level [18]. After weak ignition, a certain level of both, u' and l_T is required to reach the conditions for DDT [64]. Thus, the critical regime for a DDT is located in the upper right region of Fig. 2.1 [25]. From these considerations it can be concluded that the flamelet assumption is the most appropriate ba-

sis for the deflagration model as turbulence-chemistry interaction is expected in various flamelet regions of the diagram. However, unsteady explosion processes cannot be fully described by this steady-state diagram as crucial phenomena like auto-ignition and intrinsic flame instabilities are not considered. The following section outlines the phenomenology of flame acceleration in more detail.

2.2 Flame Acceleration

Flame acceleration is a key element of explosive combustion as it creates critical conditions for the onset of a detonation. Detonation is initiated by either strong or weak ignition. Typically, accident scenarios in chemical plants comprise weak ignition of the combustible mixture. A schematic of this process is highlighted in Fig. 2.2. Weak ignition is followed by the slow flame regime. Subsequent flame acceleration strongly depends on the initial and boundary conditions. Enhanced levels of temperature, pressure and turbulence are promoting flame acceleration. In the fast flame regime, turbulence and the degree of confinement are the main influencing parameters of flame acceleration. In case sufficiently large flame velocities are reached, DDT will take place, followed by detonation [25].

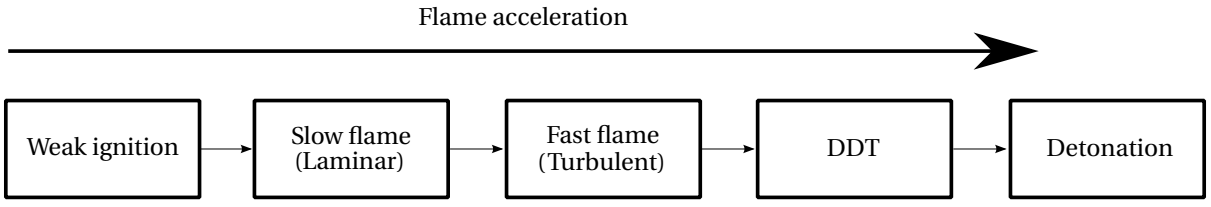

Figure 2.2: Schematic of flame acceleration process after weak ignition.

From a physical point of view, flame acceleration is driven by a positive feedback loop of gas dynamic and fluid dynamic mechanisms, which cannot be considered separately, as illustrated in Fig. 2.3. The early phase of flame acceleration is dominated by the gas dynamic feedback loop, as propagation of emitted pressure waves is faster than the creation of the turbulent flow field.

Therefore, the increase of the burning velocity is dominated by preconditioning of the fresh gas, flame stretch effects and the influence of instabilities, which will be described in more detail in Sec. 2.2.2. With increasing flame and flow velocities, the turbulence level increases accordingly and fluid dynamic effects in terms of turbulent flame wrinkling become dominant.

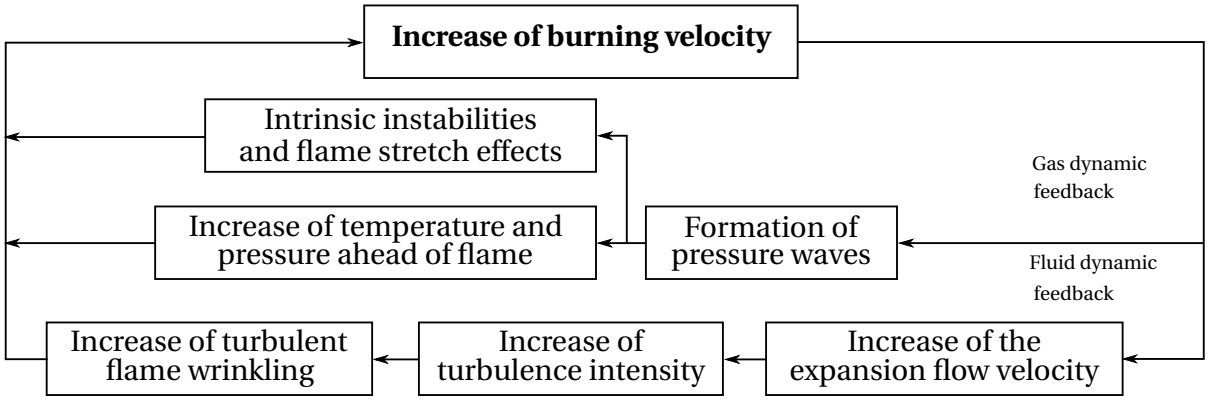

Figure 2.3: Gas dynamic and fluid dynamic feedback loop of flame acceleration process (modified from Brehm [17]).

2.2.1 Phenomenology

A commonly used approach to estimate the acceleration potential of a combustible mixture is the so-called σ criterion from Dorofeev [33]

$$\sigma = \frac{\rho_\mathrm{u}}{\rho_\mathrm{b}} > \sigma_\mathrm{cr}. \tag{2.12}$$

The expansion ratio σ (ratio of unburnt ρ_u to burnt density ρ_b) has to exceed a critical value σ_cr, which is the actual criterion, for the transition from slow to fast deflagration to take place. For H_2/air mixtures at ambient conditions, a value of 3.75 was determined empirically. The σ criterion is a necessary requirement for the development of a fast flame. In smooth geometries, the fast flame regime is reached when the flame front velocity is in the order of the speed of sound of the educts a_e [25].

The process of flame acceleration in smooth pipe-like geometries consists of several characteristic stages, illustrated in Fig. 2.4 [86].

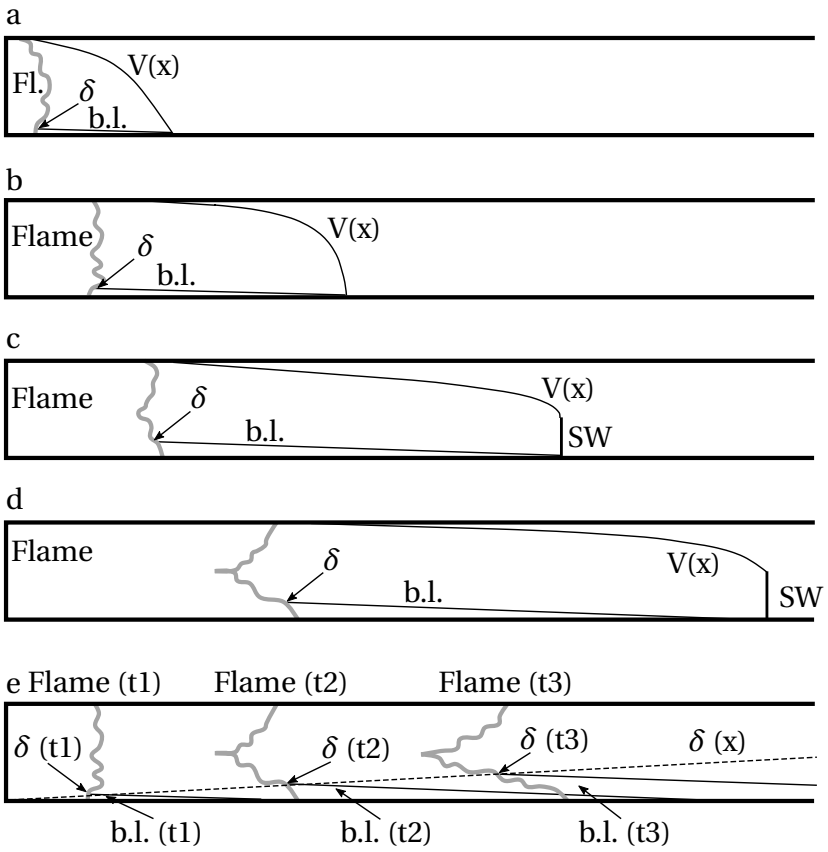

Figure 2.4: Schematic of flame acceleration process in pipes and development of boundary layer and shock ahead of the flame front (adapted from [86]).

Expansion of the hot combustion products downstream the flame acts like a piston, inducing a flow field in front of the flame. Weak pressure waves, emitted by the flame, transport this information into the unburnt mixture at a_e. During the early phase of flame acceleration (Fig. 2.4a), the flow ahead of the flame remains laminar and is likely to have a relatively smooth velocity profile $V(x)$. Moreover, a boundary layer (b.l.) of a thickness δ develops [120]. Formation of this boundary layer is crucial for flame acceleration and DDT in smooth pipe-like geometries [113]. If the pipe is sufficiently long, $V(x)$ steepens with time as shown in Fig. 2.4b and the flow as well as the boundary layer become turbulent. At some point, a shock wave will form due to accumulat-

ing pressure waves, either at the head of the compression wave (Fig. 2.4c) or between the leading pressure wave and the flame front.

In addition, the interaction of the turbulent structures with the pipe wall results in a thickening of δ with time. Turbulent vortices form in the boundary layer, increasing the local burning velocity due to the related turbulent flame wrinkling. As a result, the characteristic "tulip" shape may develop, as reported by Clanet [26], Gonzalez [56] and Salamandra [112].

The accompanying increase in the integral heat release, which results from the growth of the flame surface, leads to the emission of stronger pressure waves. This process further enhances the turbulence level. Therefore, flame acceleration continues as illustrated in Fig. 2.4d until the flame reaches the maximum deflagration speed which corresponds to the speed of sound of the reaction products a_{pr}, being a necessary requirement for DDT. A summary of the whole process is shown in Fig. 2.4e [86].

Flame acceleration in smooth spherical geometries is driven by the same physical mechanisms, outlined previously. However, most of the turbulence is produced by shear layers in the bulk flow, resulting from the propagating flame front and gas dynamics. The impact of boundary layer turbulence is small. Moreover, the growth of flame surface with increasing flame radius is an important aspect as this enhances the integral heat release and therefore intensifies flame acceleration [9], [10], [78].

Higher flame acceleration rates and therefore a shorter run-up distance to DDT can be realised by obstacle-laden geometries. This incresaes turbulent flame wrinkling and the integral heat release rate significantly. However, this setup is not of interest for the current thesis and therefore the interested reader is referred to Ciccarelli [25].

2.2.2 Flame and Flow Instabilities

Apart from turbulent flame wrinkling, various instabilities can increase the flame velocity [25]. These instablilities are either of hydrodynamic nature or flame specific. Flow instabilities are [51], [126]:

- **Rayleigh-Taylor instability**: Hydrodynamic instability which promotes growth of disturbances at interfaces in flows with fluids of different density. This instability occurs if the fluids are accelerated in different directions by gravity or other forces.

- **Kelvin-Helmholtz instability**: Accumulation of small disturbances in the shear layer between two fluids with different flow velocity or flow directions.

- **Richtmyer-Meshkov instability**: This instability appears when a shock wave is running through an interface which separates two fluids of different density. Subsequently, small amplitude perturbations evolve, which initially grow linear and afterwards non-linear in time. Finally, a chaotic regime, mixing the two phases, is reached.

The flame specific Landau-Darrieus (LD) and thermal-diffusive (TD) instabilities are described in more detail as these instabilities are considered in the combustion model (Sec. 3.5). Their nature is intrinsic, meaning that the occurrence is independent of driving forces like turbulence or pressure waves. Depending on mixture composition and initial conditions, the influence of LD and TD instabilities is of particular importance during the early acceleration phase. However, their influence diminishes continuously with increasing turbulence level [25].

The principle of the LD instability is depicted in Fig. 2.5. A curved flame front intrinsically develops due to gas dynamic effects associated to the expansion of the reaction products. The resulting curvature (t_1) causes the streamlines to converge behind convex sections and to diverge behind concave sections. This mechanism accelerates and decelerates the flame locally in the convex and concave parts, respectively. Thus flame wrinkling is enhanced (t_2). This small scale wrinkling increases the flame surface and therefore the integral heat release and flame speed [25].

Fig. 2.6 illustrates a schematic of the TD instability. This type of instability results from an imbalance of the diffusive fluxes of heat and species, which is described by the Lewis number

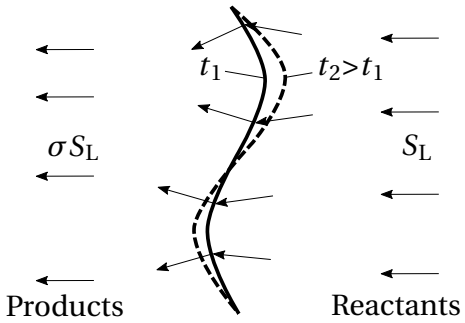

Figure 2.5: Schematic of Landau-Darrieus instability (adapted from [25]).

$$\mathrm{Le} = \frac{a}{D}. \tag{2.13}$$

Le compares the thermal diffusivity a and the diffusion coefficient D of the deficient species, related to the unburnt state of the mixture. Regarding the influence of the TD instability on a curved flame front, two different scenarios have to be considered: Le<1 (Fig. 2.6 left) and Le>1 (Fig. 2.6 right).

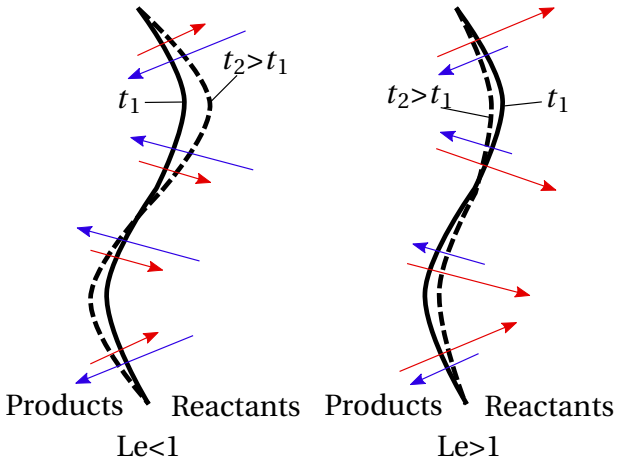

Figure 2.6: Schematic of thermal-diffusive (TD) instability. Flame front coloured black, heat flux coloured red and species flux coloured blue (adapted from [25]).

If Le<1, more educts are diffusing (blue arrows) into convex parts of the flame front while simultaneously there is a decreased heat loss (red arrows). This increases the combustion temperature and hence the burning velocity locally.

The opposite process appears in the concave parts, diminishing the burning velocity. Flame wrinkling is amplified in this scenario. On the contrary, Le>1 has a smoothening and stabilising effect on the flame front. Typically, the TD instability appears immediately after the ignition, while the LD instability requires a critical flame radius and therefore appears downstream the ignition location [25], [51], [126]. Further information on flame instabilities can also be found in [27].

2.3 Deflagration-to-Detonation Transition

Throughout this thesis, DDT is referred to as the onset of a detonation, namely the transition itself, excluding the flame acceleration and direct detonation initiation. Therefore, DDT is a consequence of sufficiently strong flame acceleration. The transition of deflagrative combustion into detonation is equivalent to an abrupt transition from a flame propagation mechanism largely driven by diffusion and turbulence into a shock-induced auto-ignition driven mechanism.

From safety perspective, DDT is very harmful as the occurring pressure loads are even above the Chapman-Jouguet (CJ) pressure of a stable detonation. Thus, this phenomenon is of particular interest for risk assessment. However, the exact process of DDT is not yet fully understood in detail. There exist several approaches and mechanisms to describe this phenomenon.

According to Klein [79], the DDT mechanisms can be categorised into two main types from a macroscopic point of view:

- **Strong solution**: DDT caused by shock focusing or shock reflection.
- **Weak solution**: Onset of detonation in the vicinity of the flame front through mixing processes of unburnt pockets or by interaction of gas dynamics, instabilities and turbulence with the flame front.

The strong solution can be explained from reaction kinetics. A shock wave must be sufficiently strong focused at either a corner of an obstacle or re-

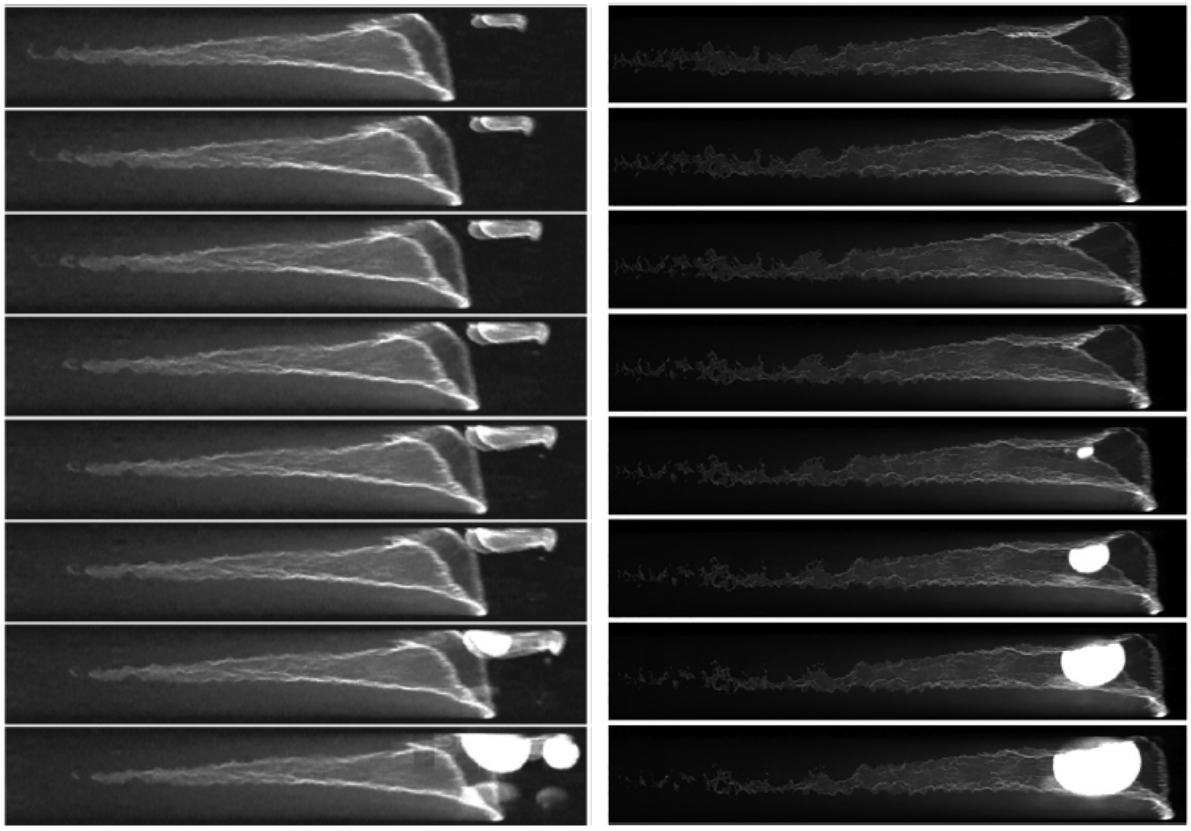

Figure 2.7: Flame front self-luminosity photos of strong (left) and weak (right) DDT mechanism for a H_2 flame in a smooth pipe (reproduced from [83]).

flected from a wall of the surrounding containment to locally exceed the auto-ignition temperature. The DDT is therefore located in front of the flame [130]. This mechanism is shown in Fig. 2.7 on the left for a H_2/air mixture in a smooth pipe [83]. Local explosion ahead of the flame front arises from a hot spot close to the upper wall of the pipe and expands towards the flame front. Consequently, a second explosion is triggered at the leading edge of the flame front. A third explosion close to the first explosion evolves in the onset of a detonation.

A second category implies the so-called weak solution which results directly from the vicinity of the flame front. This category covers the DDT scenarios investigated in this work. Weak explosions, which originate from mixing pro-

cesses induced by turbulence or instabilities [32], appear continuously near the flame front during a fast deflagration. Hence, pockets of unburnt fresh gas are transported into the burnt gas. Explosions arise from the reaction of these pockets, forming local hot spots [54], [102].

Another important representative of this category is DDT induced by shock-boundary layer interaction. This mechanism is of particular relevance for the occurrence of DDT in smooth pipes. As shown in a computational study by Dzieminska [37], the boundary layer ahead of the flame front is preconditioned by a series of pressure waves and weak shocks, which initiates a strong local explosion in the boundary layer. In that context, the preconditioning of the unburnt mixture determines whether DDT and self sustained detonation propagation result from such a hot spot. This mechanism is shown in Fig. 2.7 on the right [83]. Initially, a small explosion arises at the lower leading edge of the flame front. Afterwards, a second explosion takes place close to the upper end, resulting in the onset of detonation. If there are multiple opposing small explosions within the boundary layer, DDT can also appear in the center of the pipe.

Oran [101] carried out numerical simulations of the described DDT mechanisms and discovered that the formation of a local hot spot and subsequent explosion is an important characteristic of all the cases investigated. From this local hot spot, a explosion might occur under appropriate conditions. Hence, the origin of DDT is associated with the formation of these hot spots. Due to the fact that this mechanism is very sensitive to temperature, pressure and fuel content, it is of stochastic nature [101].

On a microscopic level, DDT can be explained by the so-called *Shock Wave Amplification by Coherent Energy Release* (SWACER) mechanism from Lee [90]. This theory claims a mechanism containing spatial reactivity gradients which result from the spatial gradient of the ignition-delay or induction time, being a strong non-linear function of mixture composition, pressure and temperature. Thus, the reaction is initiated in the region with the smallest induction time, the hot spots. Through thermal expansion and creation of shock waves, the neighbouring areas are ignited subsequently, following the reactivity gradient. This self-supporting mechanism can result in DDT under appro-

priate temperature and pressure conditions.

From the perspective of practical safety analysis, an empirical criterion in addition to the σ-criterion (Eq. 2.12) is defined, which determines the likelihood of DDT, the so-called λ-criterion [34]

$$L = 7\lambda. \tag{2.14}$$

λ is the detonation cell width (Fig. 2.10), depending on the mixture composition and the initial thermodynamic state. If flame acceleration is sufficiently strong, provided by the σ-criterion, the λ-criterion has to be additionally fullfilled for the onset of detonation. The characteristic geometrical scale L has to exceed the criterion of 7λ. According to Dorofeev [34], the experimental data base includes H_2/air mixtures in geometries on various scales (long obstructed channels and rooms with small blockage ratio). However, being derived from a limited amount of experiments, including statistical scattering, the range of validity is small. Different criteria are available for periodically obstructed channels or semi-confined geometries [18]. The complex interactions of turbulence, chemistry and gas-dynamics within chemical plants cannot be captured by this criterion. That explains why this criterion can solely be used for rough estimates.

2.4 Detonation

After DDT has taken place, the flame front and shock wave couple, forming a self-sustaining detonation complex. The shock wave is preserved through the heat release of the flame. The detonation complex will be described by 1-D theoretical considerations and by its 3-D nature in the following.

According to the theory by Chapman [21] and Jouguet [76], the detonation complex can be represented by using a 1-D, steady, adiabatic, inviscid and compressible flow in which two discontinuities are included. The internal structure of the detonation complex is neglected. The reference frame is moving with the discontinuities through which the calculated velocities are rel-

ative to this reference frame. The state of the gas is evaluated sufficiently before and after the reaction front. Therefore, thermal and chemical equilibrium can be assumed. Moreover, the specific isobaric heat capacity c_p and the isentropic exponent κ are taken to be constant. Despite these simplifications, stable detonation propagation is described well by this theory.

Due to the fact that detonations propagate at supersonic velocities, viscous effects are neglected and the description follows the integral Euler equations. Conservation of mass, momentum and energy write as [8]

$$\rho_1 u_1 = \rho_2 u_2, \tag{2.15}$$

$$p_1 + \rho_1 u_1^2 = p_2 + \rho_2 u_2^2, \tag{2.16}$$

$$h_1^s + \frac{u_1^2}{2} + q_{12} = h_2^s + \frac{u_2^2}{2}, \tag{2.17}$$

whereby ρ is density, u the flow velocity, p pressure, h the specific enthalpy and q the specific heat. Index 1 denotes the reactants and index 2 the products. h consists of the enthalpy of formation h^f and the sensible enthalpy h^s

$$h = h^f + h^s = h^f + c_p\,(T - T_{\mathrm{ref}})\,. \tag{2.18}$$

Neglecting the change in the kinetic energy, q_{12} is given by the difference of the enthalpies of formation

$$q_{12} = h_2^f - h_1^f. \tag{2.19}$$

As shown by Bartlmä [8], an expression for p can be derived from the ideal gas law, considering the fresh gas quantities. By combining Eq. 2.15 and Eq. 2.16, the equation for the Rayleigh line [147]

$$\frac{p_2}{p_1} = 1 + \kappa \mathrm{Ma}_1^2 \left(1 - \frac{\rho_1}{\rho_2}\right) \tag{2.20}$$

is deduced. A detailed derivation is found in [8]. Via the Mach number $\mathrm{Ma}_1 = \frac{u_1}{\sqrt{\kappa R T_1}}$, the velocity of the inflow is considered.

Furthermore, using Eq. 2.18 and Eq. 2.19 as well as the specific isobaric heat capacity for ideal gases

$$c_p = R\frac{\kappa}{\kappa - 1}, \tag{2.21}$$

the energy equation (Eq. 2.17) can be transformed into the equation for the Hugoniot curve [147]

$$\frac{p_2}{p_1} = \frac{\frac{\kappa+1}{\kappa-1} - \frac{\rho_1}{\rho_2} + \frac{2\kappa}{\kappa-1}\frac{q_{12}}{c_p T_1}}{\frac{\kappa+1}{\kappa-1}\frac{\rho_1}{\rho_2} - 1}, \tag{2.22}$$

which estimates the pressure jump as a function of the density jump and the heat release.

Rayleigh line (blue) and Hugoniot curves (red) are illustrated in the Rankine-Hugoniot diagram in Fig. 2.8. There exists an infinite number of solutions, being located on a Hugoniot curve and a suitable Rayleigh line. However, it can be demonstrated that there is solely one solution for steady detonation propagation, the so-called Chapman-Jouguet (CJ) solution [90]. Starting from the initial state (p_1, ρ_1), the intersection points of Rayleigh line and Hugoniot curve represent possible solutions (regions II and IV) as both equations must be satisfied. The Rayleigh lines have a slope of $-\kappa Ma_1^2$, being always negative. Hence, the grey shaded regions I and III are excluded from possible solutions. In addition, a Hugoniot curve with the particular case of no heat release ($q = 0$) is inserted, but as $q > 0$ in exothermic reactions, only curves of $q > 0$ are of interest for the current work. Regarding the propagation velocity $\mathrm{D}_{0,\mathrm{CJ}}$ of a stable detonation complex, two solutions have been found by Chapman [21] and Jouguet [76]

$$\mathrm{D}_{0,\mathrm{CJ}} = \sqrt{\kappa R T_0 + \frac{\kappa^2 - 1}{2} q_{12}} \pm \sqrt{\frac{\kappa^2 - 1}{2} q_{12}}. \tag{2.23}$$

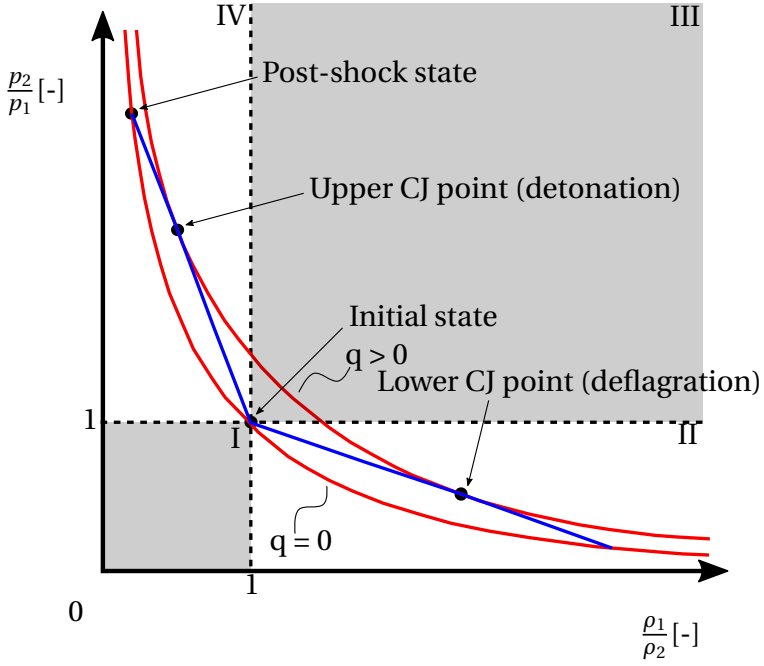

Figure 2.8: Rankine-Hugoniot diagram: Hugoniot curves (red) and Rayleigh line (blue) for $q = 0$ and $q > 0$ (adapted from [89]).

The solution for $D_{0,CJ}$ with the negative sign denotes the maximum subsonic deflagration solution, which is located in region II and comprises a small pressure drop.

On the contrary, the supersonic detonation solution for $D_{0,CJ}$ in region IV is retrieved by the positive sign, being associated with a sharp pressure rise. If the pressure rise caused by the shock is larger than the CJ condition prescribes, two intersection points exist. This phenomenon is called an overdriven detonation in which only the upper intersection point can be reached in reality. This state is unstable and hence expansion waves, emitted from the flame front, can run into the detonation front and relax the pressure until the CJ condition is satisfied.

The CJ theory has been separately investigated and extended by Zeldovich [153], von Neumann [137] and Döring [31] with respect to the internal structure of the detonation complex. They developed the so-called ZND theory. The structure of the detonation complex according to this theory is depicted in Fig. 2.9. An infinitesimal thin leading shock wave is followed by a high pressure

level, the so-called von Neumann spike, and the reaction zone. The von Neumann spike can be calculated from shock relations, incorporating the propagation velocity of the leading shock and inert conditions [2]. Moreover, the reaction zone is divided into two sections: the induction time, representing the phase of ignition delay, and the exothermic heat release, indicated by the thermicity Θ in Fig. 2.9. Thermicity measures the rate at which chemical energy is transformed into thermal energy. This heat release and the accompanying expansion ensure a constant strength of the leading shock, which maintains a self-sustaining detonation propagation at a constant speed. Furthermore, the detonation complex is followed by the so-called Taylor expansion fan which gradually decreases pressure and velocity to meet the boundary condition on the products' side. The pressure level after the Taylor fan (Fig. 2.9) is calculated as [127]

$$p_{\mathrm{Tay}} = \left(\frac{a_{\mathrm{Tay}}}{a_{\mathrm{CJ}}}\right)^{\frac{2\kappa}{\kappa-1}} \approx 0.375\, p_{\mathrm{CJ}}, \tag{2.24}$$

where the speed of sound a_{Tay} is defined as

$$a_{\mathrm{Tay}} = \frac{\kappa+1}{2} a_{\mathrm{CJ}} - \frac{\kappa-1}{2} \mathrm{D}_{\mathrm{CJ}}. \tag{2.25}$$

However, Erpenbeck [41] proved mathematically that a 1-D detonation complex is not stable and comprises therefore always a 3-D structure. Every disturbance of the detonation front causes a fluctuation in the heat release which needs to be compensated by transversal waves. Experimental studies have also proven this 3-D structure, consisting of Mach stems and transversal waves [1], [38], which will be explained in the following.

Fig. 2.10 shows a shadowgraphy of a detonation complex (leading shock and reaction zone) from a C_2H_4 mixture in the upper right part [5]. Generally, a cellular structure with the characteristic detonation cell size λ develops in a 3-D detonation. λ is given by the dimension perpendicular to the propagation direction. The cells resemble a rhombus-like pattern. Moreover, the regularity of the individual cells is heavily affected by the fuel, the mixture composition

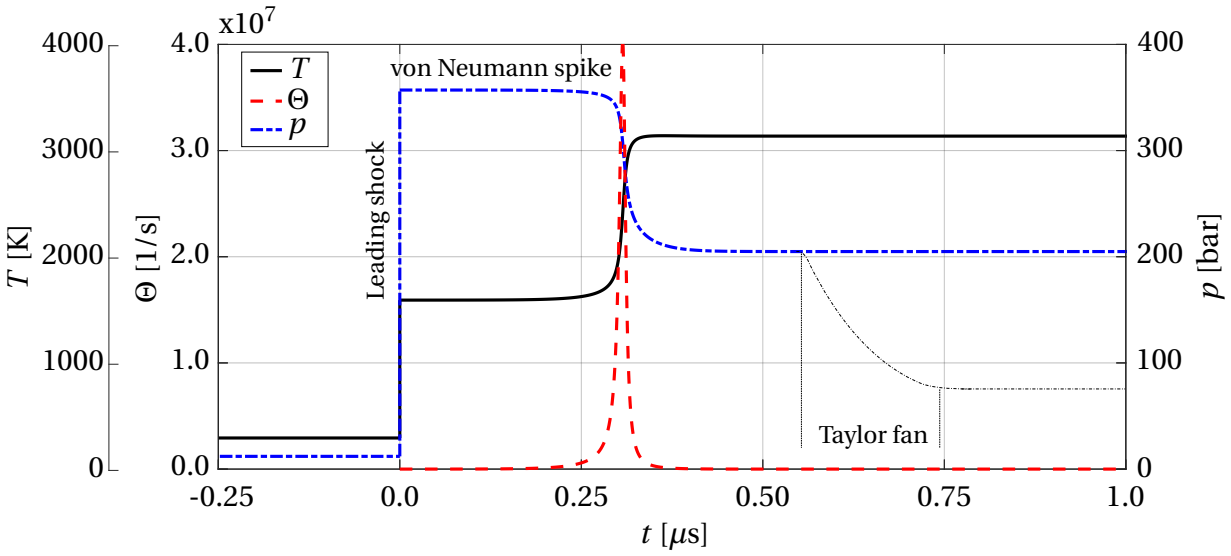

Figure 2.9: Structure of a one dimensional detonation complex according to the ZND theory. Temporal profiles of thermicity Θ (heat release), temperature T and pressure p for a stoichiometric hydrogen/air mixture at 12 bar and 293 K, retrieved from Cantera [57] calculations with the shock and detonation toolbox [44] and the O'Conaire mechanism [99]. Taylor fan schematically added by grey dashed line.

and the activation energy [48]. The soot-foil technique is used to visualise the cellular structure in experiments and to measure λ. Highly-resolved detonation simulations are also capable of visualising λ by evaluating the maximum pressure of a propagating detonation at each position. However, λ cannot directly be calculated from first principles.

In the upper left part of Fig. 2.10, the whole detonation complex, travelling from left to right, is shown. The strong compression of the induction zone by the leading shock wave, exceeding auto-ignition conditions, is indicated by the dark region. Afterwards, the density decreases through the reaction.

A schematic of the cellular detonation structure is highlighted in the lower part of Fig. 2.10. The interaction of the longitudinal main shock LS with a transverse shock TS results in the creation of Mach stems M. Due to the fact that fresh gas temperature and pressure are higher behind the Mach stems,

than behind the longitudinal shock, the flame front F couples at a smaller distance behind the Mach stems due to the smaller ignition delay times t_{ign}. The characteristic pattern of the detonation cell is eventually formed by the trajectory of the triple point T which represents the collision point of Mach stem, longitudinal and transverse shocks.

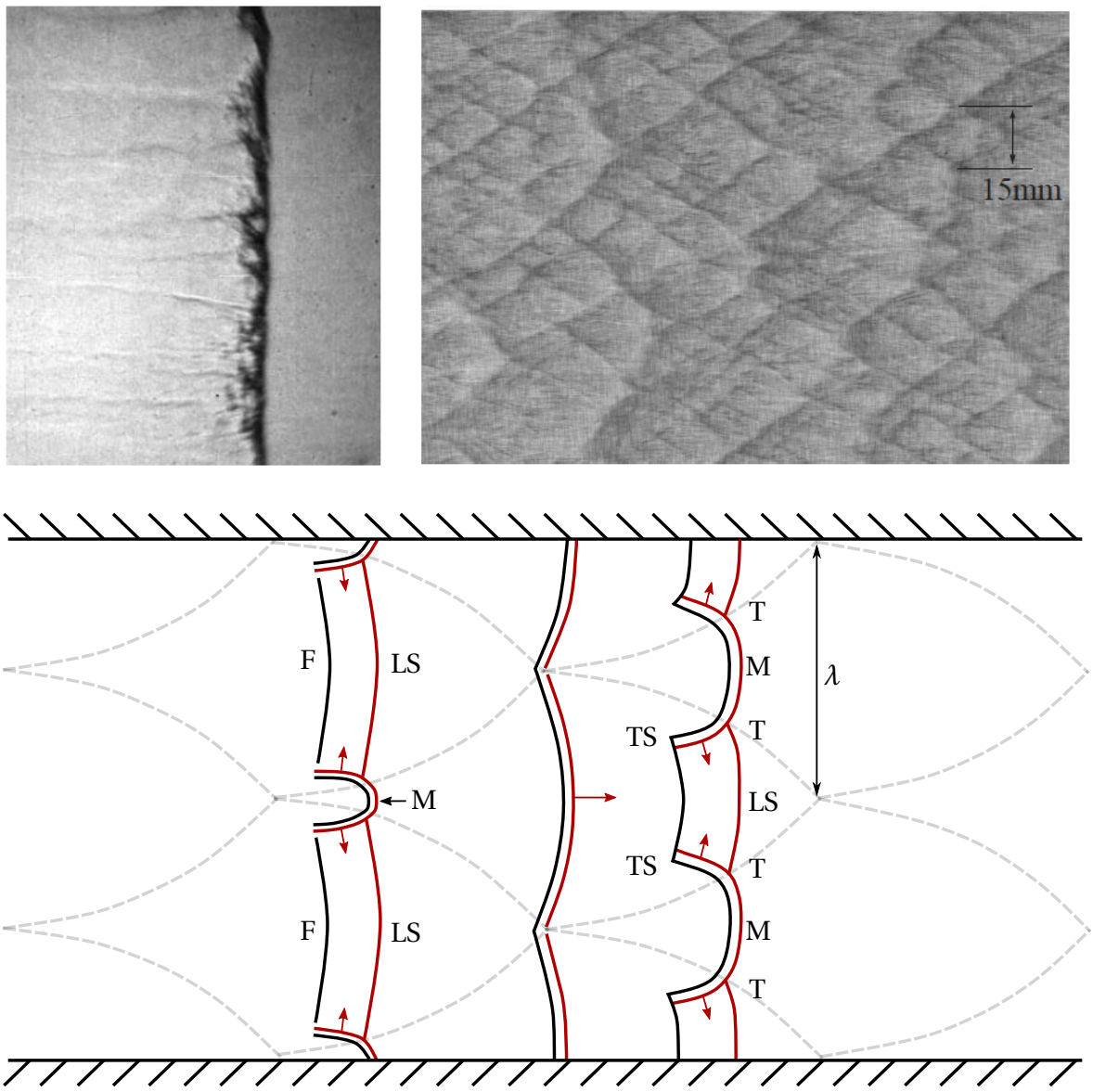

Figure 2.10: Shadowgraphy of detonation complex travelling from left to right (top left) and cellular detonation structure (top right) of a stoichiometric ethylene/air mixture reproduced from [5]. Schematic of cellular detonation structure (bottom) (adapted from [38]), flame coloured black and shocks coloured red).

3 Numerical Explosion Modelling

The development of CFD solvers for the simulation of flame acceleration and DDT on industry-scale is mainly driven by nuclear safety research and chemical and process engineering. Typically, these solvers aim at analysing worst case scenarios in order to identify critical configurations for the onset of detonation and the main influencing parameters. Therefore, the modelling focuses on predicting flame propagation at a macroscopic level. Multiple difficulties are associated with the development, which will be elucidated before introducing available CFD DDT solvers.

3.1 Simulation Challenges for Smooth Geometries in Chemical Plants

Regarding flame acceleration, DDT and detonation propagation in smooth geometries (Sec. 2.2, Sec. 2.4), various requirements with respect to the involved physical phenomena, numerical robustness and efficiency of the solver arise for the current work [30]. The most challenging aspects, in particular, are reviewed in the following:

- **Efficiency**: In order to avoid unpractical computation times, the CFD solver should have the ability of simulating industrial-scale domains under the aspect of restricted available computational resources.
- **Flow discontinuities**: Due to the highly unsteady nature of explosion processes, the state of the flow variables is characterised by abrupt spatio-temporal changes. These discontinuities must be preserved by a physically meaningful modelling approach for their correct evolution in the time and space domains.

- **Large variety of flow regimes**: The simulation is initialised at quiescent conditions. Then, the flow velocity increases due to flame propagation and acceleration. In the time span between simulation start and a certain velocity threshold, the flow characteristics are governed by incompressibility. After exceeding this threshold, it is essential to consider compressibility effects in the simulation.
- **Large disparity of time and length scales**: The timescales range from the smallest chemical timescales for fuel oxidation and heat release to the scales of the large turbulent structures. The same accounts for the length scales where the spectrum ranges from the width of the reaction zone and the smallest turbulent scales - the Kolmogorov eddies - up to the dimensions of the containment. Appropriate modelling is indispensable as it is not feasible to resolve all the scales involved.
- **Combustion model**: Chemistry is heavily influenced by turbulence, as illustrated in the Borghi diagram (Fig. 2.1). In the context of DDT simulations, multiple regimes and the temporal evolution of the turbulence-chemistry interaction must be considered (Sec. 2.1). Hence, a modelling approach - covering the whole process of flame acceleration after weak ignition (Fig. 2.2) - is of particular importance, as there exists yet no computational method to fully resolve the turbulence-chemistry interaction for large-scale geometries with available computational resources.
- **Reactive mixtures**: Stoichiometric fuel/oxidizer mixtures at elevated pressures are typically used in the chemical industry for optimising the reactions and reducing the plant dimensions. This represents a challenge in detonation modelling due to the strongly decreasing ignition delay times t_{ign} in comparison to atmospheric conditions.

3.2 State of the Art Industry-Scale DDT Solver

Many approaches and solvers for the simulation of reactive flows exist. However, their validity is limited to the particular combustion regime for which the underlying physical effects are considered in the respective approach [106]

[126]. For DDT simulations, two combustion processes, deflagration and detonation, must be considered. These processes are associated with fundamentally different combustion mechanisms (Sec. 2.2 and Sec. 2.4). Deflagrations are characterised by subsonic propagation and are driven by the diffusive and turbulent mixing of heat and species. In contrast, detonations comprise supersonic combustion which is dominated by gas dynamic effects and autoignition [25]. This complicates the implementation of models which accurately capture the interaction between chemistry, gas dynamics and fluid dynamics in a single solver while maintaining a stable convergence behaviour. Hence, appropriate combustion modelling for a DDT solver represents a compromise between physical accuracy, numerical robustness, sensitivity with respect to initial and boundary conditions and the required computational resources [30].

Due to the large dimensions of the plant components considered in this thesis, it is difficult to realise a grid-independent solution, resolving all chemical and turbulent scales. This explains why this review focuses on solvers capable of dealing with industry-scale issues. Without the sake of completeness, relevant approaches for the scope of this work, in particular, shall be brought to the reader's attention. Solely CFD DDT solvers which are able to simulate large-scale geometries with moderate computational resources and simulation runtimes are considered. Moreover, applicability within the context of flame acceleration and DDT in smooth geometries will be discussed for the individual solvers.

- **GASFLOW-MPI**: For the simulation of flame acceleration, DDT and detonation propagation, developed by the Karlsruher Institute of Technology (KIT) [150], [151]. The compressible Navier-Stokes equations are solved within a pressure-based solver architecture. Cartesian grids in combination with Adaptive Mesh Refinement (AMR) are used. Moreover, two turbulence models are available, the k - ϵ and the k-ω SST model. The combustion model covers lean H_2 mixtures and is based on a reaction progress variable approach, which distinguishes between a turbulence controlled combustion rate and a chemically controlled combustion rate for deflagration and detonation, respectively. The onset of detonation is

triggered by an induction parameter. Although there are several similarities to the solver developed in this work (Sec. 3.4), application to smooth geometries is questionable. This is due to the fact that obstacle-laden geometries are typically of interest for nuclear safety. As a consequence, combustion modelling concentrates on the fast flame regime and the dominating turbulent flame wrinkling. Therefore, other physical phenomena are neglected in the combustion modelling of this solver. However, the initial stage of slow flames - being dominated by instabilities, flame stretch and the expansion of the flame front - is a crucial aspect of flame acceleration in smooth geometries. Hence, deficits are about to be expected.

- **FLACS**: Developed from the safety and risk management company Gexcon [53] for the simulation of process engineering accident scenarios [3], [96], [138]. This code uses a cartesian-based distributed porosity concept for grid generation. This allows the simulation of a variety of complex geometrical features on a sub-grid level in terms of obstacle-induced turbulence production. Turbulence modelling is realised by the k-ϵ model, which is capable of predicting turbulence production in shear layers in the bulk flow, but boundary layer turbulence is captured more accurately by the k-ω model. Consequently, deficits for the early stage of flame acceleration - being driven by boundary layer turbulence - are to be expected. The compressible Navier-Stokes equations are solved by a pressure-based algorithm. In order to account for DDT, the 7λ criterion (Eq. 2.14) is applied in combination with a model related to the spatial pressure gradient. Therefore, DDT cannot be described as the combination of gas dynamics and auto-ignition effects as mainly fuel content and geometrical dimensions influence the applied DDT criterion. This shortcoming limits the applicability of the FLACS solver to a small number of accident scenarios. Since the solver incorporates solely a deflagration model, running until the DDT criterion is satisfied, detonation propagation cannot be computed. The deflagration model is called a β flame model, developed by Arntzen [3], and resembles an artificial flame thickening approach [126]. The combustion model and the sub-grid models are highly calibrated, restricting the applicability. In addition, validation

is again carried out with respect to obstacle-laden geometries and venting cases [96], [138]. Hence, application to smooth geometries is difficult to realise.

- **EUROPLEXUS**: Developed by the Atomic Energy and Alternative Energies Commission (CEA) [135]. As this code is based on the 3-D reactive Euler equations, viscous effects cannot be captured. However, these effects are crucial for the early phase of flame acceleration in smooth pipe-like geometries, regarding the boundary layer creation and associated turbulence production. Combustion is considered by a reaction progress variable approach. This approach includes two models for the source term closure, which should be chosen depending on geometrical and turbulence conditions. In conclusion, this architecture allows the simulation of every relevant combustion regime during flame acceleration (Sec. 2.1), including DDT and detonation propagation. The validation comprised obstacle-laden components of nuclear power plants as well as venting cases, which again complicates the transfer to smooth geometries.

- **REACFLOW**: The Institue for Energy of the Joint Research Centre Ispra uses this solver in the context of nuclear safety research [6], [146]. This code solves the compressible Navier-Stokes equations on unstructured meshes. Turbulence closure is realised by means of the k-ϵ model, being not well-suited for boundary layer driven flows. Convective fluxes are computed by an approximate Riemann solver. Two combustion models are exploited: one for finite rate chemistry and the Eddy-Dissipation model (EDM) [126] which defines the chemical reaction rate as a function of k and ϵ. However, the range of validity of the EDM model is limited and this model is not able to cover all relevant combustion regimes during flame acceleration. Due to the fact that the solver's capability focuses on the fast flame regime and detonation propagation, obstacle-laden geometries were used for validation, limiting the applicability to smooth geometries.

- **TONUS**: This review is closed by the TONUS solver [84], developed in the context of nuclear safety by the CEA and the Radiation Protection

and Nuclear Safety Institute. The compressible Navier-Stokes equations form the basis and two turbulence models are integrated: a mixing length model and the k-ϵ model, having a limited applicability to smooth pipe-like geometries. Again, combustion is represented by a reaction progress variable approach for reasons of efficiency. Three different source term closures are included for H_2 combustion: one for quasi-laminar conditions, the Eddy-Breakup model (EBU) to consider turbulence-chemistry interaction and a model for detonation propagation. However, the simple EBU model is not able to accurately cover turbulence-chemistry interaction during all stages of flame acceleration. Validation was carried out in obstacle-laden geometries and predominantly for the fast flame regime, restricting the transfer to smooth geometries.

In conclusion, each solver is designed for its specific field of application and some involve a high level of calibration, limiting or even excluding the transfer to other fields. The solvers predominantly focus on the fast flame regime and detonation propagation. Therefore, obstacle-laden geometries and venting cases are of interest for solver development and validation. Nevertheless, flame acceleration in smooth gemoetries implies a distinct phase of slow to medium fast deflagrations, for which deficits are about to be expected by these solvers. However, this phase is crucial for the whole process as it determines whether critical conditions for the onset of a detonation are reached. In addition, most of the applied turbulence modelling approaches are not well-suited for boundary layer driven flows. The k-ϵ model, i.e. is capable of predicting turbulence production in shear layers in the bulk flow but boundary layer turbulence is captured more accurately by the k-ω model. Hence, a different modelling approach has to be developed, which is capable of simulating various smooth geometries and dealing with the associated challenges, outlined in Sec. 3.1.

3.3 Governing Equations for DDT Simulations

The DDT solver in this work is based on the works of Ettner [43] and Hasslberger [62] and uses the open-source CFD package OpenFOAM [141], written in C++. The modular structure allows for building the DDT solver on existing code packages and models. Spatial discretization in OpenFOAM is realised using the Finite Volume Method (FVM). Furthermore, topologically complex unstructured grids are supported and computational cost can be handled by massive parallelisation. OpenFOAM version 2.1.x is used.

The governing equations are presented in strong form for a fixed cartesian coordinate system. Moreover, Einstein's summation convention [40] is applied due to its compactness as long as not specified differently. First, the conservation equations for mass, momentum and energy are outlined, followed by the turbulent averaging procedure. Afterwards, the k-ω SST turbulence model is described.

3.3.1 Differential Conservation Equations

Due to the highly unsteady nature of flame acceleration, DDT and detonation after weak ignition (Fig. 2.2), the problem features a mixed parabolic-hyperbolic character. The flow dynamics can be captured by the compressible Navier-Stokes equations together with mass und energy conservation equations. [1] In combination with the ideal gas law, these equations can be solved for the state variables: density ρ, pressure p, temperature T and flow velocity u. All subsonic, transsonic and supersonic flow phenomena are inherently included. Additionally, gas dynamic effects like the propagation of pressure waves and shocks are incorporated. A detailed derivation of these equations can be found in [46], [129], [142].

Conservation of mass is formulated in terms of the continuity equation as [126]

[1] In the following, the term Navier-Stokes equations always includes the conservation of mass and energy for reasons of clarity and brevity.

$$\frac{\partial \rho}{\partial t} + \frac{\partial}{\partial x_j}\left(\rho u_j\right) = 0, \tag{3.1}$$

with t and x_j as the time and spatial coordinates, respectively.

Conservation of momentum in each cartesian direction i is ensured by solving [126]

$$\frac{\partial}{\partial t}\left(\rho u_i\right) + \frac{\partial}{\partial x_j}\left(\rho u_i u_j\right) = \frac{\partial \tau_{ij}}{\partial x_j} - \frac{\partial p}{\partial x_i} + \rho g_i, \tag{3.2}$$

where the pressure term acts as a driving force for the velocity field, which can either accelerate or decelarate the flow. g_i denotes body forces which are due to gravitational acceleration. The viscous stress tensor τ_{ij} can be expressed based on Stoke's hypothesis [142] as

$$\tau_{ij} = \mu\left(\frac{\partial u_i}{\partial x_j} + \frac{\partial u_j}{\partial x_i} - \frac{2}{3}\delta_{ij}\frac{\partial u_m}{\partial x_m}\right). \tag{3.3}$$

$$\delta_{ij} = \begin{cases} 1, & i = j \\ 0, & i \neq j \end{cases} \tag{3.4}$$

Here, δ_{ij} represents the Kronecker-delta [46] and μ the dynamic viscosity, serving as a proportionality constant between the velocity gradients and the resulting shear stress. In this thesis, μ is retrieved from the Sutherland equation [107]

$$\mu = A_\mathrm{s}\frac{T^{3/2}}{T + T_\mathrm{s}}, \tag{3.5}$$

where A_s is the material-specific Sutherland constant and T_s is the Sutherland temperature.

The conservation of energy can be expressed in different forms. Due to the significant contribution of the kinetic energy in transsonic and supersonic flows,

it is necessary to formulate energy conservation in terms of the mixture's specific total internal energy e_t. This consists of the static internal energy e and the kinetic energy [126]

$$e_\mathrm{t} = e + \frac{u_i u_i}{2}. \tag{3.6}$$

The balance equation for e_t is given by [126]

$$\frac{\partial}{\partial t}\left(\rho e_\mathrm{t}\right) + \frac{\partial}{\partial x_j}\left(\left(\rho e_\mathrm{t} + p\right) u_j\right) = -\frac{\partial q_j}{\partial x_j} + \frac{\partial}{\partial x_j}\left(\tau_{ij} u_i\right). \tag{3.7}$$

For reasons of clarity, potential energy, volumetric sources and sinks, radiation as well as Dufour and Soret effect [65] have already been neglected as the influence of these contributions to the DDT dynamic is of minor importance. When expressed in terms of e_t, no chemical source term appears in the energy equation [126]. The static internal energy remains constant while chemical reaction shifts the portions of chemically bounded energy and sensible energy. Changes in the sensible energy constitute in temperature variations. The temperature of the mixture is therefore determined iteratively from Eq. 3.7.

The diffusive flux q_j contains the heat flux via heat conduction and the enthalpy flux via species diffusion, which is neglected here. Using Fourier's law [147], q_j is expressed as

$$q_j = -\lambda \frac{\partial T}{\partial x_j} = -\rho a \frac{\partial h}{\partial x_j}. \tag{3.8}$$

a is the thermal diffusivity defined as

$$a = \frac{\lambda}{\rho c_p}, \tag{3.9}$$

with the thermal conductivity λ and the specific isobaric heat capacity

$$c_p = \frac{\partial h}{\partial T}. \tag{3.10}$$

The enthalpy h can be derived from the thermodynamic identity

$$h = e + \frac{p}{\rho}. \tag{3.11}$$

This yields the final formulation for the conservation of e_t as

$$\frac{\partial}{\partial t}\left(\rho e_t\right) + \frac{\partial}{\partial x_j}\left(\left(\rho e_t + p\right) u_j\right) = \frac{\partial}{\partial x_j}\left(\rho a \frac{\partial h}{\partial x_j} + \tau_{ij} u_i\right). \tag{3.12}$$

The set of equations is closed by the ideal gas law [126]

$$p = \rho R T, \tag{3.13}$$

where R denotes the specific gas constant of the mixture.

3.3.2 Turbulent Averaging

The investigated components of chemical plants are characterised by large dimensions and the process of flame acceleration and DDT is at later stages associated with high Reynolds numbers. This eliminates the application of *Direct Numerical Simulations* (DNS) [7], [91] as the required computational resources are still not available. *Large-Eddy Simulations* (LES) [49], [47], which resolve only the large scales and model the influence of the small eddies, are not feasible for the current work, either. The filter width would have to be chosen large and therefore the benefits compared to the averaging procedure presented below would be small. Hence, only the *Unsteady Reynolds-Averaged Navier-Stokes* (URANS) equations represent an appropriate basis. At least the statistical effects of turbulence can be considered [106], [109], [126], which is sufficient for predicting the global flame propagation behaviour correctly. Capturing the statistical effects of turbulence in the URANS equations allows

to meet the DDT simulation challenges mentioned in Sec. 3.1. Moreover, a suitable combustion model can be integrated (Sec. 3.5).

To arrive at the URANS equations, each turbulent quantity ϕ is decomposed into a mean part $\overline{\phi}$ and a fluctuating part ϕ', which captures the effect of turbulent motions

$$\phi = \overline{\phi} + \phi'. \tag{3.14}$$

The intention of this procedure is to reduce the computation to the averaged quantities $\overline{\phi}$. In the *Reynolds-Averaged Navier-Stokes* (RANS) methodology, $\overline{\phi}$ is defined in a specified time interval $\triangle t$ [126]

$$\bar{\phi} = \frac{1}{\Delta t} \int_{t=t_0}^{t_0+\Delta t} \phi dt \tag{3.15}$$

Hence, there exists a clear separation between the steady main flow and the turbulent fluctuations in the RANS context. However, two unsteady phenomena are considered in the URANS equations [109]. In addition to the turbulent fluctuations ϕ', temporal variations of the averaged flow quantity $\overline{\phi}$ are considered as well. The URANS methodology allows for this separate description of the transient phenomena as long as the time step $\triangle t$, over which the average is taken, is greater than the characteristic time measures of the turbulent fluctuations. Noll [98] could however prove, that the URANS equations are also well suited for flow problems, implying high frequency changes of the flow field, as long as these changes are of deterministic and not chaotic nature [67]. Therefore, the URANS equations can capture the essential aspects of the highly unsteady nature of flame acceleration and DDT.

In case of these highly unsteady processes, $\overline{\phi}$ can be interpreted as an ensemble-average instead of a temporal average within the URANS context [109]

$$\overline{\phi} = \frac{1}{N} \sum_{n=1}^{N} \phi_n, \tag{3.16}$$

which constitutes an average with respect to N instances ϕ_n of the considered quantity ϕ.

The definition of the Reynolds-averaging implies that the averaged fluctuating quantity vanishes

$$\overline{\phi'} = 0. \tag{3.17}$$

However, the product of turbulent fluctuations does not vanish

$$\overline{\phi'\psi'} \neq 0. \tag{3.18}$$

Applying this averaging procedure on the conservation equations in Sec. 3.3.1 introduces several unknown terms in the form of Eq. 3.18, the so-called Reynolds Stresses [52]. The amount of these unkonwn Reynolds Stress terms in compressible flows can be reduced considerably by applying a density-weighted avarging procedure of turbulent quantities (Favre-averaging) [45]

$$\tilde{\phi} = \frac{\overline{\rho\phi}}{\overline{\rho}}. \tag{3.19}$$

In analogy to Eq. 3.16

$$\phi = \widetilde{\phi} + \phi'', \tag{3.20}$$

where the fluctuating part is denoted as ϕ''.

By inserting Eq. 3.20 into the conservation Eqs. 3.1, 3.2 and 3.7, the URANS equations are obtained [2] [126]

$$\frac{\partial}{\partial t}\bar{\rho} + \frac{\partial}{\partial x_j}\left(\bar{\rho}\,\widetilde{u}_j\right) = 0, \tag{3.21}$$

[2] For the sake of simplicity, the denotation URANS equations comprises the Favre-Averaged continuity and energy equations as well.

$$\frac{\partial}{\partial t}\left(\bar{\rho}\widetilde{u}_i\right)+\frac{\partial}{\partial x_j}\left(\bar{\rho}\widetilde{u}_i\widetilde{u}_j\right)+\frac{\partial}{\partial x_j}\left(\bar{\rho}\widetilde{u_i''u_j''}\right)=\frac{\partial\bar{\tau}_{ij}}{\partial x_j}-\frac{\partial\bar{p}}{\partial x_i}+\bar{\rho}\widetilde{g}_i, \tag{3.22}$$

$$\frac{\partial}{\partial t}\left(\bar{\rho}\widetilde{e}_\mathrm{t}\right)+\frac{\partial}{\partial x_j}\left(\left(\bar{\rho}\widetilde{e}_\mathrm{t}+\bar{p}\right)\widetilde{u}_j\right)+\frac{\partial}{\partial x_j}\left(\bar{\rho}\widetilde{h''u_j''}\right)=\frac{\partial}{\partial x_j}\left(\bar{\rho}a\frac{\partial\widetilde{h}}{\partial x_j}+\bar{\tau}_{ij}\widetilde{u}_i\right). \tag{3.23}$$

In this thesis, the unknown Reynolds Stress terms in Eqs. 3.22 and 3.23 are expressed as [126]

$$\bar{\rho}\widetilde{u_i''u_j''}=-\mu_\mathrm{T}\left(\frac{\partial\widetilde{u}_i}{\partial x_j}+\frac{\partial\widetilde{u}_j}{\partial x_i}-\frac{2}{3}\delta_{ij}\frac{\partial\widetilde{u}_m}{\partial x_m}\right)+\frac{2}{3}\delta_{ij}\bar{\rho}k, \tag{3.24}$$

$$\bar{\rho}\widetilde{h_t''u_j''}=-\bar{\rho}a_\mathrm{T}\frac{\partial\widetilde{h}_t}{\partial x_j}. \tag{3.25}$$

In Eq. 3.24 k denotes the turbulent kinetic energy given by

$$k=\frac{\widetilde{u_i''u_i''}}{2}. \tag{3.26}$$

The modelling of the impact of turbulence on the ensemble-averaged solution quantities is based on the eddy viscosity hypothesis of Boussinesq [126]. In this context, a theoretical eddy viscosity μ_T, a turbulent thermal diffusivity a_T and a turbulent diffusion coefficient D_T are introduced in order to consider the influence of unresolved turbulent fluctuations on the resolved mean flow field. These quantities are combined with the temporally constant laminar quantities in order to form effective quantities

$$\begin{aligned}\mu_\mathrm{eff}&=\mu+\mu_\mathrm{T},\\ a_\mathrm{eff}&=a+a_\mathrm{T}=a+\tfrac{1}{\mathrm{Pr_T}}\tfrac{\mu_\mathrm{T}}{\bar{\rho}},\\ D_\mathrm{eff}&=D+D_\mathrm{T}=D+\tfrac{1}{\mathrm{Sc_T}}\tfrac{\mu_\mathrm{T}}{\bar{\rho}}.\end{aligned} \tag{3.27}$$

a_{eff} and D_{eff} are derived from the turbulent Prandtl number $\text{Pr}_\text{T} = 1$ and the turbulent Schmidt number $\text{Sc}_\text{T} = 1$, respectively.

Inserting Eqs. 3.24 and 3.25 into Eqs. 3.21-3.23 with Eqs. 3.26 and 3.27 finally yields the governing equations solved in this thesis:

$$\frac{\partial \bar{\rho}}{\partial t} + \frac{\partial}{\partial x_j}\left(\bar{\rho}\,\widetilde{u}_j\right) = 0, \tag{3.28}$$

$$\begin{gathered}\frac{\partial}{\partial t}\left(\bar{\rho}\,\widetilde{u}_i\right) + \frac{\partial}{\partial x_j}\left(\bar{\rho}\,\widetilde{u}_i\,\widetilde{u}_j + \frac{2}{3}\delta_{ij}\bar{\rho}k\right) = \frac{\partial}{\partial x_j}\mu_{\text{eff}}\left(\frac{\partial \widetilde{u}_i}{\partial x_j} + \frac{\partial \widetilde{u}_j}{\partial x_i} - \frac{2}{3}\delta_{ij}\frac{\partial \widetilde{u}_m}{\partial x_m}\right) - \\ \frac{\partial \bar{p}}{\partial x_i} + \bar{\rho}\,\widetilde{g}_i,\end{gathered} \tag{3.29}$$

$$\frac{\partial}{\partial t}\left(\bar{\rho}\widetilde{e}_\text{t}\right) + \frac{\partial}{\partial x_j}\left(\left(\bar{\rho}\widetilde{e}_\text{t} + \bar{p}\right)\widetilde{u}_j\right) = \frac{\partial}{\partial x_j}\left(\bar{\rho}\,a_{\text{eff}}\frac{\partial \widetilde{h}}{\partial x_j} + \bar{\tau}_{ij}\widetilde{u}_i\right). \tag{3.30}$$

The final task comes down to find an expression for μ_T, which is presented in the next section.

3.3.3 Turbulence Model

Turbulence modelling is crucial, not only for the closure of the Favre-Averaged governing equations (Eqs. 3.28-3.30). There also exists a strong dependency of the burning velocity in the combustion model on turbulence-chemistry interaction (Sec. 3.5). In that context, adequate prediction of the turbulent quantities is indispensable.

In this thesis, the k-ω SST turbulence model of Menter [93] is applied. This model characterises turbulence in terms of the turbulent kinetic energy k, the angular eddy frequency ω and the specific turbulent dissipation rate ϵ. The benefit of the k-ω SST model is to combine the advantages of the k-ϵ [74] and the k-ω [144] model by using blending functions F_i. Hence, the k-ω model is used in the near wall region since boundary layer turbulence can only be poorly predicted by the k-ϵ formulation. Apart from that, the robustness of the k-ϵ model in the bulk flow ensures a stable convergence behaviour. Thus,

this model is able to capture turbulence production of accelerating flames in smooth geometries: boundary layer turbulence during the early acceleration phase in smooth pipe-like geometries as well as turbulence production in the bulk flow at later stages and in spherical geometries.

The combination of these two models has proven to be a reasonable compromise between accuracy, numerical robustness and reliabilty for turbulence prediction in various applications of industrial interest [75]. A detailed description of the implementation in OpenFOAM can be found in [94].

In the k-ω SST, the eddy viscosity is calculated from [94]

$$\mu_{\mathrm{T}} = \frac{a_1 \bar{\rho} k}{\max\left(a_1 \omega; F_2 S\right)}, \tag{3.31}$$

for which an invariant measure of the strain rate is calculated as

$$S = \sqrt{2} \left| \frac{1}{2} \left(\frac{\partial \widetilde{u}_i}{\partial x_j} + \frac{\partial \widetilde{u}_j}{\partial x_i} \right) \right|. \tag{3.32}$$

The transport equation for k (Eq. 3.26) is defined as

$$\frac{\partial}{\partial t}(\bar{\rho} k) + \frac{\partial}{\partial x_j}\left(\bar{\rho} k \widetilde{u}_j\right) - \frac{\partial}{\partial x_j}\left(\Gamma_{\mathrm{k,eff}} \frac{\partial k}{\partial x_j}\right) = P_k^* - \bar{\rho} \underbrace{\beta^* \omega k}_{\varepsilon}, \tag{3.33}$$

which also includes the relationship between k, ϵ and ω in the sink term on the right side. In addition, the transport equation for ω is given by

$$\begin{gathered} \frac{\partial}{\partial t}(\bar{\rho}\omega) + \frac{\partial}{\partial x_j}\left(\bar{\rho}\omega \widetilde{u}_j\right) - \frac{\partial}{\partial x_j}\left(\Gamma_{\omega,\mathrm{eff}} \frac{\partial \omega}{\partial x_j}\right) = \\ \frac{\bar{\rho}\gamma(F_1)}{\mu_T} P_k - \bar{\rho}\beta\left(F_1\right)\omega^2 + 2\left(1 - F_1\right)\bar{\rho}\alpha_{\omega 2} \frac{1}{\omega} \frac{\partial k}{\partial x_j} \frac{\partial \omega}{\partial x_j}. \end{gathered} \tag{3.34}$$

The production of turbulent kinetic energy

$$P_k^* = \min\left(P_k; c_1 \bar{\rho}\varepsilon\right) = \min\left(\bar{\rho}\widetilde{u_i'' u_j''} \frac{\partial \widetilde{u}_i}{\partial x_j}; c_1 \bar{\rho}\varepsilon\right) \tag{3.35}$$

is closed via Eq. 3.24 and limited by the dissipation of k. This deficit is required for reasons of numerical stability. Otherwise, the turbulent kinetic energy at stagnation points would artificially increase. For further details about this turbulence model, the interested reader is referred to Menter [94].

3.4 Solver Architecture and Discretisation

The governing equations derived in Sec. 3.3 as well as the equations of the combustion model (Sec. 3.5) represent a coupled system of non-linear partial differential equations. In order to numerically solve these equations, the Finite Volume Method (FVM), which is formulated in a flux conservative manner [46], is applied. This methodology divides the simulation domain into finite volumes. In the center of each volume, an average value of every solution variable is stored. Linearising the equations leads to a system of equations in the form

$$A\vec{\phi} = \vec{b}, \tag{3.36}$$

including the solution variables $\vec{\phi} = \left(\rho, \rho\vec{u}, \rho e_t, \rho\psi_k\right)^{\mathrm{T}}$. ψ_k represents all transported scalar variables and $\vec{b}$ contains the boundary conditions. The equations are solved in a segregated manner to ensure a stable convergence behaviour for the highly unsteady nature of explosion processes. Inverting the full matrix A in Eq. 3.36 to solve for $\vec{\phi}$ is not feasible as it is computationally costly and often associated with stability problems [71].

There exist two approaches for solving the coupled system of equations: a pressure-based solution algorithm, which is favorable for incompressible flow problems and a density-based formulation, developed for the simulation of transonic and supersonic flows [46]. Since turbulence production in smooth geometries is lower compared to obstacle-laden geometries [62], there is initially a decisive phase of slow to medium fast flames which eventually determines whether critical flame acceleration and the conditions for a DDT will be reached. Thus, it is of particular importance to accurately predict the evolu-

tion of the flow and turbulence field as well as the resulting flame acceleration during this early phase. Hence, a hybrid solver architecture is presented subsequently, which performs a switchover from a pressure- to a density-based solver, exploiting a developed transition criterion. In the following, it is explained which problems can be circumvented in this way.

As shown in Fig. 2.4, the initial stage is characterised by the expansion of the flame front and the associated emission of pressure waves, inducing the flow acceleration and the formation of a boundary layer in front of the flame (Sec. 2.2). However, the density-based solver is not able to capture the initial pressure built-up in front of the flame due to the fact that pressure is retrieved from the density field via the ideal gas law. Since the density changes by the flow velocity are negligibly small during this incompressible phase, the corresponding pressure elevation is small, too, as illustrated in Fig. 3.2 for Case H13 (Tab. 4.1) [115]. For comparison, the pressure field resulting from the pressure-based solver is shown in Fig. 3.1. The position of the flame front is highlighted by an iso surface of the reaction progress variable ($c = 0.4 - c = 0.6$), coloured grey. In order to compare the two solution methods, the pressure field at the same flame positions is considered in Figs. 3.1 and 3.2. Regarding the pressure-based solution, the pressure built-up in front of the flame between 2.5 ms and 4 ms, which is associated with the expanding flame and the emission of pressure waves, can be predicted. An expansion wave is travelling into the reaction products, which decreases the pressure slightly from 3 ms on.

In contrast to the pressure-based solver algorithm, the density-based solver architecture cannot predict the pressure built-up. At 4 ms, there is a pressure wave propagating along the pipe from left to right, while an expansion wave decreases the pressure level from 5 ms on. This is in accordance with the pressure-based solution. With respect to the temporal evolution of the spatial flame position, the pressure increase and the associated formation of a flow field and turbulence is delayed for the density-based solver. This is caused by the smaller incremental pressure changes per time step, which mutually delays the creation of the boundary layer and turbulence production as shown in Fig. 3.3. Note, scaling of the contour plots is different. The smaller incre-

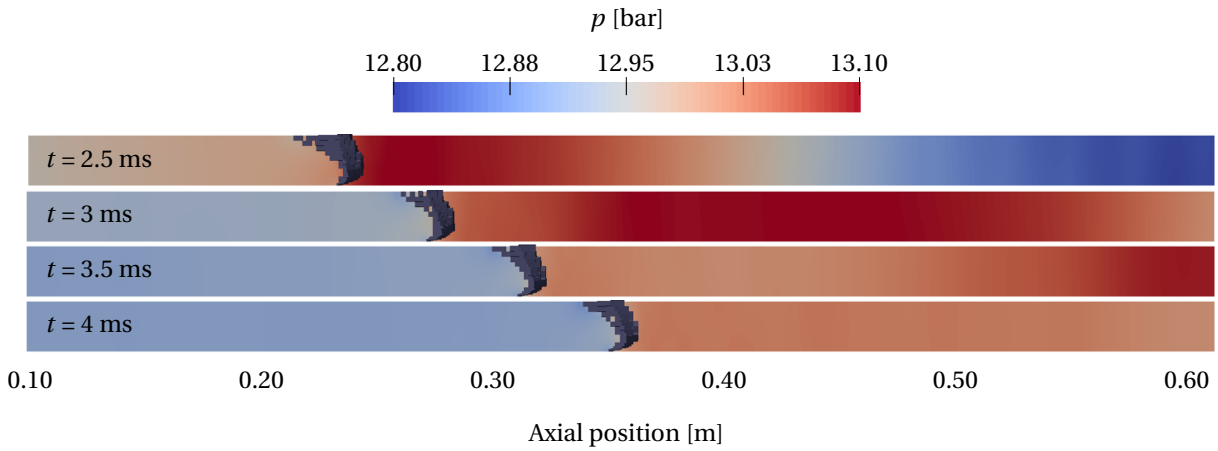

Figure 3.1: Evolution of pressure field for Case H13 [115] for the pressure-based solver on a vertical plane along the pipe axis. The flame front is illustrated by the reaction progress variable field with a threshold between 0.4 and 0.6, coloured grey. Only half of the pipe height is shown. Pipe middle axis is located at the top of the pictures of the individual plots in time.

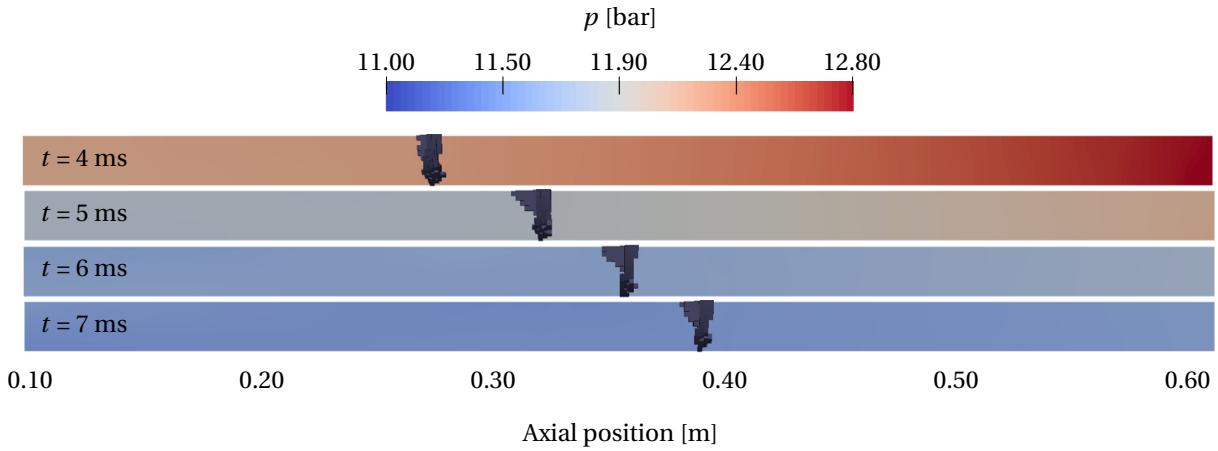

Figure 3.2: Evolution of pressure field for Case H13 [115] for the density-based solver on a vertical plane along the pipe axis. The flame front is illustrated by the reaction progress variable field with a threshold between 0.4 and 0.6, coloured grey. Only half of the pipe height is shown. Pipe middle axis is located at the top of the pictures of the individual plots in time.

mental pressure changes for the density-based solver lead to a lower increase of the flow velocity through the coupling of pressure and velocity via the momentum equation (Eq. 3.29). Consequently, the velocity gradients are smaller which decreases turbulence production (cf. Eq. 3.35) in comparison to the pressure-based solution. The resulting turbulent kinetic energy k field at 4 ms (a: pressure-based) and at 7 ms (b: density-based) additionally emphasise the deficits of the density-based solver during the incompressible phase.

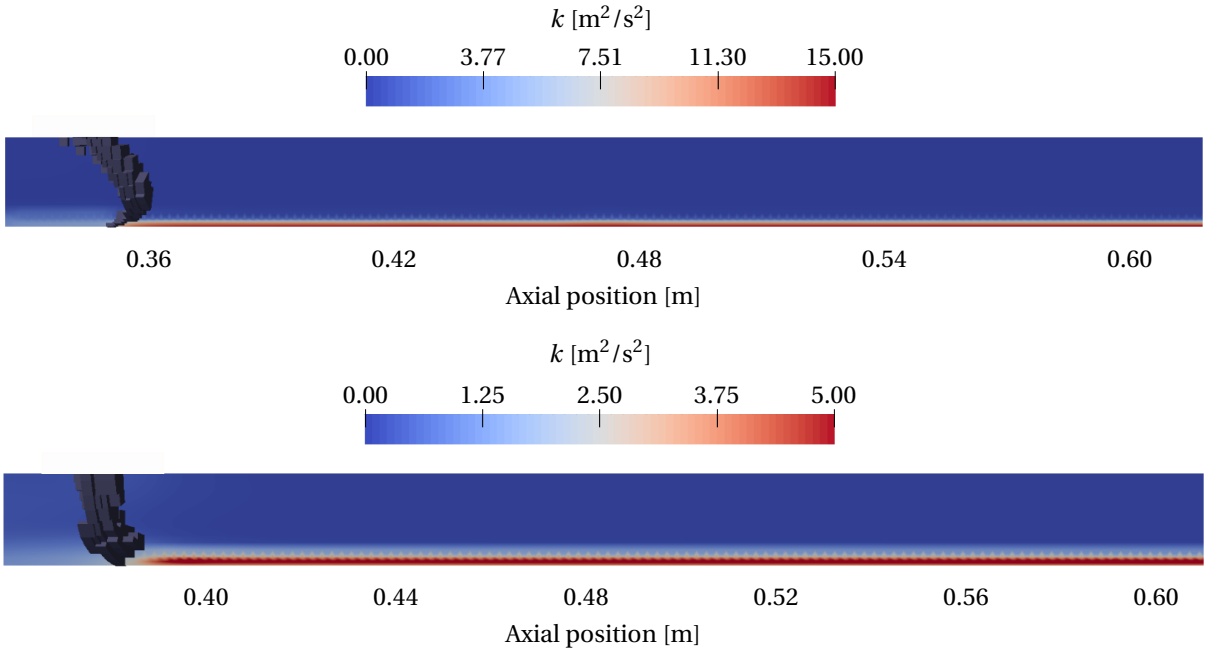

Figure 3.3: Evolution of turbulent kinetic energy field for Case H13 [115] for the pressure-based solver (top) and the density-based solver (bottom) on a vertical plane along the pipe axis. The flame front is illustrated by the reaction progress variable field with a threshold between 0.4 and 0.6, coloured grey. Only half of the pipe height is shown. Pipe middle axis is located at the top.

The turbulence level in the pressure-based solution is three times higher than the density-based solution. Typically for smooth pipe-like geometries, prodution of turbulence initially focuses on the boundary layer [25], [120]. The difference between these two methodologies results in a significant turbulent flame wrinkling and an associated stronger flame accelaration in the case of the pressure-based solution. The same effects can be observed for the density-

based solution, but with a time shift of ≈ 3 ms which grows during the acceleration.

In order to represent both, the early incompressible phase of flame propagation as well as the compressible regime of fast flames and detonation propagation, a hybrid pressure-/density-based methodology is used in this thesis. This approach provides an efficient solver architecture for the investigated phenomena. The principles of the two solution algorithms and the developed transition criterion will be presented in the following sections.

3.4.1 Pressure-Based Solution Method

Knowledge of the pressure field is necessary in order to compute the velocity field via the momentum equation (Eq. 3.29). However, the pressure field is not directly accessible as no explict pressure transport equation is solved. In consequence, the pressure field can only be determined from the velocity field, which is called pressure-velocity coupling [136]. By considering the continuity equation (Eq. 3.28), a pressure correction equation can be obtained from the momentum equation (Eq. 3.29) to solve for the pressure [46]

$$\frac{\partial}{\partial x_i}\left(\frac{\partial \bar{p}}{\partial x_i}\right) = -\frac{\partial}{\partial x_i}\left[\frac{\partial}{\partial x_j}\left(\bar{\rho}\,\widetilde{u}_i\,\widetilde{u}_j - \bar{\tau}_{ij,\,\mathrm{eff}}\right)\right] + \frac{\partial\left(\bar{\rho}\,\widetilde{g}_i\right)}{\partial x_i} + \frac{\partial^2 \bar{\rho}}{\partial t^2}, \tag{3.37}$$

while the continuity equation (Eq. 3.28) can be omitted. The density field is finally retrieved from the ideal gas law. A detailed derivation of Eq. 3.37 is given in App. A.1. In order to solve the non-linear coupling between pressure and momentum in Eq. 3.37, the PIMPLE (*Pressure-Implicit Method for Pressure-Linked Equations*) algorithm [100] is used in this work. This method combines the steady-state SIMPLE (*Semi-Implicit Method for Pressure-Linked Equations*) algorithm [103] with the unsteady PISO (*Pressure Implicit with Splitting of Operators*) methodology [68]. This ensures better stability of the solver compared to the PISO algorithm, being of particular importance for the highly unsteady process of flame acceleration.

In combination with an implicit method, pressure-based solvers offer the ad-

vantage that large time steps can be realised. Within this thesis, temporal discretisation in the pressure-based methodology is carried out using a first order implicit Euler scheme. Adaptive time stepping, in order to adapt the time step size to the highly unsteady flow field, is applied using the Courant-Friedrichs-Lewy (CFL) criterion (Eq. 3.38). Furthermore, a basic second order convection scheme using face-gradients and Gauss' theorem is deployed [100].

With respect to the specific DDT simulation challenges introduced in Sec. 3.1, the pressure-based solution algorithm is in agreement with the following requirements:

- Efficiency
- Large variety of flow regimes
- Large disparity of time and length scales

However, the predictive capabilities of the pressure-based solver are insufficient in the transonic and supersonic flow and flame regime. Specifically, the second order derivate terms in the pressure correction equation (Eq. 3.37) are of diffusive type and provoke the non-physical dissipation of strong pressure gradients as they occur in shock waves. This implies to formulate a transition criterion to change the solver type from the pressure- to the density-based algorithm once a predefined threshold is exceeded. This allows the correct modelling of the whole flame acceleration process including the slow and fast flame propagation phases. Nevertheless, the diffusive nature ensures numerical stability over a wide range for the pressure-based solver. For the sake of comprehensibility, the density-based solver is discussed before the transition criterion is elaborated in detail.

3.4.2 Density-Based Solution Method

The density-based solver architecture accounts for the fast flame regime, DDT and detonation propagation. Within this approach, the continuity equation (Eq. 3.28) is solved in a separated step from the momentum equation (Eq.

3.29) to directly compute the density field. Pressure is accordingly calculated by the ideal gas law, which implies the aforementioned deficits (Sec. 3.4) at low Ma numbers. In contrast to the pressure correction equation (Eq. 3.37), strong pressure gradients can be resolved physically correct by the density-based solver architecture without the occurrence of artificial smearing in the gradient region. This is possible due to the absence of a diffusive term in the continuity equation (Eq. 3.28). Hence, the density-based solver architecture is advantageous regarding the resolution of gas dynamic effects which are crucial for the simulation of DDT as auto-ignition effects and shock-flame interaction have to be considered.

A hybrid explicit-implicit Euler scheme is used for temporal discretisation. By treating the convective fluxes explicitly, this method provides good shock capturing capabilities. Apart from that, diffusive fluxes are accounted for by an implicit scheme. Regarding the uncertainties related to the coarse grids and turbulence as well as the combustion modelling, a first order scheme is considered an appropriate choice, keeping the computational costs moderate. To achieve a stable solution procedure and to minimise the influence of numerical diffusion on the discontinuities, the propagation speed of the waves (characteristics [88]) is taken into account. The maximum wave velocity resulting from the conservation equations and the cell width define the time step size which ensures that every cell is influenced by its neighbouring cells only. However, this requires satisfying the CFL criterion

$$\mathrm{CFL} = \max_{\Omega}\left(\frac{(|u_i| + a)\,\triangle t}{\triangle x}\right) < \mathrm{CFL}_{\max}. \tag{3.38}$$

Here, u denotes the flow velocity, a the speed of sound of an ideal gas ($a = \sqrt{\kappa RT}$), $\triangle t$ the time step size and $\triangle x$ the characteristic grid width. This criterion determines how far information is allowed to propagate within one time step. For the scope of this thesis, a maximum value of $\mathrm{CFL}_{\max} = 0.3$ is chosen for the pressure-based solver and a maximum value of $\mathrm{CFL}_{\max} = 0.2$ is used for the density-based solver. These values represent a compromise between accuracy, numerical robustness and efficiency. A stable numerical solution procedure is guaranteed while the time step size can be set large enough to

efficiently use available computational resources. Further decreasing the time step size does not significantly change the results while the solver tends to diverge at larger values.

Approximate Riemann Solver: HLLC Scheme

For calculating the convective fluxes, face-based values of an arbitrary quantity ϕ_f have to be derived from the cell-centered values ϕ. Typically, various interpolation schemes, differing in complexity and accuracy, are available for the calculation of ϕ_f in commercial CFD codes. However, a different approach is used in this thesis. An approximate Riemann solver, employing the Harten-Lax-van Leer Contact (HLLC) scheme [131], is incorporated into the density-based formulation, as this scheme allows an efficient reconstruction of pressure waves and shocks. The main aspects of the methodology are briefly explained. For detailed information, the interested reader is referred to Toro [131] and Ettner [43].

Initially, a linear reconstruction of ϕ_f from both sides of each face is carried out, delivering two values, ϕ_L and ϕ_R. As these two values are not identical, a discontinuity occurs at the cell face, representing a Riemann problem [88]. An iterative procedure based on the 1-D Euler equations would allow for the exact solution of this problem, but is computationally expensive. Hence, the approximate scheme is applied to be in compliance with the aspect of simulation efficiency.

The HLLC approximate Riemann solver resembles a shock tube problem. Three characteristic waves (contact discontinuity, shock and expansion fan) are assumed to originate from the face of each cell pair. For reasons of efficiency, two assumptions are required. The wave velocity is retrieved from the initial state inside each cell and the inner structure of the expansion fan is not resolved. Accordingly, the face-based value ϕ_f and finally the face flux $\phi_f F_f$ are estimated from ϕ_L and ϕ_R which assures a second-order accurate spatial discretisation.

Validation of the shock capturing capabilities is executed by means of a shock

tube problem, illustrated in Fig. 3.4. The initial state in the shock tube is summarised in Tab. 3.1.

Table 3.1: Initial state of shock tube.

	x < 0	x > 0
p	10 bar	1 bar
T	800 K	300 K
u	0 m/s	0 m/s

Simulation results (red line with dots) are compared with the analytical solution (grey line) at 0.1 ms. Excellent agreement can be observed. The propagation velocity of the shock wave as well as the state behind the shock can be predicted accurately, analysed by the temperature, density and pressure.

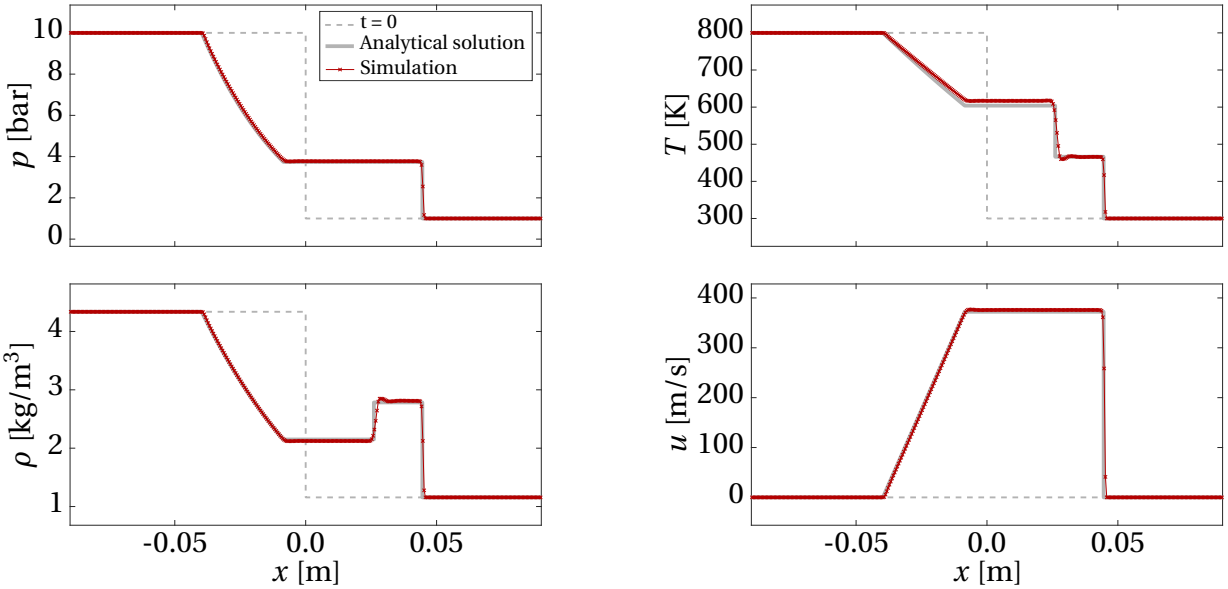

Figure 3.4: Results for shock tube problem with the density-based solver and the HLLC scheme and a cell size of 2.0 mm. Analytical solution coloured grey and simulation results coloured red.

In conclusion, the density-based solver in combination with the HLLC scheme provides a suitable methodology to capture the relevant gas dynamic effects in the later stages of flame acceleration and the subsequent DDT and detonation propagation. With respect to the specific DDT simulation challenges

introduced in Sec. 3.1, the density-based solution algorithm is in agreement with all flow-related requirements:

- Efficiency
- Flow discontinuities
- Large variety of flow regimes
- Large disparity of time and length scales

3.4.3 Transition Criteria

The definition of a universally applicable and robust transition criterion between the two solution methods is not straightforward due to the large number of geometries and process conditions involved in chemical plants. Moreover, solely a limited number of experiments is available (cf. Chap. 4). Hence, this problem is similar to the definition of the σ- (Eq. 2.12) and λ-criterion (Eq. 2.14), for which various formulations exist, depending on fuel and geometry. Within the scope of this work, it is therefore also necessary to make a distinction with regard to the geometry and type of flame propagation for the determination of the transition criterion.

Two criteria, depending on the geometry and associated type of flame propagation (smooth pipes: quasi 1-D, spheres: 3-D), are employed for the transition between the solver architectures as illustrated in Fig. 3.5 and Fig. 3.6. The transition criteria determine the point in time at which pressure- and density-based solver compute equivalent solutions of the flow and flame quantities. For that purpose, two dimensionless numbers are defined which are associated to the main driving mechanisms of flame acceleration in their respective field of application. This allows both solution algorithms to be used efficiently in their intended field of application.

In smooth pipes (Fig. 3.5), the flame propagation is quasi 1-D. The flame accelerates continuously from the initial incompressible slow flame regime up

to the compressible fast flame regime. Turbulent flame wrinkling dominates the overall flame acceleration process (Sec. 2.2).

Therefore, a flame-tip Mach number $\mathrm{Ma}_{\mathrm{flame}}$ is exploited to account for the accelerating flame and flow field as well as the pressure built-up

$$\mathrm{Ma}_{\mathrm{flame}} = \frac{u_{\text{flame-tip}}}{a_{\mathrm{e}}}. \tag{3.39}$$

$\mathrm{Ma}_{\mathrm{flame}}$ compares the flame-tip velocity $u_{\text{flame-tip}}$ with the speed of sound of the educts a_{e} in front of the flame. The c field ($c > 0.01$ and $c < 0.5$) is taken in order to specify the domain for calculating an averaged a_{e}. Only the region directly ahead of the flame is considered as this will subsequently interact with the flame front. If a threshold of $\mathrm{Ma}_{\mathrm{flame}} = 1$ is exceeded, the flame is considered a fast flame in smooth geometries (Sec. 2.2). In that context, gas dynamics and an accurate spatial and temporal evolution of pressure waves and shocks become crucial and therefore transition to the density-based solution method is realised.

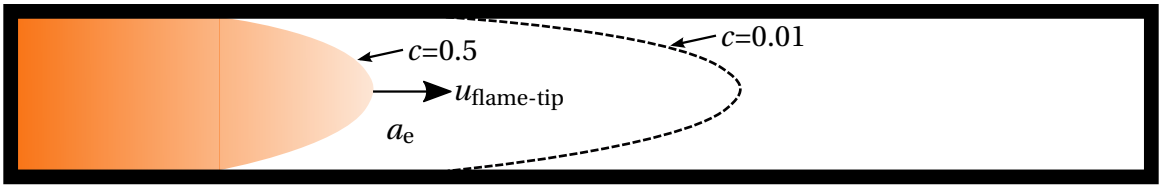

Figure 3.5: Schematic for the calculation of flame-tip Mach number $\mathrm{Ma}_{\mathrm{flame}}$ for transition criterion between pressure- and density-based solver in pipe-like geometries.

In smooth spherical geometries, multi-dimensional flame propagation takes place and expansion of the reaction products as well as the growth of the flame surface with increasing flame radius are important aspects of flame acceleration besides the turbulent flame wrinkling (Sec. 2.2). With regard to the 20 l sphere cases considered in this work (cf. Sec. 4.2), flame acceleration and DDT differ from the smooth pipe cases. Due to the small running length of the flame (radius = 170 mm), there is no prolonged phase of continuous acceleration from the slow to the fast flame regime. The influence of gas dynamic

effects is even more important, caused by the constant reflection and accumulation of pressure waves. The related preconditioning mainly determines the formation of local hot spots. Hence, a different approach for the transition criterion needs to be chosen to account for the strong impact of gas dynamics. The associated transition criterion (Fig. 3.6) is therefore based on an averaged expansion ratio over the flame front $\sigma = \rho_u/\rho_b$, which allows for considering the preconditioning by means of ρ_u as well as the impact of the expansion on flame acceleration in spherical geometries. The switchover point accordingly highlights the point at which a certain level of preconditioning is reached and from which the accurate spatial and temporal evolution of gas dynamic effects becomes crucial in order to predict DDT. The averaged densities ρ_u and ρ_b are computed within the turbulent flame brush over the flame front located at $c = 0.5$. ρ_u is calculated in front of ($c > 0.01$ and $c < 0.5$) and ρ_b behind the flame front ($c > 0.5$ and $c < 0.99$).

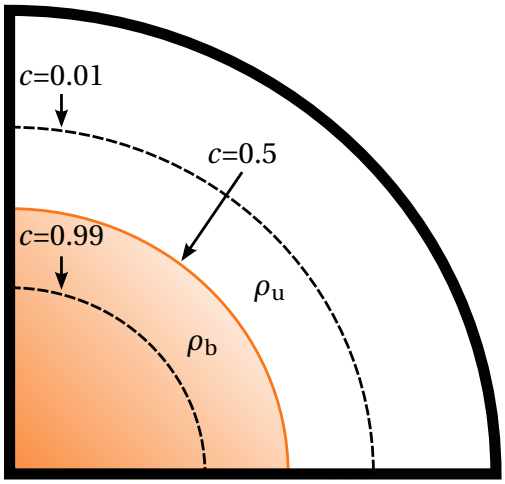

Figure 3.6: Schematic for the calculation of transition expansion ratio σ_{trans} for transition criterion between pressure- and density-based solver in spherical geometries.

The threshold for the transition σ_{trans}, which defines the switchover point in time, is defined empirically to match the experimental pressure data in the 20 l sphere cases (Sec. 4.2). σ_{trans} can be expressed by the expansion ratio of the initial state of the fuel/oxidizer mixture σ_{fuel} and a fuel content dependent factor α_σ

$$\sigma_{\text{trans}} = \sigma_{\text{fuel}} - \alpha_\sigma. \tag{3.40}$$

The correlations for σ_{fuel} are derived from 0-D Cantera [57] calculations with the O'Conaire [99] (H_2) and the Lu [92] (C_2H_4) reaction mechanisms

$$\sigma_{\text{fuel}} = \begin{cases} -36.0389 X_{\text{fuel}}^2 + 33.2454 X_{\text{fuel}} + 0.4266 & \text{for } H_2 \\ -234.9699 X_{\text{fuel}}^2 + 94.7682 X_{\text{fuel}} + 3.0976 & \text{for } C_2H_4. \end{cases} \tag{3.41}$$

Being defined empirically, the correlations for α_σ read

$$\alpha_\sigma = \begin{cases} 10.5138 X_{\text{fuel}} + 3.3011 & \text{for } H_2 \\ 31.6406 X_{\text{fuel}} + 5.7560 & \text{for } C_2H_4. \end{cases} \tag{3.42}$$

The question now arises which criterion should be taken for the simulation of intermediate geometries like cylindrical vessels, being frequently used in chemical plants, too. The selection of the transition criterion is based on geometrical considerations, referring to the aforementioned separation between smooth pipes and spheres. In that context, the decisive parameter is the length to diameter ratio (L/D) of flame propagation with respect to the ignition location. Therefore, differentiation between central ignition or at a wall is significant. This allows for distinguishing between the two types of flame acceleration and the related transition criterion:

- **Smooth pipes:** Beginning of compressible regime. Switchover point determines the point in time at which the solution of the incompressible pressure-based solver is equal to the solution of the compressible

density-based solver after a phase of continuous deflagrative flame acceleration.

- **Sphere:** Switchover point highlights the point in time at which a certain level of preconditioning is reached. An accurate spatio-temporal reproduction of the complex gas dynamics and the prediction of DDT requires the transition to the explicit density-based solver.

As there exists currently no experimental data for flame acceleration and DDT of $H_2/O_2/N_2$ and $C_2H_4/O_2/N_2$ mixtures in relevant cylindrical geometries, solely a recommendation based on experience and dummy computations can be given. If L/D < 5, indicating 3-D flame propagation, the σ criterion should be chosen. Otherwise, if L/D > 5, Ma_{flame} should be taken. This recommendation does not ensure a continuous transition in the application of the other criterion. The determination of a continuous transition function from one criterion to the other as well as a more precise differentiation is an interesting future task and can be realised by evaluating planned experiments.

3.4.4 Adaptive Mesh Refinement

In order to decrease the grid dependencies of the solution variables in underresolved CFD simulations while keeping the computational costs small, an Adaptive Mesh Refinement (AMR) approach is integrated into the solver. Hence, the AMR aims for reducing the discretisation errors resulting from insufficient resolution of physical phenomena [71]. Defining refined mesh regions manually is not feasible for explosion simulations due to the highly unsteady nature and local discontinuities. Using the AMR, high spatial resolution can be realised in regions where relevant phenomena are present. At the same time, the coarse base mesh is kept in the remaining parts of the domain. In order to control the activation of the AMR in regions with relevant physics, a suitable criterion (Eq. 3.43) is defined in this work.

The algorithm for the AMR in OpenFOAM is based on isotropic cell splitting. This means that every cell is split into eight children cells in 3-D simulations [100]. Multiple refinement level can be used. In addition, several buffer

layers can be applied. These layers extend the AMR region to ensure a smooth transition to the base mesh. Due to the unstructured grid handling in OpenFOAM, cell connectivity has to be reestablished after each refinement step. Moreover, the data fields have to be mapped onto the new mesh topology and face fluxes have to be recalculated. However, the errors associated with this mapping process are small. Unrefinement of previously refined regions is feasible and beneficial for the efficiency of the solver. This allows for fully burnt regions to be set back to the coarse base mesh.

A indicator-driven criterion based on velocity gradients is exploited for the activation of the AMR algorithm

$$\mathrm{AMR} = \frac{\left|\frac{\partial |u_i|}{\partial x_j}\right|}{\max_\Omega \left|\frac{\partial |u_i|}{\partial x_j}\right|} > 0.1, \tag{3.43}$$

which compares the local velocity gradient in each cell with the maximum velocity gradient in the boundary area of the domain. The velocity gradient as a criterion to activate the AMR algorithm is beneficial as turbulence production is assumed to be high in these regions. More precisely, the production term of k is a function of this quantity (Eq. 3.35). Owing to the unbounded nature of gradient fields, a normalisation is required.

Refining the flame front itself or shock waves induced artificial asymmetrical flame propagation. This phenomenon could be explained by the underresolved grids where the activation threshold was solely exceeded locally in individual cells. To avoid this unwanted behaviour and ensure a robust criterion on the coarse grids, no further indicator is added.

Recall that turbulence production in the boundary layer is crucial to accurately reproduce the flame acceleration in smooth pipes, especially in the early stage. This explains why the AMR is only applied in the boundary region of the smooth pipes. The AMR is triggered by the ratio between the local velocity gradient ($\left|\frac{\partial |u_i|}{\partial x_j}\right|$) and the maximum velocity gradient in the boundary layer of the domain ($\max_\Omega \left|\frac{\partial |u_i|}{\partial x_j}\right|$). If this ratio exceeds the threshold 0.1, the

cell is divided. The threshold of 0.1 was found to be a reasonable compromise in terms of robustness, accuracy and efficiency. In addition, the AMR is limited to the boundary layer of the fresh gas and the flame front via the c variable which has to be smaller than 0.99 for activation. This is due to reasons of efficiency. The mesh in the fully burnt regions of the domain is set back to the coarse base mesh as this region does not influence flame acceleration.

After having elucidated the governing equations and the general solver architecture, the combustion modelling will be examined in the following section.

3.5 Combustion Modelling of Deflagration and Detonation

In the context of safety analysis in the chemical and process engineering, turbulent combustion modelling represents a central aspect as the investigated mixtures are charcterised by high flammability and explosion risks [22], [51], [115]. Turbulent combustion modelling itself poses major challenges due to the complexity of chemical kinetics, turbulence and their interaction. For most fuels, only reduced reaction mechanisms ([92], [99]) can be applied as a result of the demanding computational costs. A second drawback refers to the fact that ensemble-averaged reaction rates cannot be calculated from averaged flow quantities as this neglects turbulence-chemistry interaction. Turbulent temperature fluctuations, i.e. have a strong impact on the non-linear reaction rates. Therefore, a broad variety of combustion models has been developed depending on the needs of its specific combustion regime [126].

One commonly used category of turbulent combustion models comprises the mixing-related models. On the one hand, there is the Eddy-Breakup model (EBU) [121] which assumes infinitely fast chemsitry. The reaction rate is controlled by turbulent mixing exclusively and therefore fuel and oxidizer are assumed to be burnt once they are mixed. On the other hand, the chemical timescales dominate the reaction rate in the Perfectly-Stirred Reactor (PSR) model [126]. As a consequence, turbulent mixing is assumed very fast. A combination of these two methods leads to the Eddy-Dissipation Concept (EDC) model [42] allowing for reaction only if fuel and oxider are mixed on the small-

est turbulent scales. With the same intention, the PSR model can be extended by the so-called Partially-Stirred-Reactor (PASR) model. The reaction rate is controlled by the fraction of chemical and turbulent timescales [55]. This model has been successfully applied to the simulation of combustion in internal combustion engines [104] and is in principle capable of reproducing DDT. However, the PSR model is situated in the upper region of the Borghi diagram (Fig. 2.1) while the simulation of explosions in smooth geometries include a distinct phase of slow to medium fast flames, being located in the flamelet regime (Fig. 2.1). Hence, it is not suitable in the framework of this thesis. In addition, the need for a reaction mechanism would be computationally too expensive.

A different approach considers turbulence-chemistry interaction by using Probability Density Functions (PDF) [108] which are used to incorporate fluctuations of turbulent quantities. These functions are either presumed or determined from a transport equation. The reaction rates are eventually obtained from integrating the PDFs which is computationally costly. Moreover, changes in state caused by shock waves cannot be considered by this model, excluding its use in explosion simulations.

Combustion could also be represented by detailed chemistry. In combination with a suitable model for turbulence-chemistry interaction, like the PASR model, this methodology can reproduce DDT. However, as this approach includes a transport equation for each species, it is only feasible for small reaction systems like H_2 combustion [126]. The computational effort increases drastically for hydrocarbon fuels: for C_2H_4 more than 30 species and 250 reactions must be considered.

In conclusion, none of the presented models is perfectly suited for all combustion regimes which are relevant for explosion processes. Hence, an efficient and robust compromise to cover all relevant turbulent combustion regimes was found by Ettner [43] and Hasslberger [62]. The so-called reaction progress variable (c) approach [16], [126] is chosen to model turbulent combustion. Depending on the value of c, it is distinguished between educts ($c = 0$) and products ($c = 1$). Thus, only one transport equation needs to be solved which significantly reduces the computational costs compared to detailed chemistry.

In the Favre-averaged context, $\tilde{c}$ corresponds to the density-weighted probability of finding a burnt mixture at a location at a given time. The reaction progress variable field can then be used to compute the distribution of the individual species. The composition in partially-burnt cells is therefore linearly interpolated using c and lookup tables containing mass fractions for the fully burnt state. These tables depend on fuel content, temperature as well as pressure and are obtained from equilibrium calculations in Cantera [57]. The evaluation of numerically stiff (Arrhenius-like) source terms is avoided by using a TFC-like closure of the flamelet-like source term. However, since chemical reaction is not directly solved, the effects of pressure, temperature, composition, turbulence etc. need to be modelled. In summary, the proposed method is efficient and shows numerical robustness which is an important aspect for engineering-type simulations.

The transport equation for c is given by

$$\frac{\partial}{\partial t}\left(\overline{\rho}\tilde{c}\right) + \frac{\partial}{\partial x_j}\left(\overline{\rho}\tilde{u}_j\tilde{c}\right) = \frac{\partial}{\partial x_j}\left[\left(\overline{\rho}D_{\mathrm{eff}}\right)\frac{\partial \tilde{c}}{\partial x_j}\right] + \max\left(\dot{\omega}_{\mathrm{def}}, \dot{\omega}_{\mathrm{det}}\right). \tag{3.44}$$

Combustion models of this type are mainly used for the regimes of wrinkled flamelets and thin reaction zones (Fig. 2.1). Deflagrative flame acceleration in this work is mainly situated in these regimes, too. Combustion modelling in the context of this thesis essentially deals with the closure of the source term in Eq. 3.44, which is given by the maximum of a deflagration ($\dot{\omega}_{\mathrm{def}}$) and a detonation ($\dot{\omega}_{\mathrm{det}}$) source term. The evaluation of the maximum allows for a clear differentiation between deflagration and auto-ignition effects in the individual cells.

In order to account for turbulence-chemistry interaction, the modelling of the deflagration source term follows the so-called Turbulent Flame Speed Closure (TFC) approach [126]. This flame speed represents the propagation velocity of the turbulent flame brush and is dependent on several physical phenomena like quenching, intrinsic flame instabilities, turbulent flame wrinkling and the thermodynamic state.

However, by reaching the fast flame regime, which is located in the region of

broken reaction zones of the Borghi diagram (Fig. 2.1), the concept of a flame surface is no longer valid [25]. Auto-ignition effects become important and the flamelet model alone is not able to capture near sonic flame propagation during this stage. The local conditions resemble a perfectly-stirred reactor in each cell, limited by chemical kinetics but not turbulence anymore. One can therefore rather speak of a volumetric reaction in each cell. Hence, a volumetric formulation, incorporating a quadratic heat release function, is chosen to model auto-ignition effects and detonation.

In order to capture deflagrative flame acceleration from the slow flame to the fast flame regime (Fig. 2.2), the deflagration source term is incorporated in the pressure-based and the density-based solver. The detonation source term, however, is only implemented in the density-based architecture which is capable of reproducing the required gas dynamic effects. More detailed information on the modelling of the deflagration and the detonation source terms is provided in the following sections.

3.5.1 Modelling of the Deflagration Source Term

This section introduces the deflagration models, including the relevant phenomena from Sec. 2.2, to resolve deflagrative flame acceleration in smooth geometries. It is distinguished between $H_2/O_2/N_2$ and $C_2H_4/O_2/N_2$ mixtures in the individual sections. The essential difference refers to the calculation of the effective burning velocity S_{eff} (Sec. 3.5.1.4). Generally, the deflagration source term modelling is based on weak ignition, which is considered the most common accident scenario in chemical plants.

A gradient approach according to the TFC methodology is chosen, i.e. [154]

$$\dot{\omega}_{\text{def}} = \rho_{\text{u}} G \underbrace{\Psi S_{\text{L}}}_{S_{\text{eff}}} \left| \frac{\partial \tilde{c}}{\partial x_j} \right|, \tag{3.45}$$

which reduces the grid dependencies in the under-resolved framework [43]. Equation 3.45 considers the expansion of the reaction products as a function

of the unburnt density ρ_{u}. G accounts for the influence of quenching on the deflagrative flame accelaration caused by high turbulence intensities. S_{eff} denotes the effective burning velocity, obtained from the laminar flame speed S_{L} and multiple sub-models, respresented by Ψ for reasons of brevity. The modelling approaches for the individual parameters in Eq. 3.45 will be presented afterwards, starting with the methodology for the unburnt properties and the quenching model. This is followed by the laminar flame speed and the individual parameters of the burning law.

3.5.1.1 Calculation of the Unburnt Properties

All quantities in the deflagration source term (Eq. 3.45) are derived from the unburnt state of the mixture. The state of the unburnt mixture parameters changes continuously during flame acceleration due to the preconditioning caused by the emission of pressure waves by the flame and their accumulation to shocks. An accurate reproduction of the fresh gas preconditioning is indispensable as this determines the rate of flame acceleration and therefore if critical conditions for the onset of detonation are reached. Isentropic relations are computationally efficient. However, they are not able to fully capture the changes of state, in particular compression induced by shock waves. Therefore, a different approach is used in this work.

A second energy equation for the unburnt state of the mixture (Eq. 3.46) is implemented into the hybrid solver architecture. This equation solely incorporates changes of state caused by the flow and pressure field. No chemical reaction is considered. Hence, isentropic and non-isentropic changes are inherently included. Moreover, this procedure allows for considering the temporal evolution during the highly unsteady process of flame acceleration and DDT as well as local compression effects. In order to ensure a stable convergence behaviour, the governing equations (Sec. 3.3.1) may only be influenced indirectly by the second energy equation via the combustion modelling.

Thus, separate fields associated with the unburnt state variables T_u and ρ_u as well as the unburnt material properties:

- Dynamic viscosity μ_u
- Specific isobaric heat capacity $c_{p,\mathrm{u}}$
- Thermal conductivity λ_u
- Thermal diffusivity a_u

are determined in a first step.

In analogy to Eq. 3.30, the second energy equation for the unburnt state $e_{\mathrm{u,t}}$ is given by

$$\frac{\partial}{\partial t}\left(\bar{\rho}\widetilde{e}_{\mathrm{u,\,t}}\right)+\frac{\partial}{\partial x_j}\left(\left(\bar{\rho}\widetilde{e}_{\mathrm{u,\,t}}+\bar{p}\right)\widetilde{u}_j\right)=\frac{\partial}{\partial x_j}\left(\bar{\rho}\,a_\mathrm{eff}\,\frac{\partial\widetilde{h}_\mathrm{u}}{\partial x_j}+\bar{\tau}_{\mathrm{u},ij}\widetilde{u}_i\right), \tag{3.46}$$

which is iteratively solved for T_u. The procedure for the calculation of the remaining unburnt properties and the integration into the solver architecture is illustrated in Fig. 3.7. ρ_u is estimated from the ideal gas law, using T_u. The corresponding values for μ_u, $c_{p,\mathrm{u}}$, λ_u and a_u are subsequently calculated in the whole domain based on T_u. This methodology allows for considering also non-isentropic changes of state for these parameters which are required for the quenching and flame wrinkling sub-models of the deflagration source term. Moreover, a feedback effect of the unburnt quantities on the conservation equations solely exists via the combustion model.

μ_u is computed according to the mixture law of Wilke [145]

$$\mu_\mathrm{u}=\sum_i\frac{x_i\mu_i\left(T_\mathrm{u}\right)}{\sum_j x_j\phi_{ij}\left(T_\mathrm{u}\right)}. \tag{3.47}$$

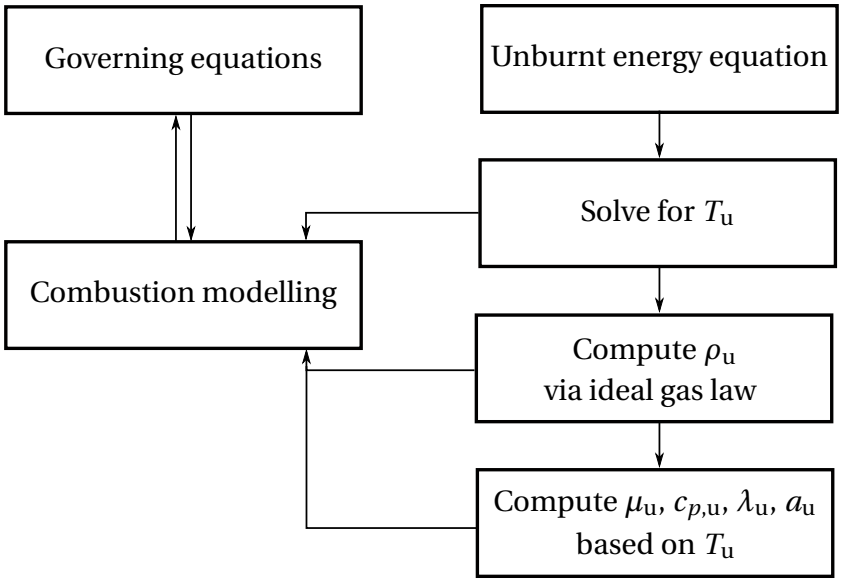

Figure 3.7: Schematic for the integration of the unburnt energy equation into the solver architecture.

Similar to the equation of Wilke [145], a mixture law for λ_u was defined by Wassiljeva, Mason and Saxena [107]

$$\lambda_\mathrm{u} = \sum_i \frac{x_i \lambda_i (T_\mathrm{u})}{\sum_j x_j \phi_{ij} (T_\mathrm{u})}. \tag{3.48}$$

Both correlations are based on an interaction parameter ϕ_{ij} for the multi-species fuel/oxidizer/diluent mixture, which uses the dynamic viscosities of a pair of species μ_i/μ_j and the respective molar masses M_i

$$\phi_{ij} = \frac{1}{2\sqrt{2}} \left(1 + \frac{M_i}{M_j}\right)^{-0.5} \left[1 + \left(\frac{\mu_i (T_\mathrm{u})}{\mu_j (T_\mathrm{u})}\right)^{0.5} \left(\frac{M_j}{M_i}\right)^{0.25}\right]^2. \tag{3.49}$$

In order to compute μ_u and λ_u of the mixture at run time, $\mu_{i,\mathrm{u}}(T_\mathrm{u})$ and $\lambda_{i,\mathrm{u}}(T_\mathrm{u})$ of the individual species are computed via polynomial expressions as

$$\begin{aligned}\mu_i (T_\mathrm{u}) = \Big(\exp\Big[&C_1 \left(\ln\left(T_\mathrm{u} \tfrac{1}{\mathrm{K}}\right)\right)^4 + C_2 \left(\ln\left(T_\mathrm{u} \tfrac{1}{\mathrm{K}}\right)\right)^3 - C_3 \left(\ln\left(T_\mathrm{u} \tfrac{1}{\mathrm{K}}\right)\right)^2 + \\ &C_4 \left(\ln\left(T_\mathrm{u} \tfrac{1}{\mathrm{K}}\right)\right) + C_5\Big]\Big)\,\mathrm{kg/ms}\end{aligned} \tag{3.50}$$

and

$$\lambda_i\left(T_\mathrm{u}\right) = \Big(\exp\Big[D_1\left(\ln\left(T_\mathrm{u}\tfrac{1}{\mathrm{K}}\right)\right)^5 D_2\left(\ln\left(T_\mathrm{u}\tfrac{1}{\mathrm{K}}\right)\right)^4 + D_3\left(\ln\left(T_\mathrm{u}\tfrac{1}{\mathrm{K}}\right)\right)^3 - D_4\left(\ln\left(T_\mathrm{u}\tfrac{1}{\mathrm{K}}\right)\right)^2 + D_5\left(\ln\left(T_\mathrm{u}\tfrac{1}{\mathrm{K}}\right)\right) + D_6\Big]\Big)\,\mathrm{W/mK}. \tag{3.51}$$

The polynomial expressions are obtained from mixture property calculations in Cantera [57], varying T_u. The coefficients of Eqs. 3.50 and 3.51 are given in App. A.2.

$c_{p,\mathrm{u}}$ is estimated using a mass weighted average

$$c_{p,\mathrm{u}} = \sum_i Y_i c_{p,i}\left(T_\mathrm{u}\right). \tag{3.52}$$

The $c_{p,i}$ of the individual components are calculated from the NASA-polynomials and the coefficients of the NIST-JANAF library from the O'Conaire reaction mechanism [99] for H_2 and the mechanism of Lu [92] for C_2H_4. Finally, a_u is obtained from the previously introduced quantities as

$$a_\mathrm{u} = \frac{\lambda_\mathrm{u}}{\rho_\mathrm{u} c_{p,\mathrm{u}}}. \tag{3.53}$$

3.5.1.2 Turbulent Flame Quenching

Generally, S_eff (Eqs. 3.69 and 3.88) increases with turbulence. However, Poinsot [126] showed that intensified mixing in the reaction zone causes flame quenching at high turbulence intensities. This motivates the introduction of a correction factor G to prevent an unrestricted growth of S_eff by the increasing turbulence level during flame acceleration. G represents the probability for the occurrence of unquenched flamelets and is formulated according to the model proposed by Zimont [154]. Specifically, G is expressed as an error function (erfc) [111] which depends on the dissipation rate ϵ:

$$G = \frac{1}{2}\mathrm{erfc}\left[-\frac{1}{\sqrt{2\sigma}}\left(\ln\left(\frac{\epsilon_{\mathrm{cr}}}{\epsilon}\right)+\frac{\sigma}{2}\right)\right]. \tag{3.54}$$

Here, σ represents the standard deviation of the log-normal distribution of ϵ, estimated as

$$\sigma = 0.26\ln\left(\frac{l_{\mathrm{T}}}{l_\eta}\right), \tag{3.55}$$

using the integral turbulent length scale l_{T} (Eq. 2.5) and the Kolmogorov length scale l_η (Eq. 2.7).

Furthermore, the critical dissipation rate ϵ_{cr}

$$\epsilon_{\mathrm{cr}} = 15\nu g_{\mathrm{cr}}^2 \tag{3.56}$$

depends on the kinematic viscosity ν and the critical flamelet quench rate g_{cr} which can be obtained from laminar flame calculations or from dimensional considerations as

$$g_{\mathrm{cr}} = \frac{S_{\mathrm{L}}^2}{a_{\mathrm{u}}}. \tag{3.57}$$

In case of low dissipation rates, no flame quenching occurs ($G = 1$), while at high dissipation rates ($\epsilon \gg \epsilon_{\mathrm{cr}}$), the flame quenches locally and $\dot{\omega}_{\mathrm{def}}$ vanishes.

3.5.1.3 Laminar Flame Speed

The laminar flame speed S_{L} represents a fundamental part of the deflagration source term. It strongly depends on the mole fraction (X_{fuel}) as well as on p and T_{u} which is accounted for by the power law expression [133]

$$S_{\mathrm{L}} = S_{\mathrm{L,ref}}(X_{\mathrm{fuel}})\left(\frac{T_{\mathrm{u}}}{T_{\mathrm{ref}}}\right)^{\alpha}\left(\frac{p}{p_{\mathrm{ref}}}\right)^{\beta}. \tag{3.58}$$

First, the laminar flame speed at reference conditions ($S_{L,ref}$ at 1 bar and 298 K) is calculated in each cell. Next, cell-averaged values for T_u and p are inserted into Eq. 3.58 to obtain the corrected laminar flame speed S_L. The correlations for $S_{L,ref}$ as well as the exponents for temperature and pressure, α and β respectively, are presented in the following sections for H_2 and C_2H_4. All polynomials have a limited range of validity, adapted to the cases investigated in the results chapter 4. It is distinguished between fuel/air and stoichiometirc fuel/O_2/N_2 mixtures in the following.

Laminar Flame Speed of H_2/O_2/N_2 Mixtures

$S_{L,ref}$ is a function of X_{H_2} and is computed by the following polynomial expression, introduced by Ettner [43] for H_2/air mixtures

$$S_{L,ref} = \left(-488.9 X_{H_2}^4 + 285.0 X_{H_2}^3 - 21.92 X_{H_2}^2 + 1.352 X_{H_2} - 0.04\right) \mathrm{m/s}. \tag{3.59}$$

The computed values for $S_{L,ref}$ are shown in Fig. 3.8 on the left for the range of validity between $X_{H_2} = 0.08 - 0.3$. Experimental data is included for validation. The stoichiometric H_2/air point is located at $X_{H_2} = 0.296$.

The corresponding expression for α depends on X_{H_2} and is retrieved from 1-D flamelet computations with Cantera [57] at various temperatures T_u

$$\alpha = 50.3552 X_{H_2}^2 - 32.3004 X_{H_2} + 6.9093. \tag{3.60}$$

The reaction mechanism of O'Conaire [99] is used as this mechanism has successfully been applied to the simulation of explosion processes by Ettner [43] and Hasslberger [62]. Inserting the expressions for $S_{L,ref}$ and α into Eq. 3.58 reveals that the flame speed S_L increases with increasing temperatures of the unburnt mixture. The pressure exponent β is kept constant at a value of 0.2 which corresponds to a stoichiometric H_2/air mixture. This infers that S_L decreases with increasing pressure levels. The influence of β on the global flame

propagation behaviour was proven to be small in comparison with α. Therefore, evaluation of an additional correlation for the calculation of β is avoided for reasons of efficiency.

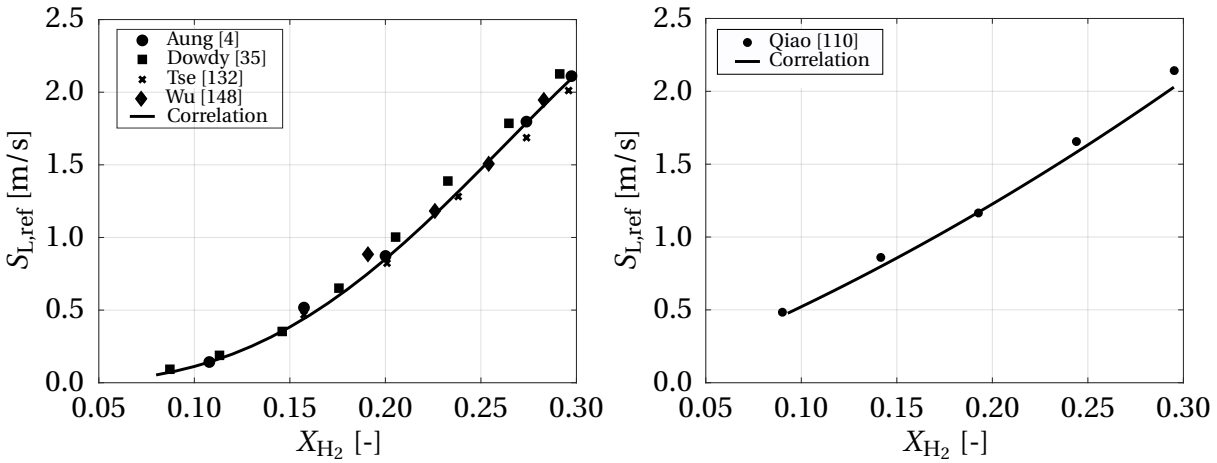

Figure 3.8: Laminar flame speed of H_2/air (left) and stoichiometric $H_2/O_2/N_2$ mixtures (right). Experimental data is included for comparison.

In chemical processes, stoichiometric $H_2/O_2/N_2$ mixtures are of particular interest with regard to the efficiency of chemical processes and the plant dimensions [114]. Therefore, a second correlation for $S_{L,ref}$ is obtained from the experimental data of Qiao [110] which explicitly accounts for stoichiometric conditions

$$S_{L,ref} = \left(20.0796 X_{H_2}^2 + 6.0740 X_{H_2} - 1.2829\right) \mathrm{m/s}. \tag{3.61}$$

The computed values are depicted in Fig. 3.8 on the right for the range of validity: $X_{H_2} = 0.08 - 0.3$. Similar as for the H_2/air mixtures, $S_{L,ref}$ increases continuously with X_{H_2} due to the decreasing amount of N_2 in air for increasing fuel content. Analogous to the H_2/air mixtures, a polynomial for α is retrieved from 1-D flamelet computations with Cantera [57] at various temperatures T_u, which reads

$$\alpha = 41.1038 X_{H_2}^2 - 27.0616 X_{H_2} + 6.1643. \tag{3.62}$$

β is again set to -0.2.

Laminar Flame Speed of $C_2H_4/O_2/N_2$ Mixtures

All polynomial expressions in this section are obtained from 1-D flamelet calculations in Cantera [57], using the reaction mechanim of Luo [92]. The calculation of S_L of C_2H_4 mixtures equals the procedure applied for H_2 mixtures and the reference conditions are identical to H_2 (1 bar and 298 K). $S_{L,ref}$ for C_2H_4/air mixtures with fuel contents between $X_{C_2H_4} = 0.03 - 0.15$ is given by

$$\begin{aligned} S_{L,ref} = \Big(&3.3623 \cdot 10^6 X_{C_2H_4}^6 - 3.0895 \cdot 10^6 X_{C_2H_4}^5 + 9.7449 \cdot 10^5 X_{C_2H_4}^4 - \\ &1.4132 \cdot 10^5 X_{C_2H_4}^3 + 9.8607 \cdot 10^3 X_{C_2H_4}^2 - 301.0784 X_{C_2H_4} + 3.3197\Big)\,\mathrm{m/s}, \end{aligned} \tag{3.63}$$

which is plotted in the left plot of Fig. 3.9 for increasing values of $X_{C_2H_4}$. Typically, the maximum value is slightly shifted to the rich side (stoichiometric point: $X_{C_2H_4}$=0.0655) [133]. Experimental data is included for validation. Qualitatively, the behaviour of $S_{L,ref}$ with respect to variations of p and T_u is similar the one of H_2 (Sec. 3.5.1.3).

The polynomial for α reads

$$\begin{aligned} \alpha = 5.3909 \cdot 10^4 X_{C_2H_4}^4 - 2.4377 \cdot 10^4 X_{C_2H_4}^3 + 3.9715 \cdot 10^3 X_{C_2H_4}^2 - \\ 269.4312 X_{C_2H_4} + 7.8632. \end{aligned} \tag{3.64}$$

Analog to H_2 (Sec. 3.5.1.3), β is set to the value at the stoichiometric C_2H_4/air point, which corresponds to -0.27.

Regarding stoichiometric $C_2H_4/O_2/N_2$ mixtures, the polynomial for $S_{L,ref}$ is formulated as

$$\begin{aligned} S_{L,ref} = \Big(&3.5839 X_{C_2H_4}^4 - 1.9326 X_{C_2H_4}^3 + 352.8108 X_{C_2H_4}^2 - \\ &3.6840 X_{C_2H_4} - 0.1405\Big)\,\mathrm{m/s}. \end{aligned} \tag{3.65}$$

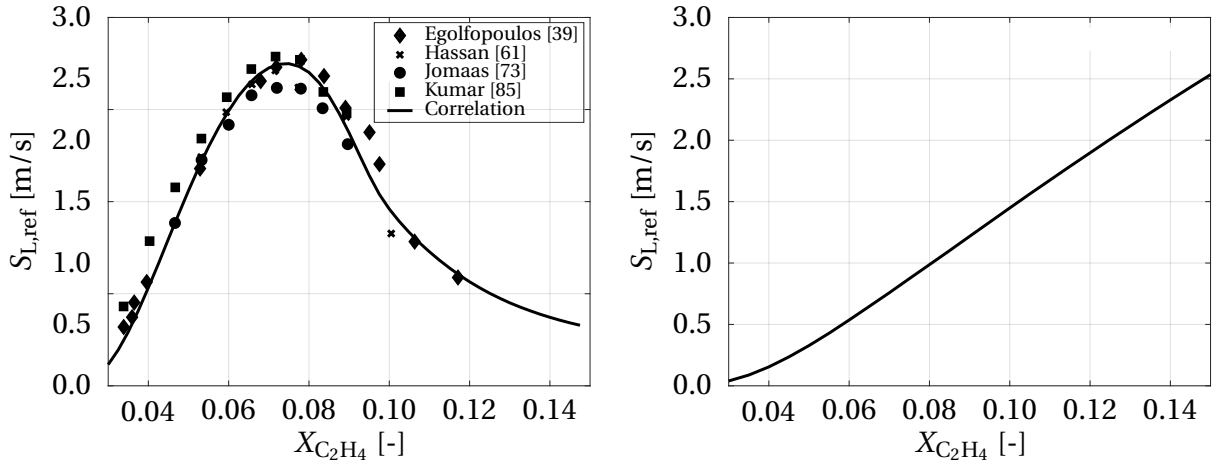

Figure 3.9: Laminar flame speed of C_2H_4/air (left) and stoichiometric $C_2H_4/O_2/N_2$ mixtures (right).

The computed values are illustrated in Fig. 3.9 on the right for the range of validity: $X_{C_2H_4} = 0.03 - 0.15$. No experimental data from literature is available for the stoichiometric mixtures, as typically C_2H_4/air mixtures are investigated. Hence, validation of the reaction mechanism applied in this work is carried out for the C_2H_4/air mixtures at various levels of T_u and p, depicted in App. A.3. Due to the fact that the computations agreed well with the experimental results for C_2H_4/air mixtures, the correlation for stoichiometric mixtures is used without further validation. Considering the uncertainties associated to the under-resolved grids, this assumption seems to be reasonable.

Finally, α is given by

$$\alpha = 6.5450 \cdot 10^3 X_{C_2H_4}^4 - 4.1740 \cdot 10^3 X_{C_2H_4}^3 + 959.3111 X_{C_2H_4}^2 - 94.7823 X_{C_2H_4} + 4.6328 \tag{3.66}$$

and β is set to -0.27.

3.5.1.4 Effective Burning Velocity

An interpretation for the effective burning velocity S_{eff} can be deduced from the concept of flame front enlargement due to turbulence, introduced by

Damköhler [29]. According to this theory, the flame surface grows due to turbulent flame wrinkling, as depicted in Fig. 3.10. This increases the burning velocity proportionally.

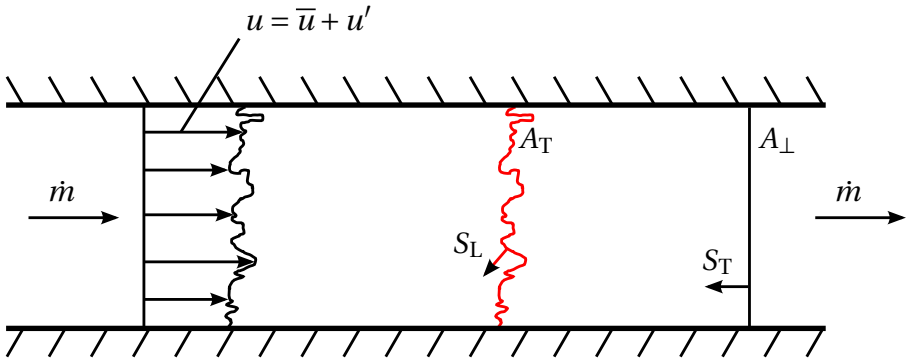

Figure 3.10: Topological interpretation of turbulent burning velocity. Turbulent flame coloured red (adapted from [106]).

This effect can be topologically explained by applying conservation of mass over the flame front in Fig. 3.10

$$\dot{m} = \rho_u A_T S_L = \rho_u A_\perp S_T = \text{const.} \tag{3.67}$$

where A_T is the instantaneous turbulent flame surface area and $A_\perp$ is the cross-sectional area. ρ_u cancels out, as both velocities are referring to the unburnt state. The ratio of the A_T and $A_\perp$ leads to

$$\frac{S_T}{S_L} = \frac{A_T}{A_\perp} = \Xi. \tag{3.68}$$

Hence, S_T represents the turbulent flame propagation velocity, resulting from surface growth due to turbulent flame wrinkling Ξ. In case of a planar laminar flame, $\Xi = 1$. In terms of the ensemble-averaging procedure, the areas are evaluated per unit volume in the control volume.

As the models for the calculation of the burning velocity used in this thesis

account for more than turbulent flame wrinkling, which is the dominant parameter though, the flame velocity in Eq. 3.45 is referred to as "effective".

Effective Burning Velocity of $H_2/O_2/N_2$ Mixtures

For the simulation of $H_2/O_2/N_2$ mixtures, S_{eff} is estimated according to the model of Katzy [77] who investigated the early stage of flame acceleration for lean H_2/air mixtures in the context of nuclear safety analysis. For the validation of the developed model, Katzy conducted flame acceleration experiments in a rectangular channel with smooth walls. This implies an initial low level of turbulence. Hence, the initial and boundary conditions are similar to the smooth geometries analysed in this thesis. However, notice that the work of Katzy focuses on lean mixtures, while stoichiometric to rich mixtures are the subject of interest in this work. This affects the model in a way that the influence of some effects - flame stretch and instability-based wrinkling - is smaller in the present thesis, as their impact increases for lean mixtures.

The model of Katzy to calculate S_{eff} reads [77]

$$S_{\text{eff}} = S_{\text{L}} \Xi_{\text{inst}} F_{\text{pressure}} F_{\text{grid}} \Xi_{\text{T}} F_{\text{stretch}} F_{\text{enclosure}}, \tag{3.69}$$

which follows a multiphenomena approach, based on the separation of the individual accelerating effects [149]. This concept employs the relation between flame surface and flame velocity (Eq. 3.68), which allows for including correlations to compute the relevant phenomena in the framework of under-resolved grids. The different terms in Eq. 3.69 represent phenomena influencing the effective value, which are listed below:

- S_{L} denotes the laminar flame speed, which is computed according to Sec. 3.5.1.3.
- Ξ_{inst} captures flame wrinkling induced by Landau-Darriues (LD) and thermal-diffusive (TD) instabilities. A pressure correction is added by F_{pressure}.

- F_{grid} takes the effect of the grid size into account.
- Ξ_{T} considers turbulent flame wrinkling.
- F_{stretch} accounts for flame stretch effects, induced by local flame front curvature.
- $F_{\text{enclosure}}$ is a geometrical model parameter, caused by flame containment.

Starting with Ξ_{inst}, all terms in Eq. 3.69 are explained in more detail subsequently.

Instability-Based Flame Wrinkling

Ξ_{inst} takes into account flame front enlargement by the LD as well as the TD instabilities (Sec. 2.2.2), using an effective Lewis number Le_{eff} approach

$$\Xi_{\text{inst}} = \Xi_{\text{inst,3D}} = \Xi^2_{\text{inst,2D}} = \text{Le}_{\text{eff}}^{-0.8}. \tag{3.70}$$

Differentiation between 2-D and 3-D wrinkling is required as the formulation was derived from 2-D experimental shadowgraphy data. Extending Ξ_{inst} to three dimensions by the power of two has been adopted from Driscoll [36]. The calculation of Le_{eff} follows the methodology of Bechtold and Matalon [12]

$$\text{Le}_{\text{eff}} = 1 + \frac{\text{Le}_{\text{E}} - 1 + \xi\,(\text{Le}_{\text{D}} - 1)}{1 + \xi}, \tag{3.71}$$

where $\text{Le}_{\text{E}} = 2.32$ and $\text{Le}_{\text{D}} = 0.33$.

The weighting factor ξ is defined as

$$\xi = \begin{cases} 1 + \text{Ze}\left(\frac{1}{\Phi} - 1\right) \text{ if } \Phi < 1 \\ 1 + \text{Ze}(\Phi - 1) \text{ if } \Phi \geq 1 \end{cases} \tag{3.72}$$

Here, Ze is the Zeldovich number which is given by

$$\mathrm{Ze} = \frac{E_\mathrm{A}\,(T_\mathrm{ad} - T_\mathrm{u})}{R T_\mathrm{ad}^2}, \tag{3.73}$$

where the global activation energy E_A has been set to 30 kcal/mol, as proposed by Sun [125]. Inserting Eqs. 3.72 and 3.73 in Eq. 3.71 for various fuel contents, one yields the following polynomial for Le_eff of $H_2/O_2/N_2$ mixtures with a fuel content between $X_{H_2} = 0.1 - 0.6$

$$\mathrm{Le}_\mathrm{eff} = 29.9953 X_{H_2}^3 - 3.3085 X_{H_2}^2 + 1.2066 X_{H_2} + 0.2806. \tag{3.74}$$

Katzy obtained a pressure dependency for the instability-based flame wrinkling as the effect strengthens for increasing pressure levels. The formulation is based on experimental and numerical investigations of the flame surface growth due to instabilities at various initial pressure levels and reads

$$F_\mathrm{pressure} = \left(\frac{p}{p_\mathrm{ref}}\right)^{0.14}. \tag{3.75}$$

p_ref amounts 1 bar. Regarding the process of flame acceleration and DDT, the pressure dependency is indispensable due to the continuously increasing pressure level. However, instability-based flame wrinkling is of prior importance for the acceleration stage directly after the ignition and for lean $H_2/O_2/N_2$ mixtures as Le_eff is significantly below unity for these mixtures.

Grid Influence

Due to the fact that the derivation of Ξ_inst is based on a reference grid size of $\triangle$ = 7.5mm, the grid resolution has a strong impact on this parameter (see Katzy [77]). Any deviation of the grid size from this value will cause a deviation in the result associated with Ξ_inst. The smaller (bigger) the cell size is, the smaller (bigger) is Ξ_inst due to the amount of flame wrinkling resolved. Therefore, Katzy carried out simulations with varying cell sizes in order to quantify this effect by the parameter F_grid.

The characteristic grid size can be retrieved from the cell volume via

$$\triangle = (\text{cell volume})^{\frac{1}{3}}. \tag{3.76}$$

Finally, F_{grid} is formulated in terms of a power law as

$$F_{\text{grid}} = \left(\frac{\triangle}{\triangle_{\text{ref}}}\right)^{0.16}, \tag{3.77}$$

in which $\triangle_{\text{ref}}$ is set to 7.5 mm. By multiplication of S_{eff} (Eq. 3.69) with the factor F_{grid}, the dependency of the simlation results on the cell size can be reduced.

Turbulent Flame Wrinkling

Turbulent flame wrinkling is incorporated by the model of Peters [105]

$$\Xi_{\text{T}} = 1 - \frac{0.39}{2}\frac{l_{\text{T}}}{l_{\text{L}}} + \left(\left(\frac{0.39}{2}\frac{l_{\text{T}}}{l_{\text{L}}}\right)^2 + 0.78\frac{u' l_{\text{T}}}{S_{\text{L,ref}} l_L}\right)^{0.5}, \tag{3.78}$$

which is valid in the whole flamelet regime of the Borghi diagram, shown in Fig. 2.1. The root mean square (r.m.s.) of the turbulent velocity fluctuations u' (Eq. 2.4) is used to account for additional flame wrinkling caused by an increasing turbulence level. Furthermore, the integral turbulent length scale l_{T} (Eq. 2.5) and the laminar flame thickness l_{L} (Eq. 2.1) are required to consider the length scales of turbulence and chemistry.

To capture the temporal development of the turbulence field, Ξ_{T} is used as the equilibrium source term (Ξ_{eq} in Eq. 3.81) of the flame wrinkling transport equation from Weller [139]

$$\frac{\partial}{\partial t}(\bar{\rho}\Xi) + \frac{\partial}{\partial x_j}\left(\bar{\rho}\Xi\widetilde{u}_j\right) = \frac{\partial}{\partial x_j}\left(\bar{\rho}D_{\text{eff}}\frac{\partial \Xi}{\partial x_j}\right) + \bar{\rho}P_{\Xi}\Xi - \bar{\rho}R_{\Xi}\Xi^2. \tag{3.79}$$

Conceptually, this model resembles the widespread flame surface density

models where the spatio-temporal evolution of the flame surface is explicitly tracked.

The production rate of flame wrinkling P_Ξ is given by [139]

$$P_\Xi = 0,28\sqrt{C_{u'}^3 \frac{\varepsilon}{\nu_\mathrm{u}}} \tag{3.80}$$

and the corresponding removal rate R_Ξ is

$$R_\Xi = \frac{P_\Xi}{\Xi_\mathrm{eq}}. \tag{3.81}$$

Further details on the model can be found in [43], [62], [139] and [140].

The utilisation of Eq. 3.79 for the turbulent flame wrinkling allows the consideration of local turbulence effects for the computation of S_eff (Eq. 3.69). Additionally, flame wrinkling is not limted to its equilibrium state. From a physical point of view, this is beneficial as the turbulence production and dissipation are far away from equilibrium state during the highly unsteady process of flame acceleration. The evolution of Ξ starts with a value of $\Xi = 1$ for laminar conditions. Initially, it increases due to the evolving flow and turbulence field, which is captured by the production term P_Ξ (Eq. 3.80). The magnitude of Ξ saturates towards a constant value during flame acceleration, caused by the removal rate R_Ξ (Eq. 3.81).

Flame Stretch

With reference to the work of Bradley [15], the effect of flame stretch - increase of the local laminar flame speed in convex parts of the flame front [77] - is included by the parameter F_stretch. Flame stretch K is defined as the rate of change of an incremental flame front surface element and consists of two parts: strain K_s and curvature κ [126]:

$$K = K_\mathrm{s} + \kappa. \tag{3.82}$$

Strain results from a non-uniform flow ahead of the flame front in form of tangential velocity gradients. Curvature is caused by the propagating curved flame front itself [126]. Due to the fact that flame and flow velocities are small during the initial acceleration phase, the impact of strain is neglected in the model of Katzy [77].

F_{stretch} represents the ratio of stretched to unstretched laminar flame speed, i.e.

$$F_{\text{stretch}} = \frac{S_{\text{L,s}}}{S_{\text{L,0}}} = (1 - \mathscr{L}\kappa)\,. \tag{3.83}$$

Here, $\mathscr{L}$ is the Markstein length which is a proportionality constant between stretched and unstretched laminar flame speed. The calculation of $\mathscr{L}$ is based on the equivalence ratio ϕ, validated by the experimental work from Taylor [128]

$$\mathscr{L} = \left(0.0007723\phi^3 - 0.002694\phi^2 + 0.003276\phi - 0.001383\right)\frac{1}{\text{m}}, \tag{3.84}$$

who investigated spherically expanding H_2 flames. The expression is valid for fuel contents between $X_{H_2} = 0.1 - 0.6$.

A formulation for κ was obtained by means of experimental and numerical investigations of a propagating flame front for varying fuel contents and pressure levels. κ is therefore computed from a reference value with a corresponding pressure correction [77]

$$\kappa = \kappa_{\text{ref}}\left(\frac{p}{p_{\text{ref}}}\right)^{0.55}. \tag{3.85}$$

κ_{ref} is set to 500 $\frac{1}{\text{m}}$ and $p_{\text{ref}} = 1$ bar. Variation of the fuel content did not influence κ_{ref} significantly and hence solely a pressure dependency is considered in Eq. 3.85. Similar to Ξ_{inst} (Eq. 3.70), the evaluation is based on 2-D experimental data and therefore correction to three dimensions is required [63]

$$\kappa_{3D} = \kappa_{2D}\frac{\pi}{2}. \tag{3.86}$$

Stretch effects have a significant impact for lean $H_2/O_2/N_2$ mixtures only, just as the instability-based flame wrinkling. Hence, the missing modelling approach for strain does not influence the results considerably for the stoichiometric mixtures investigated in the current thesis.

Flame Enclosure

The last term $F_{\text{enclosure}}$ in Eq. 3.69 can be considered a model parameter which is derived from geometrical observations as [77]

$$F_{\text{enclosure}} = 0.35\sigma. \tag{3.87}$$

The underlying enclosure effect by the containment occurs in channels or pipes and is also reported by Beauvais [11] and Burke [20]. Flame propagation takes place predominantly in one direction and therefore a finger-tip or tulip shaped flame front develops and the flame surface area is expected to be significantly larger than the cross sectional area of the geometry. The amount of burnt gas, which cannot escape the geometry, consequently produces an expansion flow downstream the flame front. This accelerating influence of the confinement on flame propagation is accounted for by the expansion ratio σ, as this paramter determines the amount of product volume stream. Hence, the accelerating effect of the expanding burnt gas across the flame front is considered based on the mixture concentration.

According to Katzy [77], this parameter must be specified individually for each investigated geometry, based on experimental validation data. Thus, depending on the geometry, $F_{\text{enclosure}}$ is either set to unity or $i\sigma$. For the scope of this thesis, $F_{\text{enclosure}} = 0.35\sigma$ for the smooth pipe cases. The prefactor is decreased in comparison to Katzy [77] which is explained by the inreased reactivity of the mixtures. Despite this simple approach to capture this enclosure effect, Katzy could reproduce flame acceleration under various process conditions

with a constant prefactor [77]. Moreover, the methodology is also capable of predicting the global flame propagation in this work for strongly differing process conditions by a constant value (see Sec. 4.1.2). Hence, the model seems to reproduce the corresponding effect reasonably.

Regarding the simulation of spherical geometries, however, the enclosure effect does not occur and $F_{\text{enclosure}}$ is set to unity.

Validation of the deflagration source term for $H_2/O_2/N_2$ mixtures is carried out using experimental flame-tip position x data from Goulier [58]. The early stage of flame acceleration in a 94 l sphere without obstacles is analysed for H_2/air mixtures at an initial pressure of 1 bar, an initial temperature of 293 K and three low levels of initial turbulence. Hence, the initial and boundary conditions are similar to the smooth pipe and sphere cases examined in this thesis (Chap. 4), except for the lower pressure. However, the influence of higher initial pressure levels in the present thesis is employed by the pressure corrections (Eqs. 3.75 and 3.85) in the calculation of S_{eff}. Two H_2 contents within the range of interest are selected for validation.

Fig. 3.11 illustrates the comparison between simulation (solid line) and experiment (dashed line) for a H_2/air mixture with 28 Vol.-% H_2 on the left and with 24 Vol.-% H_2 on the right, respectively. The initial turbulence levels are characterised by u' (Eq. 2.4) ($u' = 1.26\text{m/s}$, $u' = 2.08\text{m/s}$, $u' = 2.81\text{m/s}$). As the investigations focus on the early acceleration phase, solely the pressure-based solver is used. Excellent agreement between the measured and computed flame-tip position data can be observed for each case considered. Therefore, the applied combustion modelling for the deflagration source term as well as the pressure-based algorithm is well-validated. The small discrepancies for the cases with the lowest turbulence levels and 24 Vol.-% H_2 can be attributed to the dissipative nature of the pressure-based solver and the related smearing of gradients, slowing down flame acceleration.

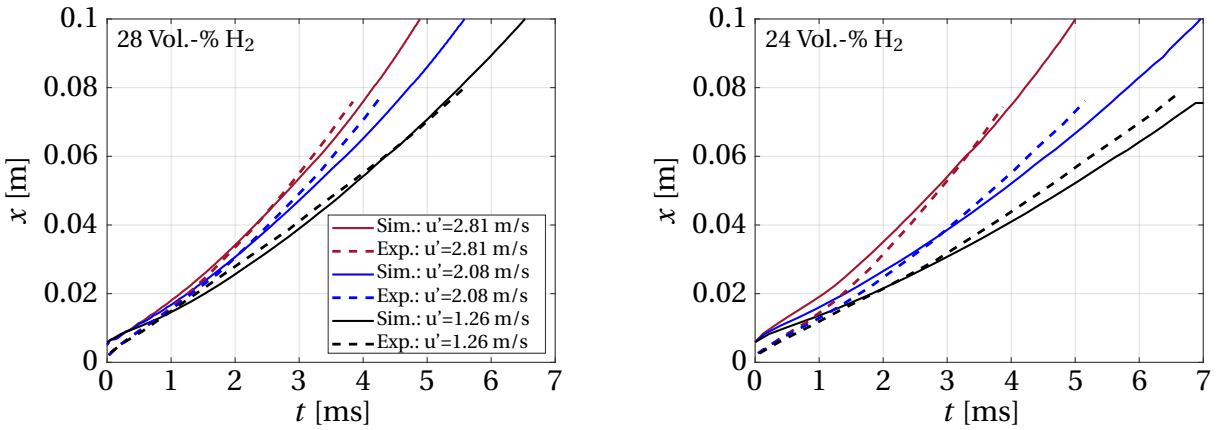

Figure 3.11: Validation of deflagration source term for $H_2/O_2/N_2$ mixtures with experimental flame-tip position data from Goulier [58]. Results for a mixture with 28 Vol.-% H_2 are shown on the left for varying initial turbulence levels and for a mixture with 24 Vol.-% H_2 on the right, respectively (dashed lines indicate the experimental data).

Effective Burning Velocity of $C_2H_4/O_2/N_2$ Mixtures

For the simulation of $C_2H_4/O_2/N_2$ mixtures, the basic structure of the deflagration source term (Eq. 3.45) is equal to the previous section. Solely the model for the calculation of S_{eff} has to be changed. The applied formulation reads

$$S_{\text{eff}} = S_{\text{L}} \Xi. \tag{3.88}$$

A suitable correlation - considering the relevant physical phenomena - for the flame wrinkling parameter Ξ was obtained by Muppala [97] for C_2H_4 mixtures, based on the experimental data of different C_2H_4 flames. Ξ is computed as [97]

$$\Xi = 1 + \frac{0.46}{\text{Le}_{\text{eff}}} \text{Re}_{\text{T}}^{0.25} \left(\frac{u'}{S_{\text{L}}} \right)^{0.3} \left(\frac{p}{p_{\text{ref}}} \right)^{0.2}, \tag{3.89}$$

which is applied as the equilibrium source term in the flame wrinkling transport equation of Weller [139] (Eq. 3.79). To account for the enhanced flame

wrinkling with increasing turbulence, the turbulent Reynolds number $\mathrm{Re_T}$ (Eq. 2.9) and the fluctuation velocity u' (Eq. 2.4) are incorporated. In addition, intrinsic flame instabilities (LD and TD) are considered by $\mathrm{Le_{eff}}$, given by

$$\mathrm{Le_{eff}} = -1.0248 X_{\mathrm{C_2H_4}}^3 - 0.2822 X_{\mathrm{C_2H_4}}^2 + 3.0531 X_{\mathrm{C_2H_4}} + 0.2717. \tag{3.90}$$

Eq. 3.90 is valid between $X_{\mathrm{C_2H_4}} = 0.03 - 0.15$ and is derived from Cantera [57] calculations with the reaction mechanism of Luo [92], following the methodology of Bechtold and Matalon [12] (Eq. 3.71). The influence of pressure on flame wrinkling is also considered in Eq. 3.89, where $p_{\mathrm{ref}} = 1$ bar.

In order to validate the deflagrative combustion modelling for $\mathrm{C_2H_4/O_2/N_2}$ mixtures, experimental flame-tip position x data from Chaudhuri [23] is used. Chaudhuri investigated the early stage of flame acceleration for a mixture with 8.34 Vol.-% $\mathrm{C_2H_4}$ in a 1.3 l cylindrical vessel without obstacles. Multiple initial states of pressure (1 bar, 2 bar, 3 bar, 5 bar) and turbulence ($u' = 1.43$m/s, $u' = 2.85$m/s) were considered. Hence, the experimental conditions are similar to the cases examined in this work.

The comparison between the computed results (solid line) and the experimental data (dashed line) is depicted in Fig. 3.12. Solely the pressure-based solver is applied due to the focus on the early acceleration phase. Generally, good agreement with the experimental results is achieved. However, the flame acceleration of the lowest reactive cases at 1 bar and $u' = 1.43$ m/s, $u' = 2.85$ m/s is lower in the simulation. This can be attributed to the dissipative nature of the pressure-based solver and the related smearing of gradients, slowing down flame acceleration. Nevertheless, the modelling approach is proven to be well-suited.

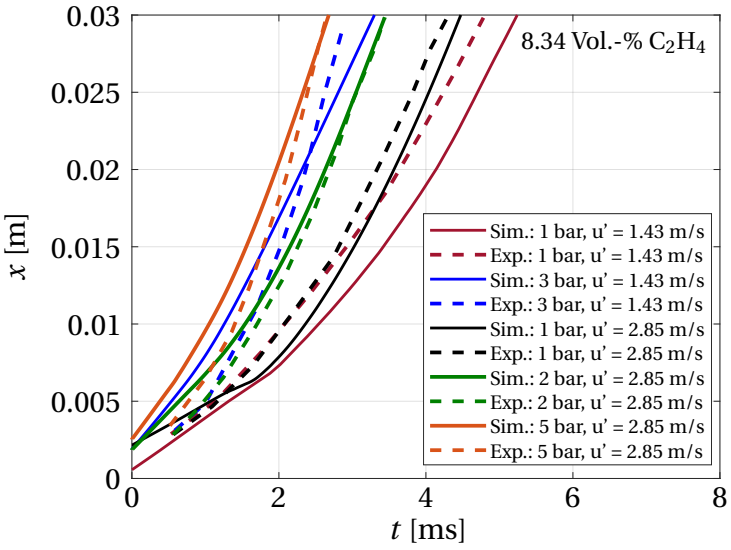

Figure 3.12: Validation of deflagration source term for $C_2H_4/O_2/N_2$ mixtures with experimental flame-tip position data from Chaudhuri [23]. Results for a mixture with 8.34 Vol.-% C_2H_4 are shown for varying initial pressure and turbulence levels (dashed lines indicate the experimental data).

3.5.2 Modelling of the Detonation Source Term

As turbulent flame wrinkling is bounded by quenching at high turbulence intensities, deflagrative flame acceleration is limited in the fast flame regime (Fig. 2.2). Therefore, auto-ignition effects become particularly important to reproduce near-sonic flame acceleration and to reach conditions, critical for the onset of a detonation. It is assumed that the local conditions resemble a perfectly-stirred reactor in each cell at high levels of turbulence due to the intensified mixing. In order to account for this mechanism in the simulations, a volumetric detonation source term (Eq. 3.93) is incorporated into the density-based solver [62]. The underlying methodology comprises a two-step mechanism, following the approaches of Colin [28] and Michel [95]. Modelling of the detonation source term therefore resembles the ZND structure (Fig. 2.9). The first step refers to the creation of a critical amount of radicals in the wake of the leading shock wave. This time interval is denoted as the induction or ignition

delay time, which is considered by the parameter τ (Eq. 3.91) in the modelling of the detonation source term. The second stage represents the exothermal heat release caused by the combustion. This is incorporated by a quadratic heat release function (Eq. 3.93) in accordance with the ZND theory.

The detonation modelling approach employs tabulated chemistry, which is beneficial in terms of efficiency. First, this methodology avoids solving a separate transport equation - including Arrhenius-type source terms - for each species. Second, stiff chemistry calculations - meaning that the chemical time scales are considerably smaller than the flow time scales - do not limit spatial and temporal CFD discretisation.

The dimensionless ignition delay time τ is introduced as

$$\tau = \frac{t}{t_{\text{ign}}\left(T, p, Y_{\text{fuel}}\right)} = \frac{Y}{Y_{\text{cr}}}, \tag{3.91}$$

which compares the current simulation time t with the pre-tabulated ignition delay times t_{ign}. τ can therefore be interpreted as a measure for the critical amount of radicals Y_{cr} which is required for auto-ignition effects to occur in the system. When Y_{cr} is attained, the energy is released within a short period.

τ is obtained by solving the following transport equation [43]

$$\frac{\partial}{\partial t}\left(\overline{\rho}\tilde{\tau}\right) + \frac{\partial}{\partial x_j}\left(\overline{\rho}\tilde{\tau}\,\tilde{u}_j\right) - \frac{\partial}{\partial x_j}\left(\overline{\rho} D_{\text{eff}} \frac{\partial \tilde{\tau}}{\partial x_j}\right) = \frac{\overline{\rho}}{t_{\text{ign}}}, \tag{3.92}$$

to account for the temporal evolution of temperature and pressure which have a strong impact on the t_{ign}. Moreover, convective and diffusive transport of radicals between cells is considered.

The t_{ign} are calculated from 0-D isochoric explosion calculations in Cantera [57] using the Shock and Detonation (SD) toolbox [44]. Ignition delay is defined as the time interval until the inflection point of the temperature curve is reached. Regarding H_2 mixtures, the O'Conaire reaction mechanism [99] is used while the mechanism of Lu [92] is applied for C_2H_4 mixtures. Tabulation

is carried out according to T, p and Y_{fuel}, which is assumed superior in comparison to correlations for the case of large temperature and pressure variations. Correlations of the form $t_{\text{ign}} \sim T^{\alpha} p^{\beta}$ are not able to capture the related changes of the reaction paths [89]. The computed multi-dimensional lookup tables are provided to the solver for interpolation in each cell of the simulation domain during run time.

As illustrated in Fig. 3.13, the t_{ign} are a highly non-linear function of temperature and pressure. In the upper part, the t_{ign} of two $H_2/O_2/N_2$ mixtures with 25.0 Vol.-% H_2 (left) and 29.56 Vol.-% H_2 (right) are shown at four pressure levels (1 bar, 5 bar, 10 bar and 50 bar). Accordingly, two $C_2H_4/O_2/N_2$ mixtures with 6.55 Vol.-% C_2H_4 and 10.0 Vol.-% C_2H_4 are depicted in the lower part at the same pressures. The fuel contents and pressure levels comprise typical conditions investigated in Chap. 4. However, the influence of the fuel content is small, while the t_{ign} decrease strongly with increasing temperature for elevated pressures. As the activation of the detonation source term (Eq. 3.93) is mainly triggered by t_{ign} ($\mathrm{H}(\tau - 1)$), the activation tends to happen earlier than in the experiment. Specifically, this refers to H_2 mixtures which show a strong decrease at pressure levels of 1 bar and 10 bar already. For C_2H_4 mixtures, there is a more gradual decrease.

In the context of under-resolved simulations, the cell-averaged temperature T instead of the unburnt temperature T_{u} is used for looking up the $t_{\text{ign}}(T, p, Y_{\text{fuel}})$. This represents a required modelling approach as T_{u} does not reach auto-ignition temperatures due to the smearing of pressure waves and shocks on the coarse grids and by the pressure-based solver.

Similar to the ZND theory (Fig. 2.9) [31], [137], [153] Hasslberger modelled the exothermic heat release by a quadratic function in the detonation source term [62]

$$\dot{\omega}_{\text{det}} = \theta \frac{2\mathrm{B}}{t_{\text{exo}}} c\,(1-c)\,\mathrm{H}(\tau - 1)\,\mathrm{H}(T - T_{\text{Trans}})\,, \tag{3.93}$$

which is extended by a temperature criterion $T - T_{\text{Trans}}$ in this thesis. This restriction in combination with the parameter θ is applied to model the von

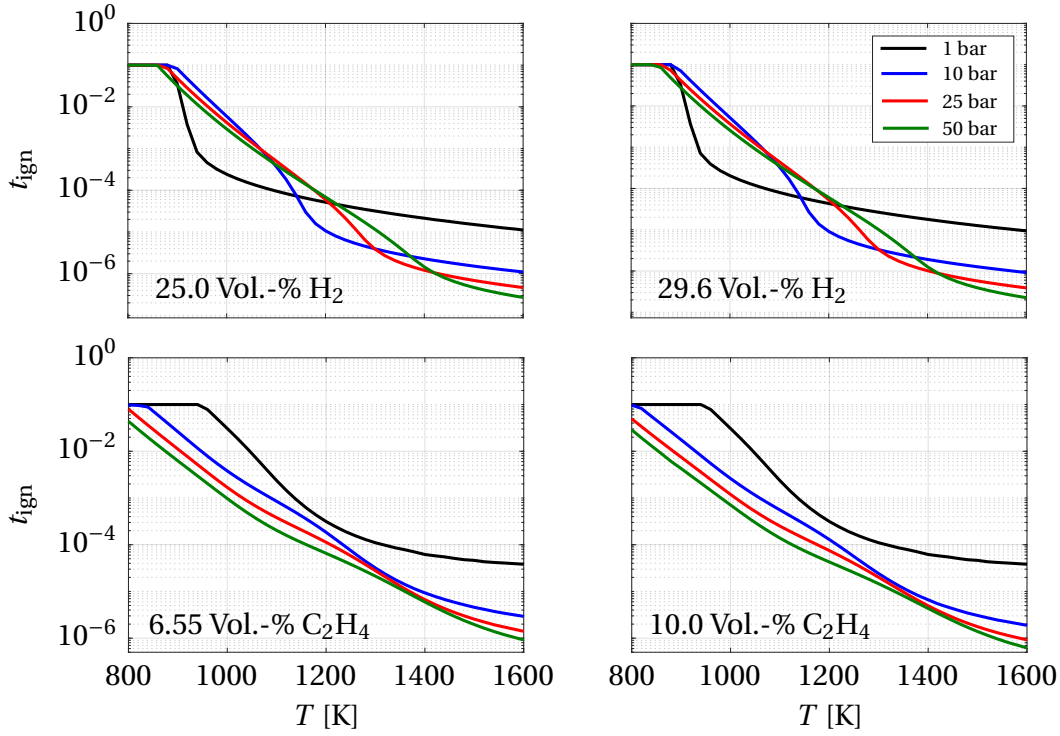

Figure 3.13: Ignition delay times over temperature for two $H_2/O_2/N_2$ mixtures (upper part) and two $C_2H_4/O_2/N_2$ mixtures (lower part) at various pressure levels.

Neumann spike (Fig. 2.9) which cannot be resolved on the under-resolved grids. The solver is therefore not able to distinguish between the leading shock and the reaction zone within computational cells. However, modelling of the von Neumann spike is essential to correctly compute the global flame propagation behaviour as well as the characteristic pressure levels.

θ prevents the heat from being released until the maximum pressure peak has passed, which is characterised by the temporal derivative of the pressure

$$\theta = \max\left(\theta; \mathrm{H}\left(-\frac{\partial p}{\partial t}\right)\mathrm{H}\left(\tau - 1\right)\right). \tag{3.94}$$

If the temporal pressure gradient becomes negative, intending that the von Neumann spike and the leading shock wave have passed, θ becomes unity. Otherwise, θ is zero. By using the maximum function, θ remains unity, once

the criterion is fulfilled. This behaviour is important because the reaction may require more than one time step.

In addition, to prevent an early heat release, T_{Trans} is set to the temperature at the von Neumann spike. Without this criterion, activation of the detonation source term is triggered too early for the stoichiometric mixtures at elevated pressures, investigated in the current thesis. T_{Trans} is computed from 0-D Cantera [57] calculations, using the SD toolbox [44]. To allow for preconditioning of the fresh gas to be considered, T_{Trans} is tabulated as a function of T_{u}, p and Y_{fuel}. T_{Trans} is consequently evaluated in each flame front cell at every time step. This ensures spatial separation of the leading shock and the subsequent reaction zone in the flame front cells within the under-resolved framework.

Activation of the detonation source term is realised if the t_{ign} become small. Hence, $\tau = 1$ and the Heaviside function becomes unity. Moreover, B is a model constant, set to a value of 4.5951, which results from the condition that the maximum amount of heat is released at $c = 0.5$. For further details on the detonation source term modelling, the interested reader is referred to Hasslberger [62].

The detonation source term modelling of Ettner [43], which incorporates the so-called Min.-Max. model, is not considered in this thesis due to the drawbacks outlined by Hasslberger [62]. The implemented sub-grid reconstruction of pressure waves and shocks is computationally costly in 3-D simulations. Additionally, the linear heat release function does not follow the ZND theory and is likely to produce overshoots in the c field which require an undesired artificial bounding methodology.

The calculation of the detonative reaction time t_{exo} is adapted in comparison to the original formulation from Hasslberger $t_{\mathrm{exo}} = 15\triangle t$ [62]. A constant value in the form $t_{\mathrm{exo}} = i\triangle t$ shows significant deficits for the strongly differing process conditions in this work. This shortcoming concerns in particular C_2H_4 mixtures, involving a more complex chemistry than H_2. In the present thesis, t_{exo} describes the time span, the detonation complex needs to pass a cell and is modelled as

$$t_{\mathrm{exo}} = (1-c)\,\frac{\triangle}{\mathrm{D_{CJ}}}, \tag{3.95}$$

using the characteristic cell size $\triangle$ and the Chapman-Jouguet velocity $\mathrm{D_{CJ}}$ [21], [76]. An illustration is given in Fig. 3.14. The burnt part of a cell ($c = 1$ in Fig. 3.14) is considered by $(1-c)$ in Eq. 3.95. Hence, t_{exo} represents the time interval, the stable detonation complex, propagating at $\mathrm{D_{CJ}}$, needs to pass the unburnt part of a cell ($c = 0$ in Fig. 3.14). The values for $\mathrm{D_{CJ}}$ are obtained from Cantera [57] calulcations with the SD toolbox [44] and are tabulated according to T_{u}, p and Y_{fuel} to consider preconditioning of the fresh gas. By analysing the timescales provided by the t_{exo} model, it turns out that the ZND theory [31], [137], [153] provides timescales in the same order of magnitude for the exothermic heat release (10e-6s-10e-7s). As the two-step formulation of the detonation source term modelling resembles the ZND theory, the presented methodology for computing t_{exo} is well-suited for the current work.

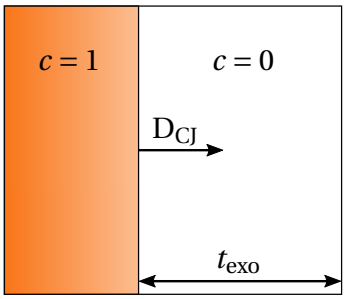

Figure 3.14: Schematic of the t_{exo} model for the calculation of the characteristic detonative reaction time.

In order to validate the detonation source term modelling and the density-based solver architecture, one dimensional detonation propagation simulations are performed. The simulation domain represents a 10 m long smooth channel with a cell size of 2.0 mm. Stoichiometric mixtures of H_2 and C_2H_4 with air are initialised at 293 K and elevated pressures at 12 bar and 8 bar, respectively. Strong ignition at one end of the channel is realised by patching the CJ state of the mixture.

Four different formulations for the calculation of t_{exo} are compared with each other in Fig. 3.15: the previously presented model (Eq. 3.95) and the approach

of Hasslberger [62], using three prefactors ($5\triangle t$, $10\triangle t$, $30\triangle t$). Verification is carried out by means of the stable propagation velocity, which is compared with the CJ velocity D_{CJ} of the mixture. In addition, being one of the most important output parameters, the pressure distributions are compared with characteristic pressure levels from the ZND theory (Fig. 2.9): the von Neumann spike p_{vN}, the CJ pressure p_{CJ} and the pressure at the end of the Taylor expansion wave p_{Tay}. All values were calculated with Cantera [57], using the SD toolbox [44].

Regarding the results for the propagation velocity of the stoichiometric H_2 mixture (top left), D_{CJ} can be reproduced well by the t_{exo} model (Eq. 3.95). Considering the approach of Hasslberger [62], it turns out that the prefactor has to be large enough to meet D_{CJ}, as there exists a boundary behaviour for large values of the prefactor. This is also reported in [62]. However, looking at the propagation velocities for C_2H_4 mixtures (top right), there exists a large spread for the investigated prefactors and no asymptotical behaviour can be observed. In addition, the propagation behaviour is non-physical for high values of $i\triangle t$. Only the t_{exo} model (Eq. 3.95) is able to correctly predict the propagation speed. Hence, the model from Hasslberger works for H_2 mixtures but loses applicability for more complex fuels.

Comparing the pressure data, predicted by the t_{exo} model, with the theoretical values, excellent agreement is observed for both fuels. All characteristic pressure levels from one dimensional theory can be reproduced. The modelling of the von Neumann spike by means of θ and $T - T_{Trans}$ works well. The pressure oscillations for the stoichiometric C_2H_4 mixture result from the more complex chemistry. The tabulated chemistry in terms of D_{CJ} and the underresolved grids are not able to fully capture all chemical processes and possible reaction paths, causing heat release fluctuations. This is also reflected in the propagation velocity of C_2H_4, while it does not occur for H_2.

In conclusion, the presented methodology to account for detonation propagation and auto-ignition effects by a volumetric detonation source term is proven to be a robust approach which is capable of predicting the global detonation propagation behaviour correctly. The developed t_{exo} model captures the timescales of detonative heat release for both fuels investigated in this the-

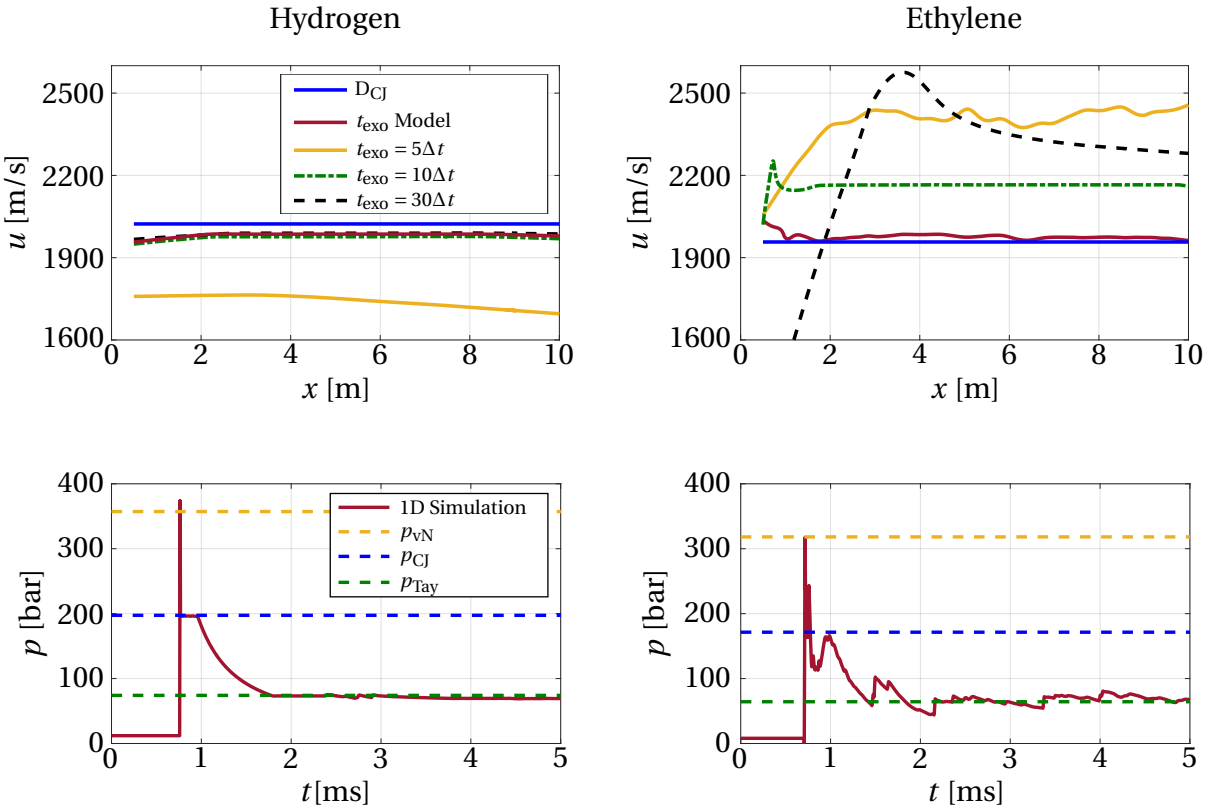

Figure 3.15: Validation of t_{exo} model and detonation source term for H_2 (left) and C_2H_4 (right) mixtures using one dimensional detonation simulations. Propagation velocity and pressure distribution are used for verification of the applied methodology.

sis without any tuning parameter. Extension towards other fuels can be realised by computing and tabulating D_{CJ} with a suitable reaction mechanism. However, the applicability of the tabulated chemistry for complex fuels has to be reevaluated.

4 Results and Discussion

In order to validate the hybrid pressure-/density-based solver developed in this work, smooth pipes of varying size and a 20 l sphere are considered. Therefore, two different types of flame propagation: quasi 1-D propagation in the smooth pipes and 3-D propagation in the sphere are used for the validation. The general objective is to correctly predict the global flame propagation behaviour of stoichiometric $H_2/O_2/N_2$ and $C_2H_4/O_2/N_2$ mixtures and to identify critical mixtures and conditions with respect to the occurrence of DDT.

4.1 Smooth Pipes

For the smooth pipes, the CFD results are evaluated based on the computed DDT locations. Due to the small number of repetitions of the individual experiments, statistics cannot be captured. Thus, the target of a successful prediction is set to lie within +/- 25 % of the experimental DDT location. Since DDT itself includes a stochastic behaviour [69] and experimental DDT locations varied up to 30 % for experiments with the same initial conditions, the confidence interval seems to be reasonable.

In literature, the DDT location is generally referred to as the position where the flame reaches a speed in the order of the speed of sound of the reaction products a_{pr} [25]. This is followed by a sharp increase in flame velocity and a related kink in the flame-tip position x over time t diagram. Referring to the definition of the experimental DDT locations from Schildberg [115], [116], however, this method cannot be applied to the investigated cases in the current thesis. The experimental DDT locations are retrieved from the maximum plastic deformation of the pipe, which is directly related to the maxmimun occurring pressure load. Hence, maximum simulation pressure following the character-

istic kink is taken for validation of the solver architecture. The peak pressure is determined from the pressure distribution along the pipe wall. In the following, the numerical setup and the results for stoichiometric $H_2/O_2/N_2$ and $C_2H_4/O_2/N_2$ mixtures will be presented.

4.1.1 Numerical Setup

Fig. 4.1 shows the computational domain for the smooth pipe cases. Solely the marked quarter of the pipe is computed in order to reduce the computational costs. Hence, symmetry boundary conditions are applied. The initial grid size is set to 2.0 mm, allowing for the simulations to be run on Linux workstations with 64 cores. The computational domain is discretised by hexahedral cells such that a preferably uniform mesh is assured in order to reduce the discretisation error. The resolution of first principle combustion simulations is usually given relative to the laminar flame thickness l_L which is out of the scope for the large geometries considered in the current work. However, in terms of safety analysis, the focus is at examining worst case scenarios. Thus, predicting the global flame propagation behaviour correctly is of praticular importance. This does not require resolving the micro-structure of all underlying processes as the subsequent results will demonstrate. Moreover, referring to the CFL criterion (Eq. 3.38), the temporal discretisation limits the grid size, too. Thus, level 1 refinement with 2 buffer layers is used for the AMR, being a reasonbale compromise in terms of efficiency and accuracy.

The wall boundaries are set to be adiabatic with a no-slip condition. Due to the large velocities associated to explosion processes, heat losses to the wall are assumed to be negligible. Homogeneous Neumann boundary conditions are imposed for all remaining transported quantities.

In the context of under-resolved simulations, a certain level of inital turbulence is required. This is due to the smoothening of gradients by the coarse grids and the pressure-based solver. Hence, the expansion of the ignition kernel and the initial pressure built-up are smaller than in the experiment. This deficit accordingly slows down flame acceleration, which needs to be compensated by a minimum level of initial turbulence to capture

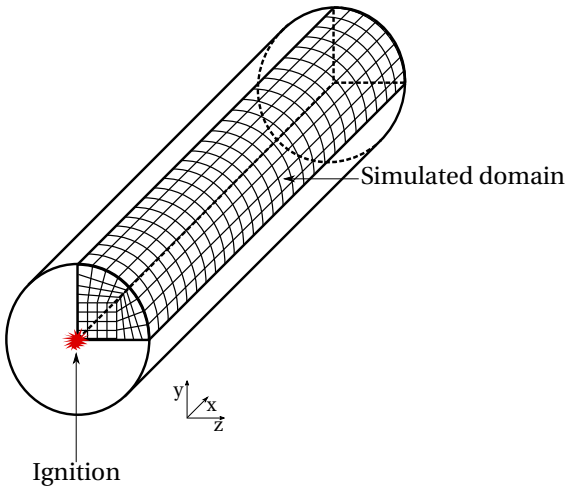

Figure 4.1: CFD grid of smooth pipe. Only marked quarter is simulated.

the initial phase of flame acceleration. Therefore, the initial values of the turbulence-characterising quantities k and ω are chosen at uniform values of $k = 0.1\ \mathrm{m^2/s^2}$ and $\omega = 100$ Hz. The values are identical for all simulations. Furthermore, the wall functions from OpenFOAM [141] for k and ω are applied. Temperature T of the initially quiescent mixture is set to 293 K, while pressure p is set according to [115], depicted in Tab. 4.1. Flame wrinkling Ξ is initialised with a value of unity.

Ignition of the mixture is realised by setting its state to burnt within a spherical volume in the first time step at one end of the pipe, centred on its axis. In comparison to patching the burnt state during the initialisation [43], [62], the heat release caused by ignition is considered. Additionally, this ensures a certain independence of the simulations from the initial turbulence level. This is due to the fact that the equations of the turbulence model are solved before the burnt state is set within the ignition kernel. Thus, most of the initial turbulence - characterised by k - is dissipated by the prescribed value of ω. The turbulence level at the time of ignition is consequently always almost the same, regardless of the initial level.

4.1.2 $H_2/O_2/N_2$ Mixtures

Validation of the investigated stoichiometric $H_2/O_2/N_2$ mixtures is carried out by means of experimental DDT locations from Schildberg [115]. For these stoichiometric mixtures, the air is diluted with nitrogen. A summary of the initial conditions and geometrical dimensions is given in Tab. 4.1.

Table 4.1: Smooth pipe experimental conditions for stoichiometric $H_2/O_2/N_2$ mixtures, taken from Schildberg [115].

Case	X_{H_2}	Initial pressure	Pipe diameter	Pipe length	DDT Exp.	DDT Sim.
H13	0.236	12.00 bar	48.3 x 2.6 mm	9.48 m	-	-
H14	0.256	12.00 bar	48.3 x 2.6 mm	9.48 m	3.98 m	3.60 m
H15	0.276	12.00 bar	48.3 x 2.6 mm	9.48 m	3.58 m	2.73 m
H2	0.296	12.00 bar	48.3 x 2.6 mm	9.48 m	2.93 m	2.38 m
H27	0.276	4.50 bar	114.3 x 3.6 mm	6.35 m	6.35 m	5.25 m
H26	0.286	4.50 bar	114.3 x 3.6 mm	6.35 m	5.38 m	4.96 m

For each case evaluated in the following, flame-tip position x over time t data and the corresponding flame-tip velocity v over position x data will be analysed. In addition, the pressure distribution and the evolution of the flame shape will be investigated for selected cases.

Experimental x-t data is available for the cases H13, H15, H14 and H2 in Tab. 4.1, while for the two cases in the larger pipe (H26, H27) only the DDT location can be referred to for validation. Photodiodes were used to experimentally determine x along the pipe axis during deflagrative flame acceleration (up to 2.2 m) and piezo-electric pressure sensors were installed in the rear part of the pipe to monitor x during detonation propagation [143].

First, the computed results for the purely deflagrative case H13 are compared with the measurements in Fig. 4.2. The transition between the pressure- and the density-based solver τ_{trans} takes place at 19.73 ms. Good agreement is achieved for both, x-t data (left) and v-x data (right). The flame shows continuous acceleration due to the mechanisms described in Sec. 2.2, but critical conditions for DDT and detonation propagation are not reached. This is in-

dicated by the subsonic velocities with respect to the reaction products' state. However, looking at the v-x diagram, auto-ignition effects start to take place

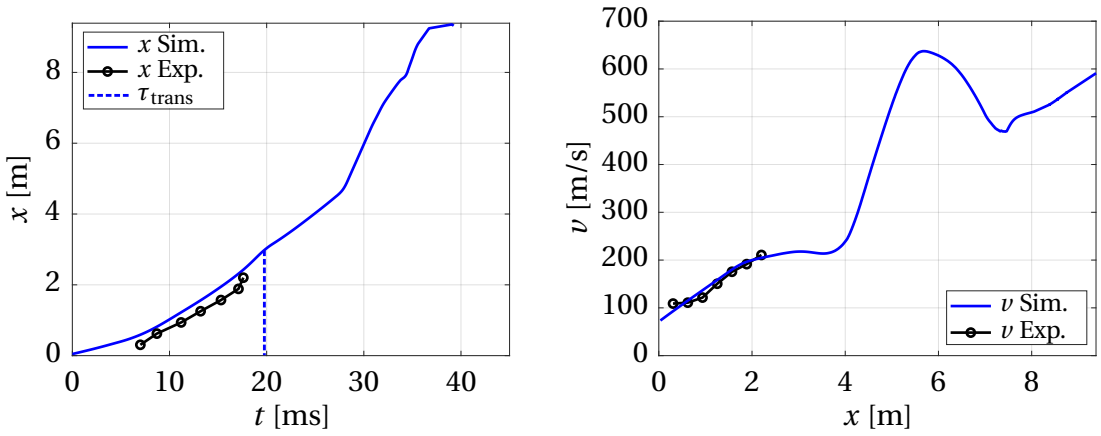

Figure 4.2: Flame-tip position x (left) and flame-tip velocity v (right) of case H13 (simulation: blue line; experiment: black line with dots). τ_{trans} (blue dashed line) at 19.73 ms.

at 4 m, strongly increasing v. The associated characteristic kink is located at this position in the x-t diagram. Nevertheless, back-running pressure waves are limiting flame acceleration and therefore flame propagation remains deflagrative in accordance with the experiment. a_{pr} at 810 m/s is not reached, which is considered a necessary criterion for DDT [25].

From the perspective of plant design, this case is of particular importance as it represents the lower DDT boundary. Correct prediction of this boundary is an essential validation aspect. In case no DDT is predicted by the simulation, substantial components of explosion safety could be avoided for the design of the plant. Nonetheless, confirmation by different safety assessment methods and stable process conditions is required, too.

Fig. 4.3 depicts the numerical and experimental results for flame-tip related quantities of case H14: x-t data (left) and v-x data (right). Again, good agreement with the measured values is observed. Comparing the results with case H13 (Fig. 4.2), the influence of the higher fuel content (X_{H_2}=0.256) on flame acceleration is highlighted. The increased reactivity of the mixture intensifies flame acceleration. As a consequence, τ_{trans} appears earlier at 14.79 ms. The flame accelerates gradually up to the kink at 3.55 m, while the expansion of the

products, instabilities and turbulence production in the boundary layer dominate the early stage. With increasing flame and flow velocities, shear layers

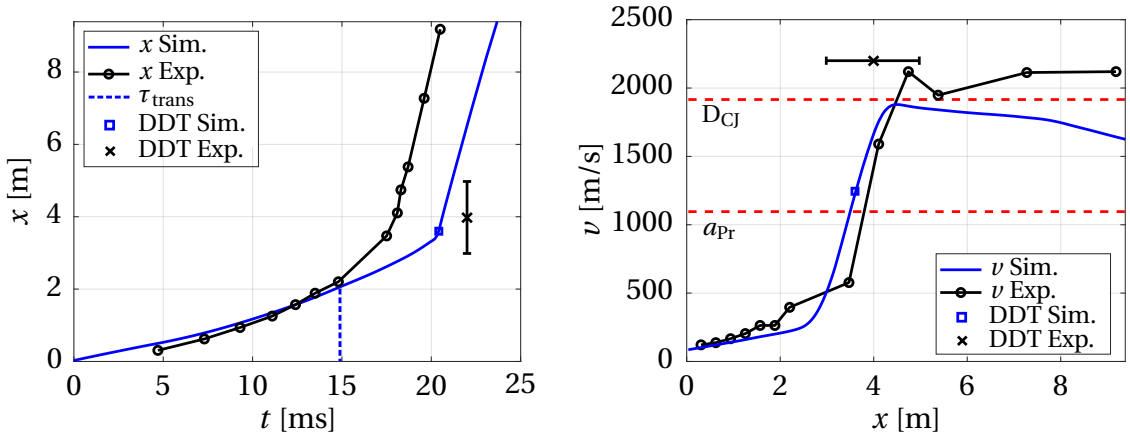

Figure 4.3: Flame-tip position x (left) and flame-tip velocity v (right) of case H14 (simulation: blue line; experiment: black line with dots). DDT location indicated by black cross with confidence interval (experiment) and blue square (simulation). D_{CJ} and a_{pr} indicated by red dashed lines. τ_{trans} (blue dashed line) at 14.79 ms.

develop in the bulk flow. This enhances turbulence production and turbulent flame wrinkling in this area. The kink at 3.55 m highlights the development of a sonic flame. DDT retrieved from the maximum pressure along the pipe wall emerges at 3.6 m which is within the confidence interval of the experimental DDT location at 3.98 m. In the subsequent detonative regime, a linear dependence of x on t exists. This denotes a constant flame speed, which is characteristic for detonative flame propagation. The smaller gradient in the simulative x-t data implies a smaller detonation velocity, which is confirmed by the v-x diagram on the right.

The Chapman-Jouguet velocity D_{CJ} (Eq. 2.23) and a_{pr} are included in the v-x graph in Fig. 4.3. v increases gradually up to $\approx$ 2.75 m where first autoignition effects occur. Enhanced flame acceleration in the following triggers DDT when the flame reaches a velocity in the order of a_{pr} (sonic regime), which is in agreement with previous experimental findings [25]. Afterwards, the detonation accelerates up to D_{CJ} and relaxes in the simulation while propagating along the pipe. The overdriven detonation in the experiment, exceed-

ing D_{CJ}, cannot be reproduced. This results from the under-resolved framework and the associated numerical diffusion. Moreover, the smaller preconditioning of the fresh gas due to the smearing of pressure waves and shocks on the coarse grids and by the pressure-based solver explains the smaller propagation velocity.

Generally, timescales in the simulation are overpredicted and therefore the computed positions are delayed in time in comparison with the experiment. This delay is associated with the ignition modelling which is a shortcoming in the context of under-resolved simulations in combination with a reaction progress variable c approach (Eq. 3.44). Temperatures in the simulation are limited to the adiabatic flame temperature ($c = 1$) while the temperatures after experimental ignition are higher due to the ignition energy and reaction of the fresh gas. Thus, expansion of the flame front is larger in the experiment, which leads to the emission of stronger pressure waves. Consequently, preconditioning of the fresh gas and flame acceleration are higher in the experiment. Therefore, the unburnt quantities and the laminar flame speed are lower in the simulation, which reduces flame acceleration.

Further increasing the fuel content to X_{H_2}=0.276 in case H15 shifts the DDT location upstream as depicted in Fig. 4.4. τ_{trans} is equally shifted in time due to the increased reactivity. The flame propagation behaviour, however, is similar to case H14. Regarding the x-t data on the left, the same acceleration characteristics exist. This includes the delay, resulting from the ignition, and the kink. DDT takes place at 2.73 m, which matches the confidence interval of the experimental DDT location at 3.58 m.

Regarding the v-x diagram in Fig. 4.4 on the right, the initiation of autoignition effects from 1.75 m on is again apparent in terms of the strongly increasing velocity. The onset of detonation appears when the flame reaches the sonic regime. In accordance with case H14, the detonation accelerates up to D_{CJ} and relaxes to a value below D_{CJ} at which it propagates along the pipe. This results from the aforementioned smaller preconditioning of the fresh gas and the numerical diffusion on the under-resolved grids.

Flame acceleration of case H2, being a stoichiometric H_2/air mixture, is anal-

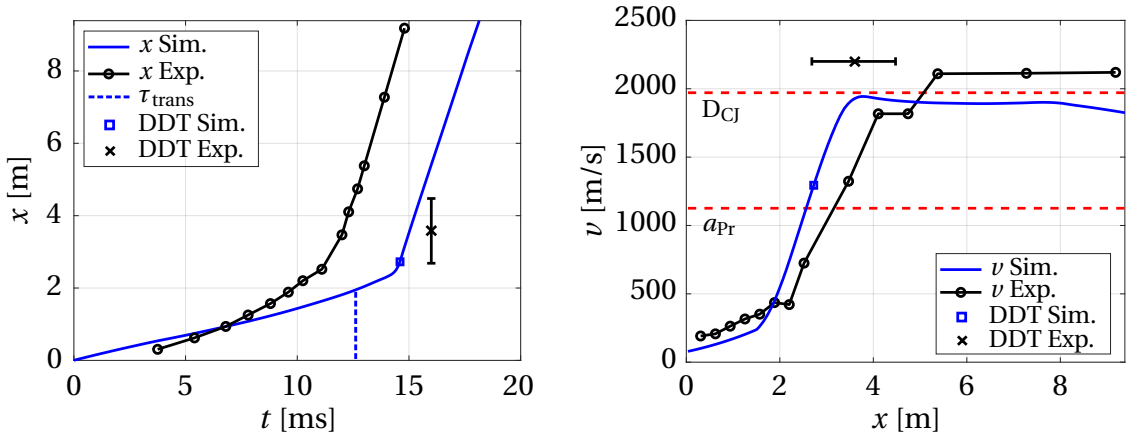

Figure 4.4: Flame-tip position x (left) and flame-tip velocity v (right) of case H15 (simulation: blue line; experiment: black line with dots). DDT location indicated by black cross with confidence interval (experiment) and blue square (simulation). D_{CJ} and a_{pr} indicated by red dashed lines. τ_{trans} (blue dashed line) at 12.82 ms.

ysed in more detail, starting with x-t (left) and v-x data (right) in Fig. 4.5. The computed results of case H2 resemble cases H14 and H15. The propagation behaviour is similar as the initial and boundary conditions are identical. Thus, the increased reactivity (X_{H_2}=0.296) enhances the acceleration rate and shifts the DDT location upstream. Good agreement with the experimental data is achieved. τ_{trans} takes place at 6.01 ms. As a positive gas dynamic and fluid dynamic feedback loop establishes, the flame front accelerates continuously, indicated by the steepening gradient in the x-t data. DDT is triggered at 2.38 m, which is located within the confidence interval of the experimental DDT at 2.93 m.

DDT is again observed at a velocity close to a_{pr}, which peaks at D_{CJ}. As was to be expected from the under-resolved framework, the overdriven detonation cannot be predicted and the detonation propagation speed is lower than the experimental value and D_{CJ}.

In order to analyse the global flame propagation behaviour in more detail, the evolution of the flame shape is investigated by means of the c field in the following. Fig. 4.6 illustrates the flame front on a vertical plane along the horizon-

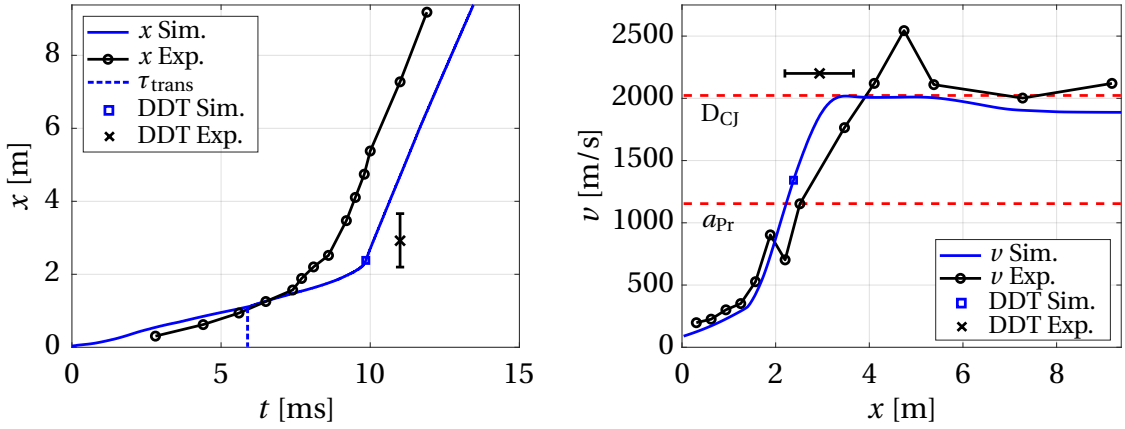

Figure 4.5: Flame-tip position x (left) and flame-tip velocity v (right) of case H2 (simulation: blue line; experiment: black line with dots). DDT location indicated by black cross with confidence interval (experiment) and blue square (simulation). D_{CJ} and a_{pr} indicated by red dashed lines. τ_{trans} (blue dashed line) at 6.01 ms.

tal pipe axis. Only half of the pipe height is shown. The wall is located at the bottom of the individual plots in Fig. 4.6. Typical stages of flame acceleration as reported by Ciccarelli [25] (Fig. 2.4) are observed:

- Initially, the flame expands spherically, not shown here, as the ignition source is located centrally at a distance of 35 mm from the left pipe end [115]. This stage is dominated by the expansion of the reaction products, instability-based flame wrinkling and flame stretch effects.

- A finger-tip shaped flame front develops at 2 ms due to the no-slip boundary condition.

- The flame induces a flow in the fresh gas by the continuously emitted pressure waves, which leads to the formation of a boundary layer. More precisely, the interaction of the flow with the wall enhances turbulence production in that zone, increasing turbulent flame wrinkling. Accordingly, the effective burning velocity S_{eff} and flame acceleration increase in the wall area. This process is highlighted by the flame shape changes at 3 ms and 4 ms in Fig. 4.6.

- A tulip-shaped flame front evolves at 4.6 ms in accordance with the experimental findings by Krivosheyev [83] and Kuznetsov [86] for H_2 flame propagation in smooth pipes. Moreover, the induced flame wrinkling by turbulence and gas dynamics can be seen at 4.6 ms.

In conclusion, the applied hybrid numerical methodology is capable of reproducing the characeristic stages of H_2 flame propagation in smooth pipes within the framework of under-resolved simulations.

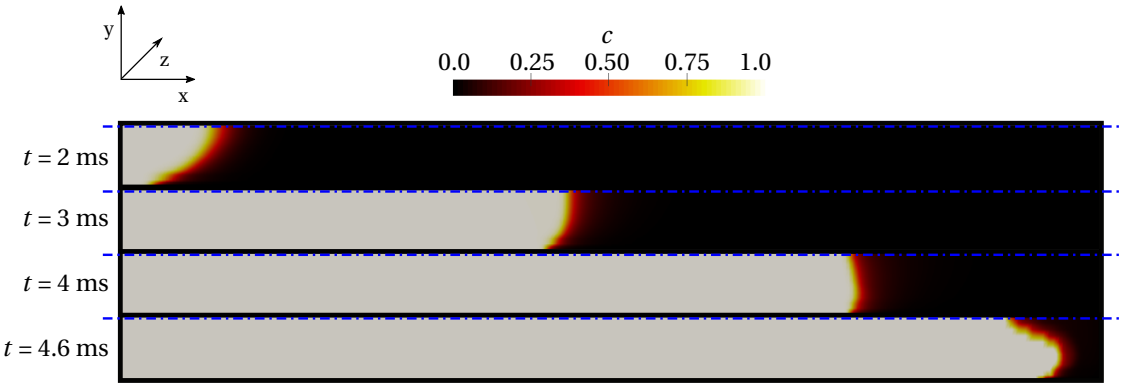

Figure 4.6: Flame propagation of case H2 between 2 ms and 4.6 ms on a vertical plane along the horizontal pipe axis, illustrated by the c field. Only half of the pipe height is shown. Pipe middle axis at the top of the pictures of the individual plots in time.

The pressure distribution of case H2 at multiple sensor locations along the pipe wall are compared with the experimental data from Schildberg [115] in Fig. 4.7. As the other investigated cases exhibit in principle a similar pressure/distance/time behaviour, this comparison is considered representative for all investigated H_2 cases. Simulation data is shifted in time to match the experimental DDT location. Thus, the delay associated with the ignition is eliminated.

An intrinsic shortcoming of the under-resolved framework and the pressure-based solver architecture refers to the fact that pressure waves and shocks are smeared out and therefore the absolute peak values can typically not be reproduced by the simulation. Nevertheless, a good qualitative and quantitative agreement for the remaining parts of the pressure data is achieved.

A pressure peak develops as a consequence of the ignition and the subsequent expansion of the reaction products, which is captured from the sensor location at 0.94 m on in Fig. 4.7. Due to the preconditioning of the fresh gas, pressure waves are accumulating which strengthens the peak while propagating along the pipe. However, the pressure-based solver in combination with the ignition modelling deficits and the under-resolved grids is not able to capture this peak during the early deflagration stage. From the sensor location at 2.2 m on, formation of a small pressure peak is captured in the simulation as a result of the switch to the explicit density-based solver.

The strong pressure peak in the simulation from 2.84 m on is attributed to the detonation as DDT has taken place at 2.38 m. The propagation velocities of the detonation and back-running pressure waves from the pipe end agree well for simulation and experiment in the following. While propagating towards the pipe end, the detonative pressure peak varies in both, experiment and simulation due to relaxation - indicated by the decreasing velocity in Fig. 4.5 (right) - and the interaction with reflected pressure waves from the pipe walls and the pipe end.

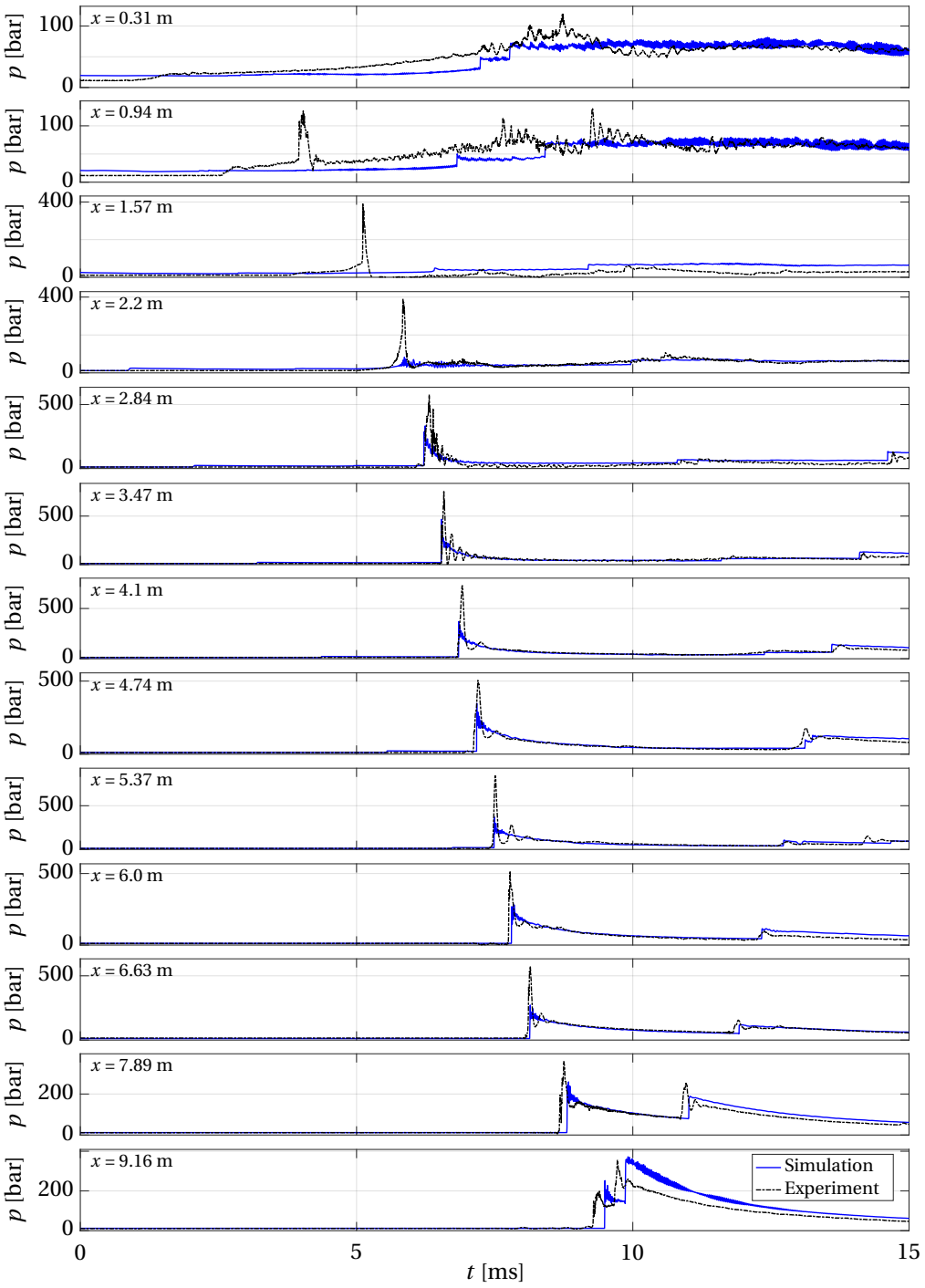

Figure 4.7: Comparison of experimental pressure data of case H2 (black dashed line) and simulation pressure (blue line) at experimental pressure sensor locations. Simulation data is shifted in time to match the pressure peak to the experimental DDT location (2.93 m).

In order to validate the solver for a broad range of geometries and initial conditions, cases H26 and H27 are additionally considered. The pipe diameter is increased and the length is reduced for these cases (Tab. 4.1). As aforementioned, no experimental flame-tip data is available and therefore validation is limited to the DDT location.

Even though cases H26 and H27 exhibit high fuel contents (Case H26: X_{H_2}=0.286, Case H27: X_{H_2}=0.276), the location of DDT is shifted downstream in comparison to the cases in the smaller pipe. This is explained by two reasons: On the one hand, the run-up distance is generally assumed to be roughly proportional to the inner pipe diameter for equal initial conditions (p, T). On the other hand, the lower initial pressure decreases turbulent flame wrinkling and delays auto-ignition.

Regarding the x-t diagram (left) and the v-x diagram (right) of case H27, depicted in Fig. 4.8, the experimental DDT is observed at the pipe end which cannot be reproduced by the solver. The computed DDT takes place at 5.25 m, shortly after the solver transition at 23.46 ms. However, this case exhibits the same flame propagation behaviour as the previous cases. DDT is located in the sonic flame regime and the detonation propagation speed is in the order of D_{CJ}. An explanation for the discrepancies to the experiment is given at the end of this section. Nevertheless, the computed DDT location is still within the confidence interval. In addition, this case does not represent a typical explosion scenario in chemical plants as the pipes are typically assumed to be much longer than the run-up distance to DDT. Therefore, the onset of detonation is triggered before the flame front reaches the pipe end in reality.

Regarding the computed results of case H26 in Fig. 4.9, the DDT location at 4.96 m agrees well with the experimental confidence interval around the measured value at 5.38 m. τ_{trans} appears at 16.93 ms. Apart from that, the acceleration behaviour is identical to the other cases. v increases gradually and significant auto-ignition effects are indicated by the kink in the x-t diagram where a linear dependence on time is observed afterwards. Moreover, the detonation reaches D_{CJ} and relaxes to a value below D_{CJ} while propagating along the pipe.

Similar to all configurations investigated for the stoichiometric $H_2/O_2/N_2$ mix-

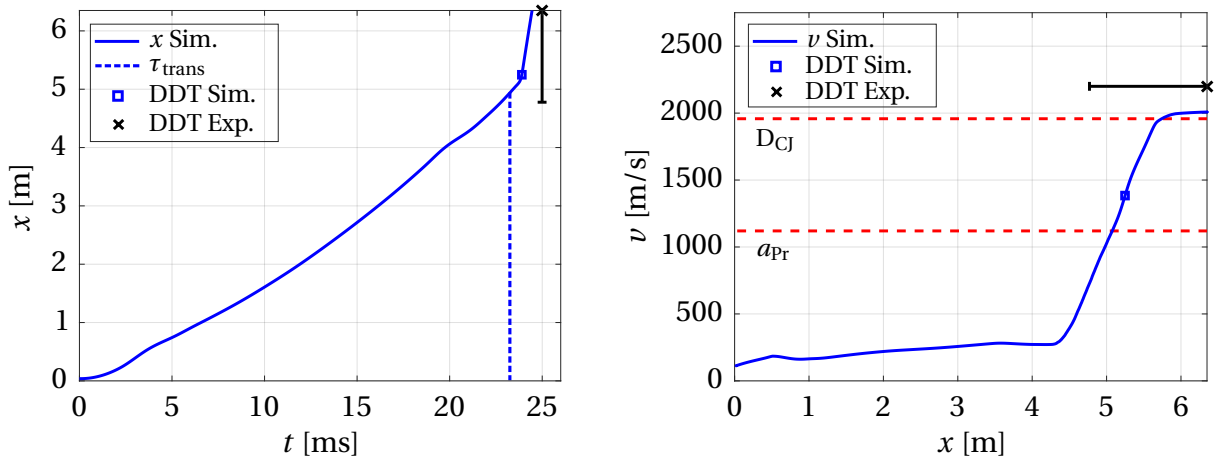

Figure 4.8: Flame-tip position x (left) and flame-tip velocity v (right) of case H27. DDT location indicated by black cross with confidence interval (experiment) and blue square (simulation). D_{CJ} and a_{pr} indicated by red dashed lines. τ_{trans} (blue dashed line) at 23.46 ms.

tures, DDT occurs earlier in the simulation than in the experiment. This is due to the dependence of the t_{ign} on pressure. The t_{ign} in Fig. 3.13 exhibit a strong decrease over temperature for elevated pressure levels. Considering $H_2/O_2/N_2$ mixtures, this is already critical at pressure levels of 1 bar and 10 bar. As mentioned in Sec. 3.5.2, the under-resolved grids require the cell-averaged temperature T to be used for looking up the t_{ign} as a result of the smaller preconditioning. However, due to the smearing of the c field in flame front cells on the coarse grids, local activation of the detonation source term is triggered in partially-burnt cells ($c > 0.5$). Hence, DDT tends to happen earlier in the simulations, where critical conditions are likely to occur in individual cells close to the flame front. In addition, the increased initial pressure level and subsequent pressure built-up exacerbate this mechanism. This also explains that the DDT at the pipe end in case H27 cannot be predicted. The detonation source term is activated in several cells after the solver transition and therefore DDT is immediately triggered as the flame velocity is close to the sonic regime.

In conclusion, the developed numerical methodology is capable of predicting the global flame propagation behaviour of stoichiometric $H_2/O_2/N_2$ mixtures

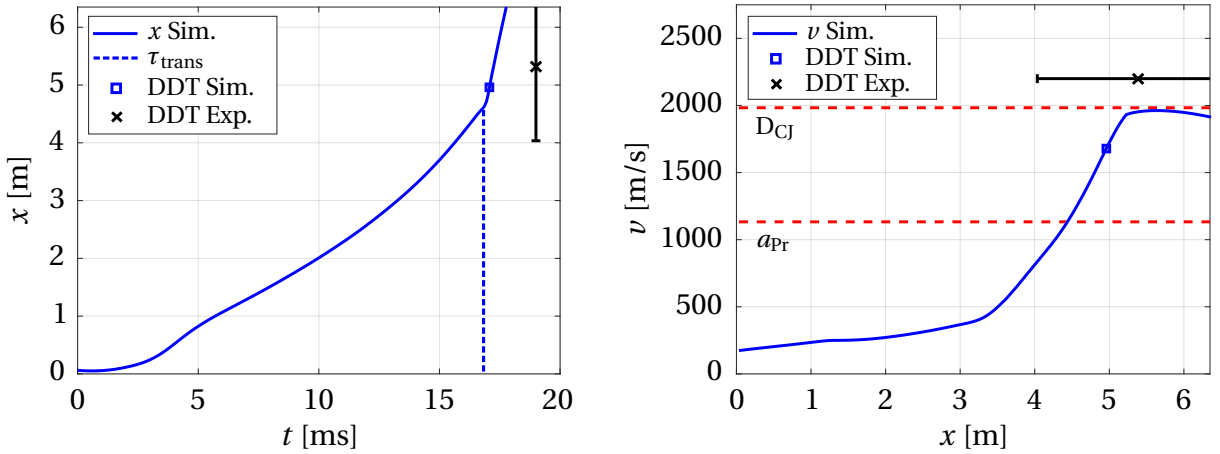

Figure 4.9: Flame-tip position x (left) and flame-tip velocity v (right) of case H26. DDT location indicated by black cross with confidence interval (experiment) and blue square (simulation). D_{CJ} and a_{pr} indicated by red dashed lines. τ_{trans} (blue dashed line) at 16.93 ms.

and its characteristic stages in smooth pipes at various initial conditions. The DDT location is reproduced within the defined confidence interval of the experimental DDT location for the investigated cases. Furthermore, the lower DDT boundary is predicted correctly, which is of particular importance for risk assessments.

4.1.3 $C_2H_4/O_2/N_2$ Mixtures

This section deals with the validation of the developed solver framework and combustion modelling for stoichiometric $C_2H_4/O_2/N_2$ mixtures, being one of the most important representatives of hydrocarbons used in chemical and process engineering. The numerical setup follows Sec. 4.1.1. Experimental validation data is taken from Schildberg [116]. For the stoichiometric $C_2H_4/O_2/N_2$ mixtures, the air is enriched with oxygen. A summary of the initial conditions and geometrical dimensions is given in Tab. 4.2. The initial temperature is set to 293 K. Again, two different pipe geometries are considered. No experimental flame-tip data is available and therefore validation is limited to the prediction of the DDT location within the confidence interval of +/- 25 % of the experimental DDT location.

Table 4.2: Smooth pipe experimental conditions for C_2H_4 mixtures, taken from Schildberg [116].

Case	$X_{C_2H_4}$	Initial pressure	Pipe diameter	Pipe length	DDT Exp.	DDT Sim.
E10	0.0733	8.00 bar	48.3 x 2.6 mm	9.48 m	3.24 m	3.59 m
E11	0.0833	8.00 bar	48.3 x 2.6 mm	9.48 m	2.39 m	2.51 m
E12	0.933	8.00 bar	48.3 x 2.6 mm	9.48 m	1.68 m	1.88 m
E13	0.1033	10.00 bar	48.3 x 2.6 mm	9.48 m	1.55 m	1.25 m
E14	0.1166	10.00 bar	48.3 x 2.6 mm	9.48 m	1.08 m	1.01 m
E29	0.10	2.66 bar	114.3 x 3.6 mm	9.603 m	4.10 m	3.27 m
E31	0.1166	3.00 bar	114.3 x 3.6 mm	9.603 m	2.39 m	2.74 m
E32	0.10	3.50 bar	114.3 x 3.6 mm	9.603 m	3.60 m	3.44 m

The cases will be analysed in order of increasing fuel content, starting with case E10 in Fig. 4.10. As expected, the change in mixture did not alter the qualitative acceleration behaviour. This was also reported by Kuznetsov [87] who investigated flame acceleration and DDT of stoichiometric H_2/O_2 and C_2H_4/O_2 mixtures in smooth pipes experimentally. A closer look at the x-t diagram (left) and the v-x diagram (right) of Case E10 reveals smoother traces compared to the $H_2/O_2/N_2$ mixtures. Since the general reactivity of C_2H_4 is lower and the air is only sightly enriched with oxygen in case E10 ($X_{C_2H_4}$=0.0733), acceleration and DDT take place more gradually. Therefore,

the characteristic kink in the x-t diagram is less pronounced. τ_{trans} occurs at 12.79 ms.

Furthermore, the computed DDT at 3.59 m matches the experimental confidence interval around the DDT at 3.24 m but is now located after the measured value. Considering the dependency of the t_{ign} on pressure and temperature for C_2H_4 (Fig. 3.13), there is a more gradual decrease compared to H_2. Especially the strong reduction for a pressure level of 10 bar, which is mainly responsible for the early activation of the detonation source term in the H_2 cases, does not appear. As a consequence, computed DDT locations scatter around the experimental values.

Regarding the v-x diagram on the right, DDT is observed after v exceeds a_{pr} and reaches the sonic flame regime. The detonation overshoots D_{CJ} and relaxes to a value above the stable propagation velocity from 1-D theory. In principle, this resembles an overderiven detonation, as observed experimentally, i.e. for case H2 (Fig. 4.6). However, this phenomenon could not be reproduced

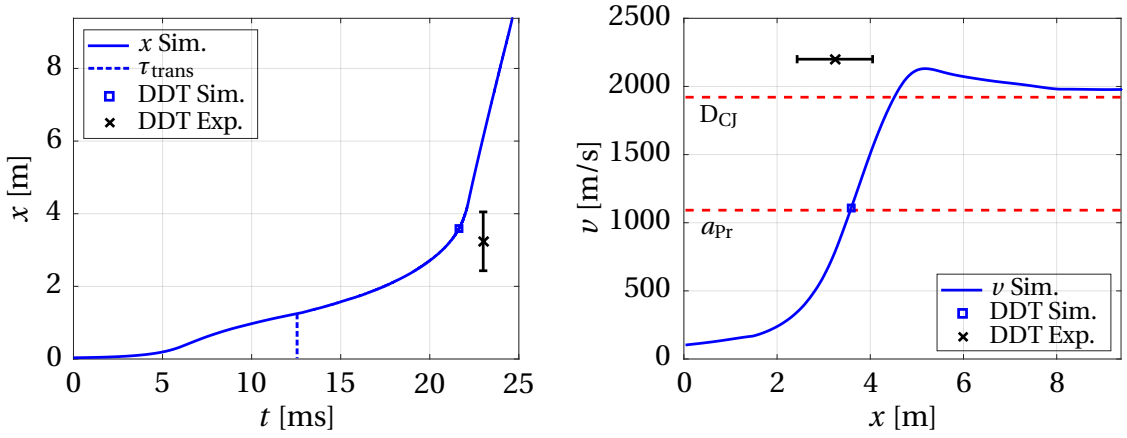

Figure 4.10: Flame-tip position x (left) and flame-tip velocity v (right) of case E10. DDT location indicated by black cross with confidence interval (experiment) and blue square (simulation). D_{CJ} and a_{pr} indicated by red dashed lines. τ_{trans} (blue dashed line) at 12.79 ms.

for the $H_2/O_2/N_2$ mixtures and is therefore not expected to be predicted for the $C_2H_4/O_2/N_2$ mixtures as the numerical setup is identical. An explanation is given by the OpenFOAM [141] thermo libraries which tend to overestimate

the heat relase for oxygen enriched air as their development in old OpenFOAM versions (2.1.x) mainly focused on applications with standard air. Thus, the implementation of the thermo libraries is based on the O_2:N_2 ratio of air. As a consequence, the burnt material properties like $c_{p,\mathrm{b}}$ or a_b are computed with a certain error. This results in the overestimation of the heat release for the oxygen enriched conditions. The extent to which the heat release is overpredicted seems to be roughly proportional to the reactivity of the mixture, as is evident from the following cases. This phenomenon also becomes apparent in the pressure data of the 20 l sphere in Sec. 4.2.3. Nevertheless, the global flame and detonation propagation is physically reasonable.

Regarding the results of case E11 in Fig. 4.11, flame acceleration is identical, while the kink in the x-t diagram (left) is more significant than for case E10 due to the increased reactivity ($X_{\mathrm{C_2H_4}}$=0.0833). τ_trans appears at 13.41 ms. The computed DDT is located in the sonic flame regime at 2.51 m, occurring downstream of the experimental value at 2.39 m. A considerable intial delay exists in the the x-t data. This is related to the ignition modelling deficits and seems to have a stronger impact for more complex fuels. For these fuels, the tabulated chemistry is not able to fully capture all chemical processes and reaction paths associated to the ignition and the expansion of the flame front as the tabulation is solely carried out at specific points. Intermediate states are linearly interpolated in the solver. If a non-linear behaviour of certain quantities occurs between the tabulated values, this cannot be reproduced by the simulations. A detailed examination, however, would require additional experimental flame-tip data.

The trace of v is again similar to former cases. After a strong acceleration due to auto-ignition effects, v peaks at a value above D_CJ and relaxes in the following while propagating along the pipe due to numerical diffusion and the smaller preconditioning on the under-resolved grids.

Flame acceleration and DDT of case E12 ($X_{\mathrm{C_2H_4}}$=0.0933) are analysed in more detail in the following, starting with x-t data (left) and v-x data (right) in Fig. 4.12. τ_trans takes place at 7.92 ms. Again, the overall propagation behaviour is similar to the other cases, including continuous deflagrative flame acceleration, the characteristic kink and detonation propagation at a constant speed.

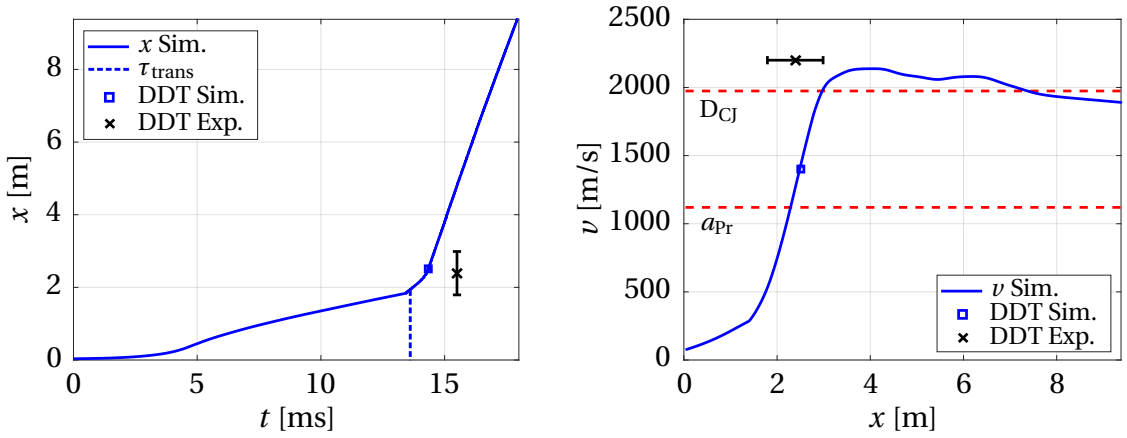

Figure 4.11: Flame-tip position x (left) and flame-tip velocity v (right) of case E11. DDT location indicated by black cross with confidence interval (experiment) and blue square (simulation). D_{CJ} and a_{pr} indicated by red dashed lines. τ_{trans} (blue dashed line) at 13.41 ms.

The computed DDT at 1.88 m is predicted within the confidence interval of the experimental DDT at 1.68 m.

Regarding the v-x diagram, DDT occurs at a velocity above a_{pr}, as expected. Moreover, the detonation velocity exceeds D_{CJ} due to the overpredicted heat release and propagates along the pipe axis at a velocity larger than D_{CJ}.

Similar to case H2 (Fig. 4.6), the global flame propagation behaviour is examined by the evolution of the flame shape, using the c field. Fig. 4.13 illustrates the flame front on a vertical plane along the horizontal pipe axis. Only half of the pipe height is shown, where the wall is located at the bottom of the individual plots in time. The same distinct stages as for case H2 are identified, also reported by Kuznetsov [87]:

- First, flame dynamics are dominated by the expansion and instability-based flame wrinkling, where the impact of instabilities is small due to the stoichiometric mixtures.
- A finger-tip shaped flame front develops at 2 ms and 3 ms after the spherical expansion due to the no-slip boundary condition.
- When the flame front reaches the boundary layer, where most of the tur-

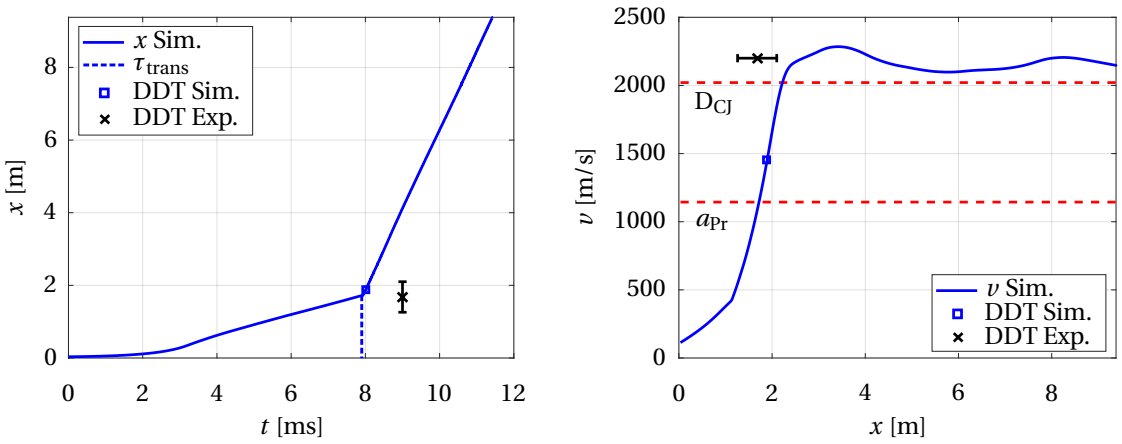

Figure 4.12: Flame-tip position x (left) and flame-tip velocity v (right) of case E12. DDT location indicated by black cross with confidence interval (experiment) and blue square (simulation). D_{CJ} and a_{pr} indicated by red dashed lines. τ_{trans} at 7.92 ms.

bulence is produced in the early stage, S_{eff} increases here due to turbulent flame wrinkling. This results in the formation of a tulip-shaped flame front at 5 ms.

However, the tulip-shaped flame is less pronounced as for H_2 due to the stronger smearing of the c field, associated to the lower reactivity of C_2H_4.

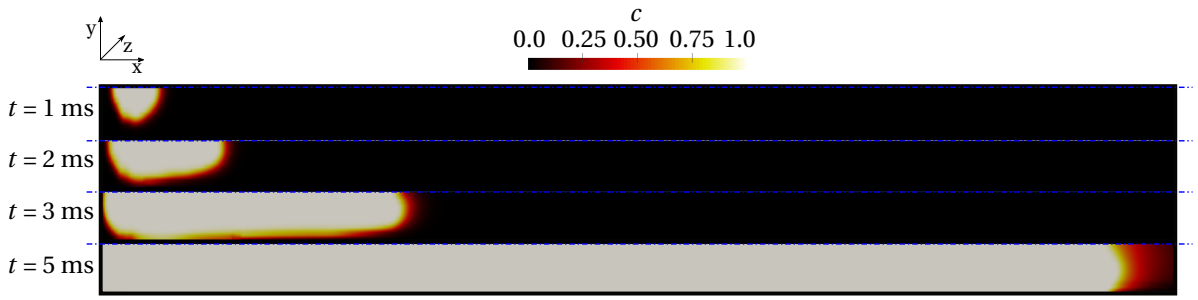

Figure 4.13: Flame propagation of case E12 between 1 ms and 5 ms on a vertical plane along the horizontal pipe axis, illustrated by the c field. Only half of the pipe height is shown. Pipe middle axis at the top of the pictures of the individual plots in time.

The pressure distributions of case E12 at multiple sensor locations along the pipe wall are compared with the experimental data from Schildberg [116] in

Fig. 4.14. Similar to the H_2 simulations, the other C_2H_4 cases exhibit a similar pressure/distance/time behaviour and therefore this comparison is considered representative for all investigated C_2H_4 cases. Simulation data is shifted in time to match the experimental DDT location. Thus, the delay associated with the ignition is eliminated.

In general, a good qualitative agreement for the simulated pressure data is achieved. Regarding the sensor locations between 0.31 m and 1.57 m, the experimenal peak cannot be reproduced due to the dissipative nature of the pressure-based solver and the deficits with respect to the ignition modelling. From the sensor location at 2.2 m on, a strong pressure peak is present in the simulation data as a result of the switch to the explicit density-based solver and the previous DDT. Following on from the DDT, the propagation velocities of the detonation and back-running pressure waves from the pipe end agree well for simulation and experiment. During the propagation along the pipe, the detonative pressure peak varies in both, experiment and simulation due to the relaxation and the interaction with transverse pressure waves.

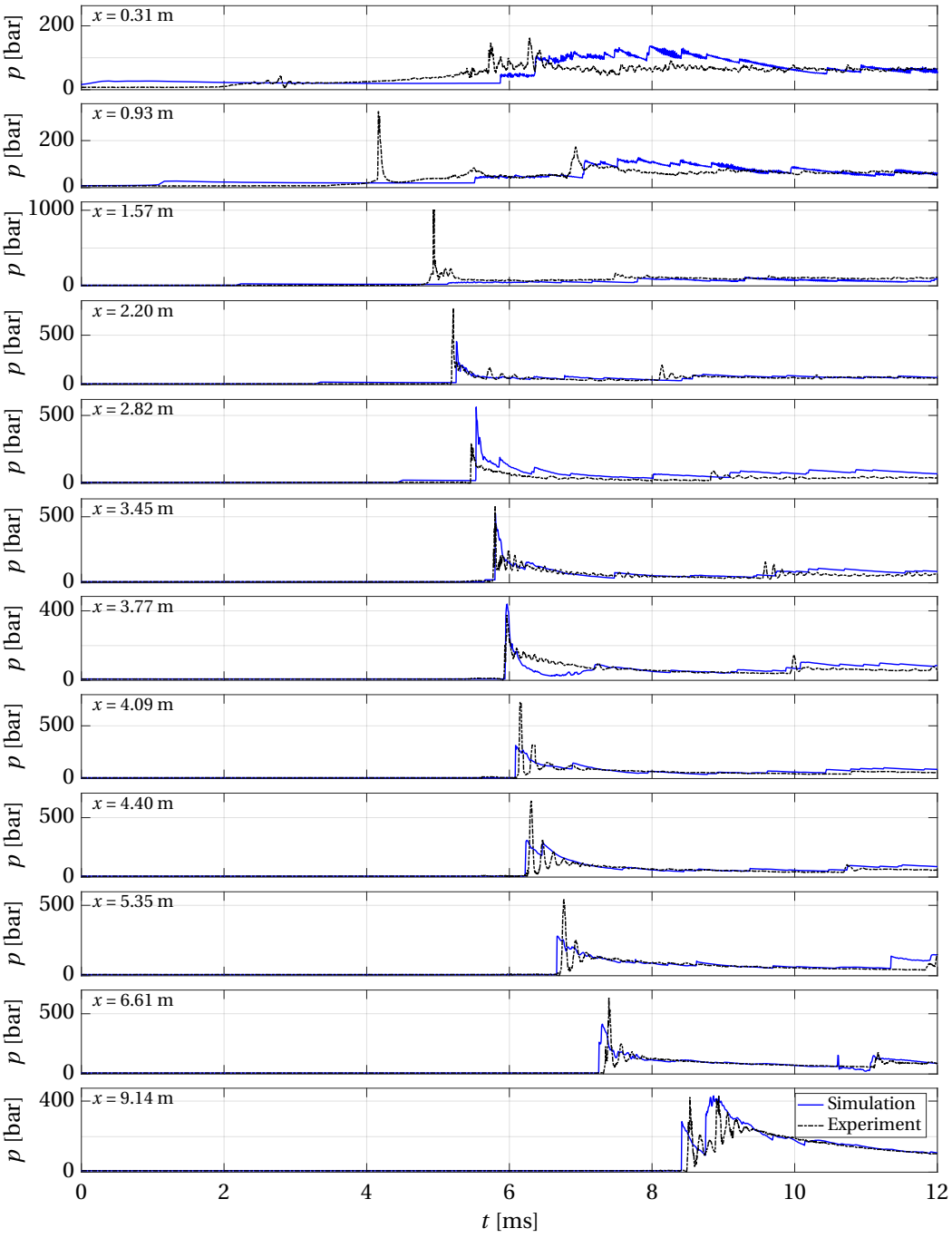

Figure 4.14: Comparison of experimental pressure data of case E12 (black dashed line) and simulation pressure (blue line) at experimental pressure sensor locations. Simulation data is shifted in time to match the pressure peak to the experimental DDT location (1.68 m).

To conclude the validation for the small pipe, two cases with a further increased fuel content (Case E13: $X_{C_2H_4}$=0.1033, Case E14: $X_{C_2H_4}$=0.1166) and an initial pressure of 10 bar are investigated. The results for x-t (left) and v-x (right) of case E13 in Fig. 4.15 show a similar flame propagation behaviour. Due to the enhanced reactivity and the intensified flame acceleration, τ_{trans} is shifted to earlier points in time and appears at 4.71 ms. Moreover, the computed DDT at 1.25 m matches the confidence interval of the experimental DDT at 1.55 m, being located at the lower end.

Regarding the v-x diagram, the strong acceleration for this highly reactive mixture is apparent from the beginning on. The DDT takes place after exceeding a_{pr} and the velocity peaks above D_{CJ} as a consequence of the overpredicted heat release. Consequently, the detonation propagates along the pipe at a velocity larger than D_{CJ}.

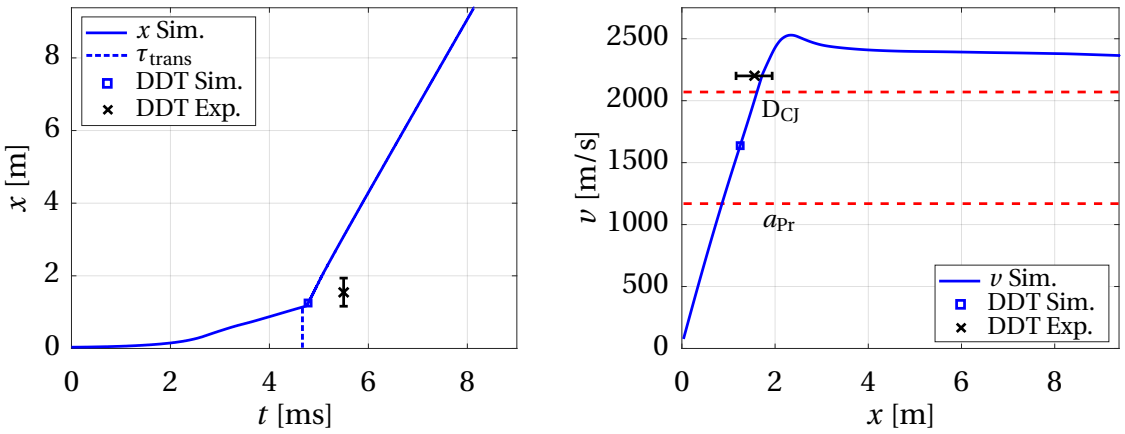

Figure 4.15: Flame-tip position x (left) and flame-tip velocity v (right) of case E13. DDT location indicated by black cross with confidence interval (experiment) and blue square (simulation). D_{CJ} and a_{pr} indicated by red dashed lines. τ_{trans} (blue dashed line) at 4.71 ms.

Case E14 depicts the highest reactivity for the small pipe cases and therefore τ_{trans} occurs at 3.31 ms in Fig. 4.16. The experimental DDT is located at 1.08 m which can successfully be predicted by the solver where the DDT is located at 1.01 m. Otherwise, the results for x-t (left) and v-x (right) are again similar to the other cases. The solver setup as well as the combustion modelling have therefore proven to be capable of predicting the global flame propagation for

stoichiometric C_2H_4/O_2 mixtures in the small pipe.

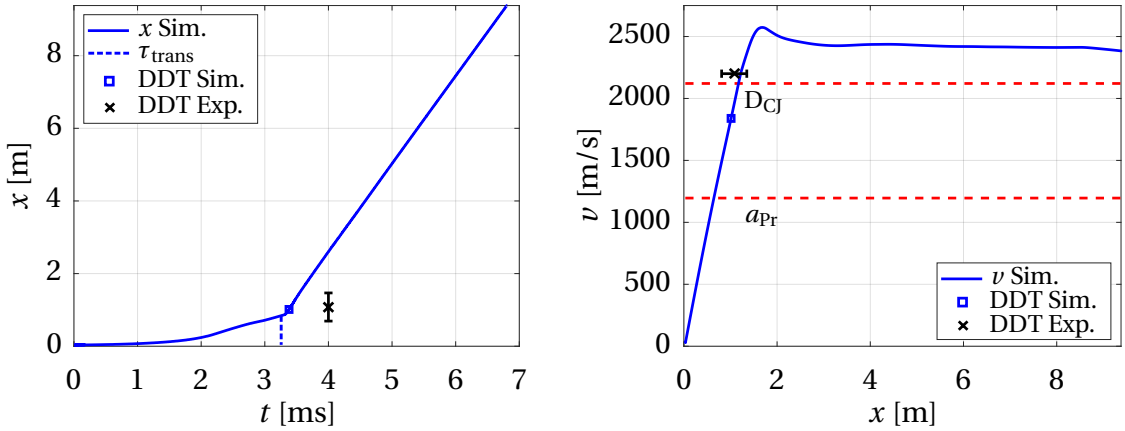

Figure 4.16: Flame-tip position x (left) and flame-tip velocity v (right) of case E14. DDT location indicated by black cross with confidence interval (experiment) and blue square (simulation). D_{CJ} and a_{pr} indicated by red dashed lines. τ_{trans} (blue dashed line) at 3.31 ms.

The validation for stoichiometric $C_2H_4/O_2/N_2$ mixtures in smooth pipes is concluded by three cases in a larger pipe (Tab. 4.2). Similar to the cases H26 and H27, the experimental DDT location is shifted downstream as the run-up distance is in general assumed to be roughly proportional to the inner pipe diameter for equal initial conditions (p, T). In addition, the lower initial pressure decreases turbulent flame wrinkling and delays auto-ignition effects. However, the computed traces exhibit the same flame acceleration behaviour.

Hence, x-t data of case E29 ($X_{C_2H_4}$=0.10) in Fig. 4.17 (left) is characterised by a gradually increasing gradient. Significant auto-ignition effects are indicated by the kink in the x-t diagram where a shift to the linear dependence on time is observed in the detonative regime. τ_{trans} appears at 11.37 ms and the computed DDT at 3.27 m agrees well with the confidence interval of the experimental DDT location at 4.10 m.

Regarding the v-x data in Fig. 4.17 (right), DDT is again located in the sonic flame regime. Moreover, the exceeding of D_{CJ} and the elevated detonation velocity are apparent as expected from the overpredicted heat release.

Further increasing the fuel content at roughly the same initial pressure in case

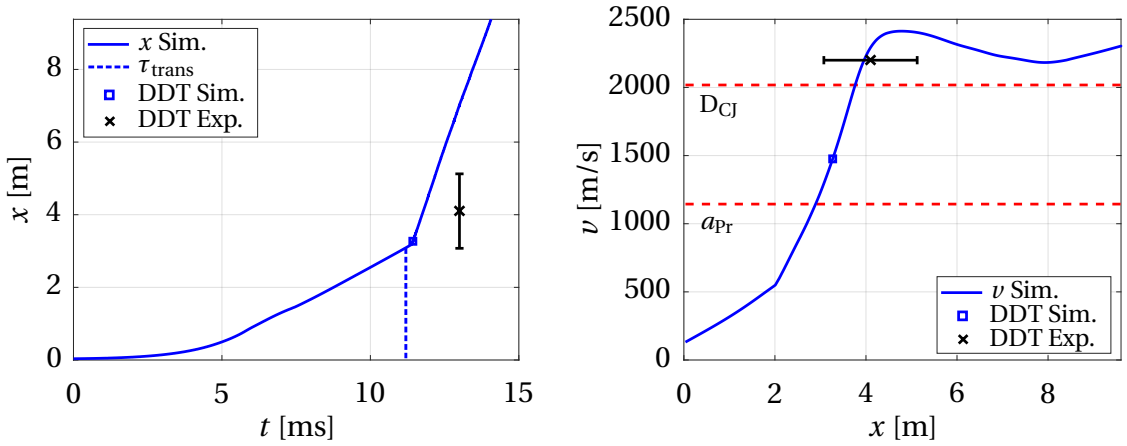

Figure 4.17: Flame-tip position x (left) and flame-tip velocity v (right) of case E29. DDT location indicated by black cross with confidence interval (experiment) and blue square (simulation). D_{CJ} and a_{pr} indicated by red dashed lines. τ_{trans} (blue dashed line) at 11.37 ms.

E31 ($X_{C_2H_4}$=0.1166) intensifies flame acceleration and shifts the location of DDT upstream, as depicted in Fig. 4.18. τ_{trans} takes place at 7.85 ms. The experimental DDT location at 2.39 m is successfully predicted by the simulation where DDT is observed at 2.74 m, being in the sonic flame regime.

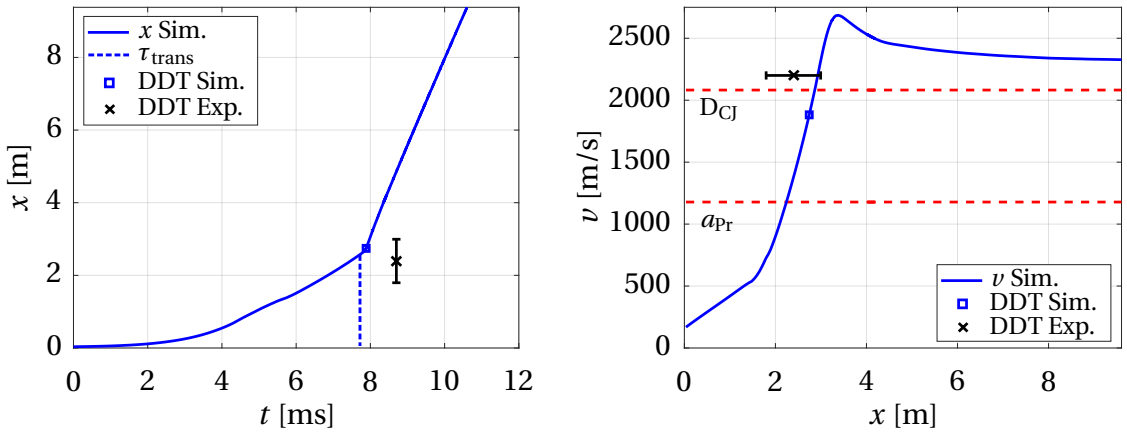

Figure 4.18: Flame-tip position x (left) and flame-tip velocity v (right) of case E31. DDT location indicated by black cross with confidence interval (experiment) and blue square (simulation). D_{CJ} and a_{pr} indicated by red dashed lines. τ_{trans} (blue dashed line) at 7.85 ms.

Finally, the results for x-t (left) and v-x (right) of case E32 are analysed in Fig. 4.19. In comparison to case E29 (Fig. 4.17), the C_2H_4 content ($X_{C_2H_4}$=0.10) is equal but the initial pressure is increased. This enhances flame wrinkling (cf. Eq. 3.89) and therefore flame acceleration, shifting the location of DDT upstream. τ_{trans} appears at 11.39 ms. Excellent agreement between the computed DDT at 3.44 m and the measured value at 3.60 m is achieved. The simulated results for x and v are qualitatively similar to all configurations investigated for the stoichiometric $C_2H_4/O_2/N_2$ mixtures, including continuous deflagrative flame acceleration and detonation propagation at a constant speed.

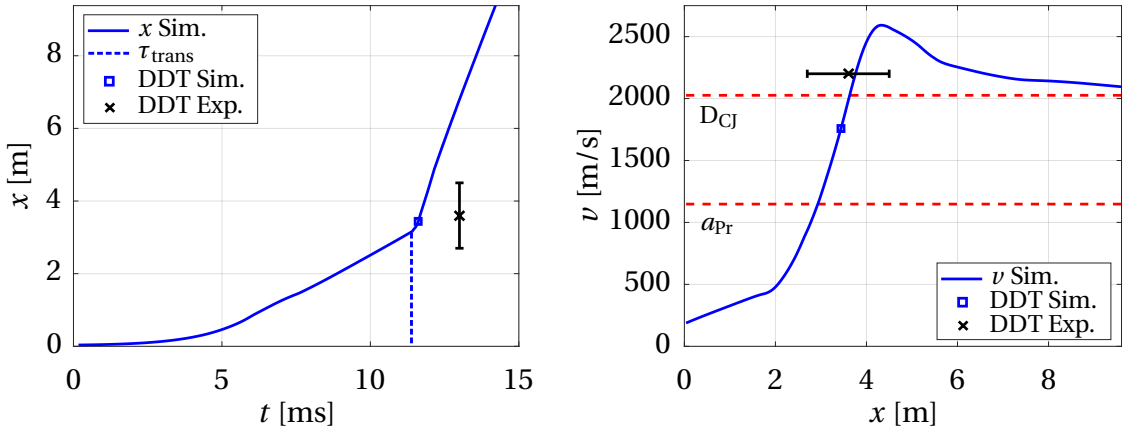

Figure 4.19: Flame-tip position x (left) and flame-tip velocity v (right) of case E32. DDT location indicated by black cross with confidence interval (experiment) and blue square (simulation). D_{CJ} and a_{pr} indicated by red dashed lines. τ_{trans} (blue dashed line) at 11.39 ms.

In summary, the presented results have proven the capability of the developed pressure-/density-based CFD DDT solver to efficiently predict DDT locations of stoichiometric $H_2/O_2/N_2$ and $C_2H_4/O_2/N_2$ mixtures in smooth pipes for different pipe dimensions and initial conditions. More precisely, the DDT location could be predicted within the defined confidence interval of +/- 25 % of the experimental value. Solely the DDT at the pipe end in case H27 could not be reproduced. However, this case does not represent a typical accident scenario. Regarding stoichiometric $H_2/O_2/N_2$ mixtures, DDT is generally observed towards the lower end of the confidence interval due to the strong decrease of the t_{ign} with pressure. Regarding the design process of chemi-

cal plants, this tendency can be interpreted as a conservative prediction of potential DDT locations. In terms of stoichiometric $C_2H_4/O_2/N_2$ mixtures, the dependency of t_{ign} on pressure is not as critical and therefore the computed DDT positions scatter around the measured values. Since the OpenFOAM [141] thermo libraries are mainly developed and validated for standard fuel/air mixtures in the used old version (2.1.x), the implementation is based on the O_2:N_2 ratio of air. As a consequence, the burnt material properties like $c_{p,\mathrm{b}}$ or a_{b} are computed with a certain error which results in the overestimation of the heat release for the oxygen enriched conditions. Moreover, the delay associated with the ignition modelling deficits is larger for the stoichiometric $C_2H_4/O_2/N_2$ mixtures as the tabulated chemistry is not able to fully capture the chemical processes and possible reaction paths for more complex fuels. This concerns in particular C_2H_4 burnt in N_2 diluted air with low reactivity. For these mixtures, critical flame acceleration was not reached and no DDT could be computed.

Characteristic features of accelerating flames in smooth pipes are reproduced within the under-resolved framework in accordance with the experimental findings of other authors [83] [87]. Four distinct stages were identified:

- Initially, flame dynamics are dominated by the expansion of the flame front and instability-based flame wrinkling as well as flame stretch effects.
- With the creation of a boundary layer, where most of the turbulence is produced in the early stage, flame acceleration increases and turbulent flame wrinkling becomes dominant. Due to increasing flame and flow velocities, turbulence production is also enhanced in the bulk flow as a result of gas dynamic effects and the related creation of shear layers.
- As critical conditions for the onset of detonation are satisfied, significant auto-ignition effects start to take place, marked by the characteristic kink in the x-t data.
- There exists a linear dependence of flame-tip position on time for detonation propagation. This indicates a constant speed, being characteristic for stable detonations.

In terms of computing pressure, the under-resolved framework is not able to reproduce the maximum value of the pressure peaks due to the smearing of pressure waves and shocks on the coarse grids as well as the dissipative nature of the pressure-based solver. Nevertheless, there is a good qualitative and quantitative agreement for the remaining parts of the pressure distributions. Additionally, the propagation velocities of the detonation and back-running pressure waves are predicted well.

4.2 20 l Sphere

In order to validate the developed solver for different smooth geometries, the results for flame acceleration and DDT in a 20 l sphere will be presented in this section. Hence, 3-D flame propagation is considered, in comparison to quasi 1-D flame dynamics in the smooth pipe cases. Validation is carried out by means of the pressure distribution where simulated pressure data is shifted in time to match the experimental peak level. The focus is therefore on identifying mixtures and conditions, being critical for the onset of a detonation. $H_2/O_2/N_2$ and stoichiometric $C_2H_4/O_2/N_2$ mixtures are investigated.

4.2.1 Numerical Setup

Fig. 4.20 shows the computational domain for the 20 l sphere simulations. The diameter of the sphere is 340 mm. Only an eighth of the sphere is computed in order to reduce the computational costs. Thus, symmetry boundary conditions are applied, allowing for the simulations to be run on standard Linux workstations with 64 cores. The initial grid size is set to 2.0 mm.

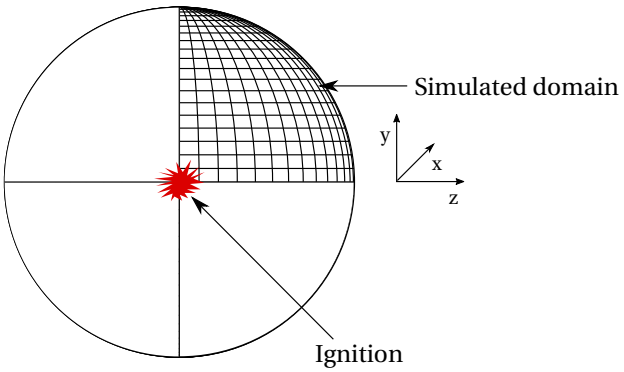

Figure 4.20: CFD grid of 20 l sphere. Only marked eighth is simulated.

No AMR is applied to the surface region of the sphere as turbulence is mainly produced in shear layers in front of the reaction zone. The expansion of the reaction products and the increase of the flame surface with increasing flame radius have a strong impact on flame dynamics, too. Ignition of the mixture

is realised by setting its state to burnt within a spherical volume in the centre of the sphere during the first time step. The remaining numerical settings are similar to the smooth pipe cases, depicted in Sec. 4.1.1.

4.2.2 $H_2/O_2/N_2$ Mixtures

No measurement data from BASF exists for H_2O_2/N_2 mixtures in a 20 l sphere. Moreover, there is only little data in the literature which is associated to the dangers of H_2 flame acceleration and DDT. Hence, mostly lean mixtures with a small acceleration potential are investigated, being not of interest for the current work. However, Jo [72] analysed the pressure data from the combustion of a rich H_2/air mixture with 31.7 Vol.-% H_2 at 1 bar initial pressure and an initial temperature of 293 K, which is used for validating the solver setup and combustion modelling for H_2.

Fig. 4.21 highlights the pressure for the investigated H_2/air mixture where the pressure probe is located centrally at the top of the sphere. τ_{trans} takes place at 11.86 ms. After a stage of slowly increasing pressure, the experimental pressure data rises and exceeds the adiabatic isochoric explosion pressure p_{AICC}. Afterwards, the pressure level relaxes to a value below p_{AICC} due to heat losses at the wall. As expected from the under-resolved framework and the pressure data in smooth pipes (Fig. 4.7, Fig. 4.14), the simulative peak pressure is somewhat lower than the measured value. Nevertheless, there is an excellent qualitative and quantitative agreement for the remaining parts. No DDT is observed in both, simulation and experiment, which is indicated by the small pressure oscillations and the lack of a strong pressure peak, being significantly larger than p_{AICC}. Therefore, this mixture is not considered critical in terms of flame acceleration and DDT which is attributed to the atmospheric initial conditions and the usage of standard air.

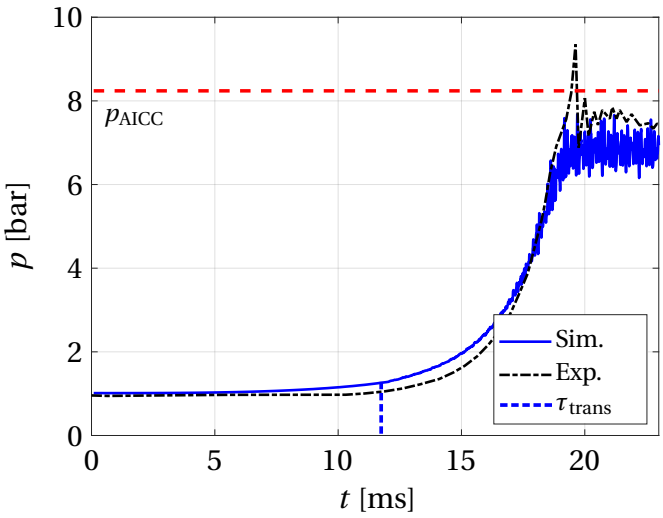

Figure 4.21: Comparison of simulation pressure data (blue line) with experimental results from Jo [72] (black dashed line) for a H_2/air mixture with 31.7 Vol.-% H_2 at 1 bar and 293 K. τ_{trans} (blue dashed line) at 11.86 ms. Adiabatic, isochoric explosion pressure (p_{AICC}) indicated by red dashed line.

4.2.3 $C_2H_4/O_2/N_2$ Mixtures

Stoichiometric $C_2H_4/O_2/N_2$ mixtures have been analysed experimentally at BASF at an initial pressure of 5 bar and an initial temperature of 293 K as well as 473 K in order to identify the lower detonation boundary. The results for an initial temperature of 293 K are depicted in Fig. 4.22 for a fuel content of 9.33 Vol.-% C_2H_4 (left) and 10.0 Vol.-% C_2H_4 (right). τ_{trans} appears at 8.11 ms and 6.96 ms, respectively.

The occurrence of DDT can be identified between the two fuel contents in Fig. 4.22. Regarding the case with 9.33 Vol.-% C_2H_4 on the left, no DDT takes place which is indicated by the small pressure oscillations and the lack of a strong peak exceeding p_{AICC}. The experimental maximum pressure agrees well with p_{AICC} while the simulative pressure level is higher. This is explained by the overpredicted heat release for oxygen enriched air (see pipe case E10 for more detailed explanation). Apart from that, the computed pressure data matches

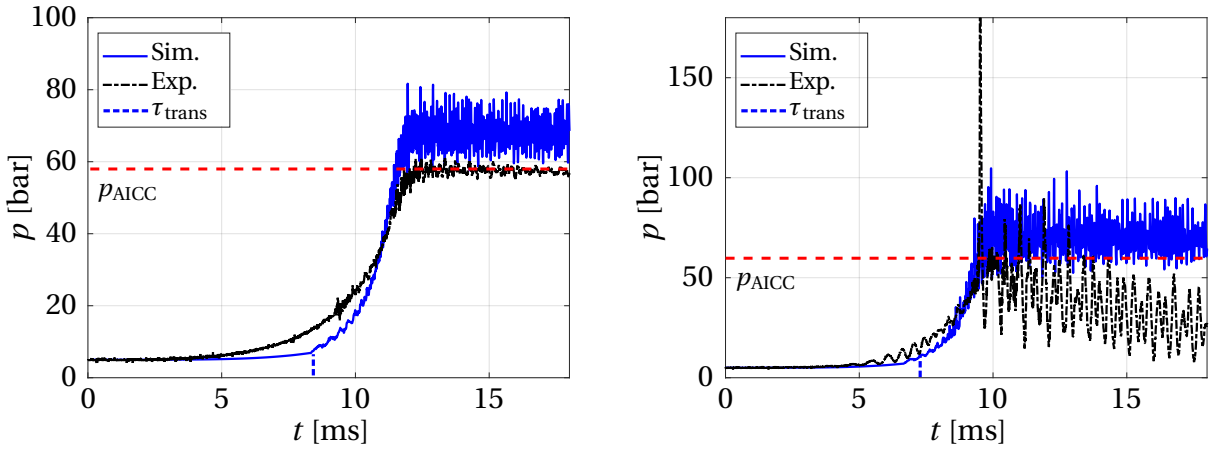

Figure 4.22: Comparison of pressure data for two stoichiometric $C_2H_4/O_2/N_2$ mixtures with 9.33 Vol.-% C_2H_4 (left) and 10.0 Vol.-% C_2H_4 (right) at 5 bar and 293 K. τ_{trans} (blue dashed line) at 8.11 ms and 6.96 ms, respectively. Simulation data coloured blue and experimental results coloured black. Adiabatic, isochoric explosion pressure (p_{AICC}) indicated by red dashed line.

the measurements well.

The presence of DDT is deduced from the pressure distribution of the case with 10.0 Vol.-% C_2H_4 in Fig. 4.22 (right). Both, in the experiment and the simulation, a strong pressure peak at $t \approx 10$ ms and the subsequent large pressure oscillations imply the occurrence of DDT. Generally, good agreement with the experimental data is achieved. The decrease of the experimental pressure level results from a thermo shock of the sensor. The averaged simulative pressure level is again larger than the measured value, being close to p_{AICC}.

Finally, the two previously introduced stoichiometric $C_2H_4/O_2/N_2$ mixtures are investigated at an initial temperature of 473 K in Fig. 4.23. The behaviour is similar to Fig. 4.22. No DDT is observed for the mixture with 9.33 Vol.-% C_2H_4 (left) while DDT takes place at $t \approx 8$ ms for the mixture with 10.0 Vol.-% C_2H_4 (right). This is indicated by the strong pressure peak and the associated oscillations afterwards. τ_{trans} is shifted to earlier points in time due to the increased temperature (reactivity) and appears at 5.12 ms and 4.85 ms, respectively. In accordance with the former results, the averaged pressure level in

the simulation is larger due to the overpredicted heat release (see pipe case E10 for more detailed explanation). The difference between simulation and experiment is smaller due to the high combustion temperatures and the corresponding small density, which dampens the simulation pressure level via the ideal gas law. Apart from that, the results match excellently and the DDT boundary could be predicted correctly.

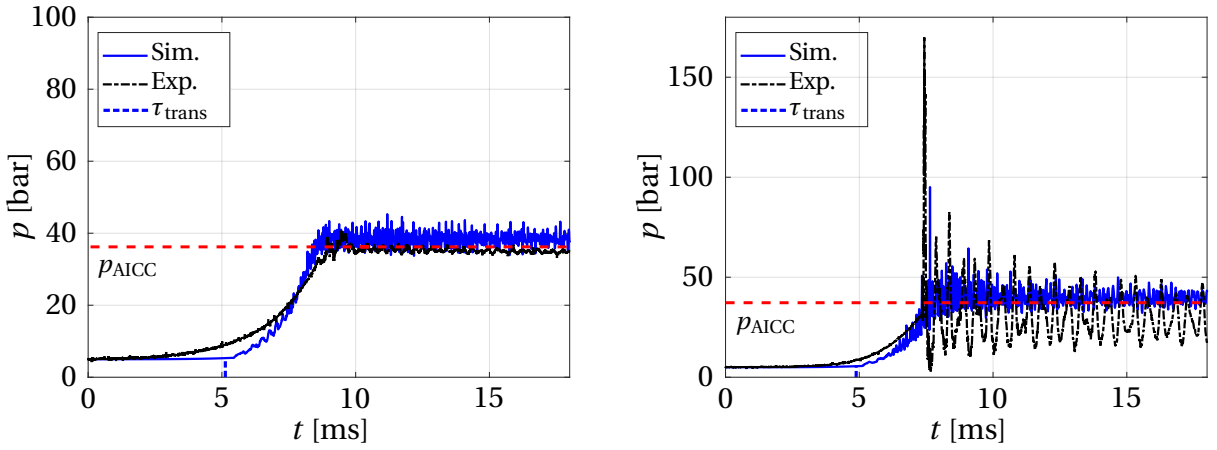

Figure 4.23: Comparison of pressure data for two stoichiometric $C_2H_4/O_2/N_2$ mixtures with 9.33 Vol.-% C_2H_4 (left) and 10.0 Vol.-% C_2H_4 (right) at 5 bar and 473 K. τ_{trans} (blue dashed line) at 5.12 ms and 4.85 ms, respectively. Simulation data coloured blue and experimental results coloured black. Adiabatic, isochoric explosion pressure (p_{AICC}) indicated by red dashed line.

Summarising the presented results for flame acceleration and DDT in a 20 l sphere, the solver's capability to account for symmetrical flame propagation in the sphere is proven by means of the pressure distributions. Regarding H_2 mixtures, validation was limited to the experimental data for a purely deflagrative case at atmospheric conditions from Jo [72], where good agreement is achieved. As expected from the under-resolved framework, the maximum simulation pressure level is lower than the experimental value and p_{AICC}.

In terms of stoichiometric $C_2H_4/O_2/N_2$ mixtures, validation of the solver setup was carried out for two mixtures at an initial pressure of 5 bar and 293 K as well as 473 K initial temperature. The transition from a deflagrative explosion for a mixture with 9.33 Vol.-% C_2H_4 to the occurrence of DDT for a mixture

with 10.0 Vol.-% C_2H_4 could successfully be reproduced. From the point of risk assessment and plant design, the prediction whether DDT takes place - by identifying critical mixtures and conditions - is the most important aspect. The larger pressure level in the simulation due to the overpredicted heat release for oxygen enriched air (see pipe case E10 for more detailed explanation) can be interpreted as a conservative prediction of potential pressure loads. In conclusion, the developed CFD solver has proven to be an efficient tool for the simulation of flame acceleration, DDT and detonation propagation in typical smooth geometries of chemical plants: pipes and spherical vessels.

5 Summary and Outlook

5.1 Summary

Risk assessment is a crucial aspect in chemical and process engineering due to the usage of highly sensitive gaseous combustible mixtures at various process conditions. As effective ignition sources cannot be excluded in case of an accident, a comprehensive analysis, covering a broad range of potential accident scenarios, is of particular importance. In that context, the elaboration of critical conditions for the hazardous DDT to take place is of major interest. The current state of knowledge in the CFD DDT solver development focuses predominantly on obstacle-laden geometries and lean mixtures due to the research being mainly driven by nuclear reactor safety. Hence, application of these solvers to process engineering problems where smooth geometries and stoichiometric fuel/oxidizer/diluent mixtures are of interest is limited.

The CFD DDT solver developed in this work is able to close this gap and is therefore capable of simulating flame acceleration, DDT and detonation propagation in smooth geometries after a weak ignition. More precisely, the intention is to correctly predict the global flame propagation behaviour and the DDT location. For that purpose, an efficient hybrid pressure-/density-based solver architecture was implemented within the OpenFOAM framework. This allows for the incompressible regime of slow to medium fast flames as well as the compressible fast flame regime and detonation propagation to be captured. Combustion is considered by a reaction progress variable approach. The modelling in this work refers to the closure of the source term by the maximum taken from a deflagration and a detonation source term. The deflagration source term is based on the concept of turbulent flame speed closure (TFC), applying the model from Katzy for H_2 mixtures and the correlation of Muppala for C_2H_4 mixtures. The temporal evolution of flame wrinkling dur-

ing this highly unsteady process is incorporated by the flame wrinkling transport equation from Weller. Modelling of the detonation source term resembles the ZND theory (Sec. 2.4), including a two stage formulation: an initial phase of ignition delay, followed by an exothermic heat release. Activation of the detonation source term is controlled by a dimensionless induction parameter which compares the simulation time with tabulated ignition delay times, derived from Cantera calculations. This parameter is also incorporated into a transport equation to allow for considering the temporal evolution of pressure and temperature fields as well as the exchange of radicals.

Validation of the solver is carried out for stoichiometric $H_2/O_2/N_2$ and $C_2H_4/O_2/N_2$ mixtures by means of experimental DDT locations in smooth pipes and pressure traces in a 20 l sphere. Hence, two different types of flame propagation could be examined: quasi 1-D propagation in the smooth pipes and 3-D propagation in the 20 l sphere. For smooth pipes, the target of a successful prediction of the DDT location is set to lie within a confidence interval of +/- 25 % of the experimental DDT location. Regarding the 20 l sphere, the investigations focus on identifying critical mixtures and conditions for the onset of DDT.

With respect to the smooth pipe cases, the DDT location could be computed within the confidence interval of the experimental DDT for a variety of pipe geometries, fuel mixtures and initial conditions. The DDT originated from the immediate vicinity of the flame front in all cases. In addition, essential features of flame propagation in smooth pipes could be reproduced within the framework of under-resolved simulations: the formation of a finger-tip shaped flame, followed by a tulip-shaped flame front. Fuel mixtures and conditions, being critical for a DDT to occur in the 20 l sphere, could successfully be predicted by the solver at two initial temperature levels. The hypothesis that the macroscopic simulation of flame acceleration and DDT does not require capturing of all small-scale phenomena could thus be confirmed.

An intrinsic shortcoming of the under-resolved framework and the dissipative nature of the pressure-based solver is the smearing of pressure waves and shocks. Hence, the initial pressure built-up and the related peak pressures in smooth pipes are underpredicted. In contrast, gas dynamics including the

measured pressure peaks are reproduced well after the switchover to the explicit density-based solver, and there is also a good quantitative agreement of the simulated pressure in the pipes with the measurements. Moreover, the propagation velocity of the detonation complex is precisely predicted. The deviation of the simulated pressures from the experimental data for stoichiometric $C_2H_4/O_2/N_2$ mixtures in the 20 l sphere can be traced back to the overpredicted heat release due to the use of thermo libraries, which do not cover air enrichment with O_2. Apart from that, the computed pressure distributions agree well with the experimental results and the adiabatic isochoric explosion pressure for the 20 l sphere cases.

Due to the large number of different process conditions covered by the simulations carried out, it can be concluded that the solver developed in this work is a valuable tool for the simulation of explosion processes in smooth industrial-scale geometries. The usage of under-resolved grids and tabulated chemistry make the solver numerically efficient. Solely a few additional transport equations compared to an inert flow solver are implemented. In addition, the tabulated chemistry avoids the evaluation of numerically stiff source terms (e.g. Arrhenius approaches). Hence, the DDT solver is feasible for performing parameter studies in the context of risk assessment and to support the experimental work.

Considering the long-term goal of being able to simulate flame acceleration and DDT in complex geometries, the developed solver is a solid starting point. Open issues, which are of interest for the future solver development, are outlined in the next section.

5.2 Outlook

With regard to the future solver development, there are three aspects that should be addressed. The solver has so far solely been applied to simple smooth geometries. Thus, in the next step the simulation of more complex geometries should be considered, which are typical for process engineering equipment. Unfavourable grid angles, large aspect ratios and strongly differ-

ing cell volumes should be avoided around the obstacles [46]. The AMR can be modified to locally increase the resolution around the obstacles. Moreover, the solver should be able to deal with the intensified flame acceleration, resulting from obstacle-induced turbulence. Transition between the solution methods and DDT will therefore be shifted to earlier points in time. However, selection of the transition criterion has to be reevaluated in that context.

A second aspect involves the analysis of the thermo libraries with respect to the overpredicted heat release for oxygen enriched air. Since the release of OpenFOAM version 2.1.x [141], which was employed in the work reported in the current thesis, many updates and improvements have been implemented in the thermo libraries. The latest thermo libraries should be capable of dealing with varying oxygen concentrations in air. However, it is questionable whether a revision of solely the thermo libraries makes sense. The entire solver should rather be transferred to an up-to-date OpenFOAM version. In that context, the ignition modelling deficits could be addressed, too. A model for the ignition process can be created with updated thermo libraries, accounting for the temperature overshoot in the ignition volume exceeding the adiabatic flame temperature. This would allow for reproducing the initial expansion of the flame front and the experimental time scales more accurately. For validation purposes, experimental flame-tip position data of the early acceleration stage is required. Apart from that, highly-resolved simulations of the ignition can support the modelling.

Finally, extension of the combustion modelling towards multiple fuels is an aspect of high relevance for the chemical and processing industry. Due to the large variety of processes and involved mixtures, the solver should be able to cope with typical representatives like propene, acetylene or cyclohexane. Respective experimental data is available from Schildberg [114], [117], [118], [119] and Sperber [122]. For the simulation of complex fuels like cyclohexane, in particular, up-to-date thermo libraries are essential. However, the applicability of the tabulated chemistry in combination with the reaction progress variable approach on the under-resolved grids has to be reevaluated in that context. The rising complexity of ethylene chemistry already tends to increase the impact of the ignition modelling deficits. Furthermore, implementation

and validation of suitable burning laws for the calculation of the effective burning velocity is required.

Bibliography

[1] ACHASOV, O., AND PENYAZKOV, O. Dynamics study of detonation-wave cellular structure. 1. statistical properties of detonation wave front. *Shock Waves 11* (2002), 297–308.

[2] ANDERSON, J. *Modern compressible flow*. McGraw-Hill, 2004.

[3] ARNTZEN, B. *Modeling of turbulence and combustion for simulation of gas explosions in complex geometries*. PhD thesis, The Norwegian University of Science and Technology, 1998.

[4] AUNG, K., HASSAN, M., AND FAETH, G. Flame stretch interactions of laminar premixed hydrogen/air flames at normal temperature and pressure. *Combustion and Flame 109*, 1 (1997), 1–24.

[5] AUSTIN, J. *The role of instability in gaseous detonation*. PhD thesis, California Institute of Technology, 2003.

[6] BARALDI, D., HEITSCH, M., AND WILKENING, H. CFD simulations of hydrogen combustion in a simplified EPR containment with CFX and Reacflow. *Combustion Science and Technology 149*, 1-6 (1999), 361–387.

[7] BARITAUD, T., POINSOT, T., AND BAUM, M. *Direct numerical simulation for turbulent reacting flow*. Editions Technip, 1996.

[8] BARTLMÄ, F. *Gasdynamik der Verbrennung. Leitfäden der angewandten Mathematik und Mechanik*. Springer, 1975.

[9] BAUWENS, C., BERGTHORSON, J., AND DOROFEEV, S. Experimental study of spherical-flame acceleration mechanisms in large-scale propane air flames. *Proceedings of the Combustion Institute 35*, 2 (2015), 2059–2066.

[10] BAUWENS, C., BERGTHORSON, J., AND DOROFEEV, S. Experimental investigation of spherical-flame acceleration in lean hydrogen-air mixtures. *International Journal of Hydrogen Energy 42*, 11 (2017), 7691–7697.

[11] BEAUVAIS, R., MAYINGER, F., AND STRUBE, G. Turbulent flame acceleration - mechanisms and significance for safety considerations. *International Journal of Hydrogen Energy 19*, 8 (1994), 701–708.

[12] BECHTOLD, J., AND MATALON, M. The dependence of the markstein length on stoichiometry. *Combustion and Flame 127*, 1 (2001), 1906–1913.

[13] BLANCHARD, R., ARNDT, D., GRAETZ, R., POLI, M., AND SCHEIDER, S. Explosions in closed pipes containing baffels and 90 degree bends. *Journal of Loss Prevention in the Process Industries 23*, 2 (2010), 253–259.

[14] BORGHI, R. *On the structure and morphology of turbulent premixed flames*. Recent advances in the Aerospace Sciences, Plenum Press, 1985, pp. 117–138.

[15] BRADLEY, D., LAU, A., AND LAWES, M. Flame stretch rate as a determinant of turbulent burning velocity. *Philosophical Transactions: Physical Sciences and Engineering 338*, 1650 (1992), 359–387.

[16] BRAY, K., AND MOSS, J. Unified statistical model of the premixed turbulent flame. *Acta Astronautica 4*, 3 (1977), 291–319.

[17] BREHM, N. *Ein Beitrag zum Phänomen des Übergangs von der Deflagration in die Detonation*. PhD thesis, Technische Universität München, 1989.

[18] BREITUNG, W. Innovative Methoden zu Analyse und Kontrolle des Wasserstoffverhaltens bei Kernschmeldunfällen. Tech. rep., Forschungszentrum Karlsruhe, Institut für Kern- und Energietechnik, 2005.

[19] BUNDESANSTALT FÜR GEOWISSENSCHAFTEN UND ROHSTOFFE. Beirut explosion causes strong shock waves - infrasonic, hydroacoustic and seismic signals registered and investigated by BGR. Last accessed July 14, 2021. http://www.seismologie.bgr.de/sdac/erdbeben/big_quakes/beirut_200804_eng.html.

[20] BURKE, M., CHEN, Z., JU, Y., AND DRYER, F. Effect of cylindrical confinement on the determination of laminar flame speeds using outwardly propagating flames. *Combustion and Flame 156*, 4 (2009), 771–779.

[21] CHAPMAN, D. On the rate of explosions in gases. *The London, Edinburgh, and Dublin Philosophical Magazine and Journal of Science 47*, 284 (1899), 90–104.

[22] CHATRATHI, K., GOING, J., AND GRANDESTAFF, B. Flame propagation in industrial scale piping. *Combustion Science and Technology 20*, 4 (2001), 286–294.

[23] CHAUDHURI, S., WU, F., AND LAW, C. Scaling of turbulent flame speed for expanding flames with markstein diffusion considerations. *Physical Review E 88*, 3 (2013), 033005.

[24] CHEMICAL PARKS. List of chemical parks. Last accessed July 14, 2021. https://chemicalparks.com/chemical-parks/list-of-chemical-parks.

[25] CICCARELLI, G., AND DOROFEEV, S. Flame acceleration and transition do detonation in ducts. *Progress in Energy and Combustion Science 34*, 4 (2008), 499–550.

[26] CLANET, C., AND SEARBY, G. On the 'tulip flame' phenomenon. *Combustion and Flame 105*, 1 (1996), 225–238.

[27] CLAVIN, P. Dynamic behavior of premixed flame fronts in laminar and turbulent flows. *Progress in Energy and Combustion Science 11*, 1 (1985), 1–59.

[28] COLIN, O., DA CRUZ, A. P., AND JAY, S. Detailed chemistry-based auto-ignition model including low temperature phenomena applied to 3-D engine calculations. *Proceedings of the Combustion Institute 30*, 2 (2005), 2649–2656.

[29] DAMKÖHLER, G. Der Einfluss der Turbulenz auf die Flammengeschwindigkeit in Gasgemischen. *Zeitschrift für Elektrochemie und angewandte physikalische Chemie 46*, 11 (1940), 601–652.

[30] DAUDEY, N., AND CHAMPASITH, A. Accidental hydrogen release inside a nuclear power plant: CFD modelling and consequence analysis. *Tenth International Symposium on Hazards, Prevention, and Mitigation of Industrial Explosions* (2014).

[31] DÖRING, W. Über den Detonationsvorgang in Gasen. *Annalen der Physik 435*, 6 (1943), 421–436.

[32] DOROFEEV, S. Flame acceleration and explosion safety applications. *Proceedings of the Combustion Institute 33*, 2 (2011), 2161–2175.

[33] DOROFEEV, S., SIDOROV, V., DVOINISHNIKOV, A., AND BREITUNG, W. Evaluation of limits for effective flame acceleration in hydrogen mixtures. *Journal of Loss Prevention in the Process Industries 14*, 6 (2001), 583–589.

[34] DOROFEEV, S., SIDOROV, V., KUZNETSOV, M., MATSUKOV, I., AND ALEKSEEV, V. Effect of scale on the onset of detonations. *Shock Waves 10* (2000), 137–149.

[35] DOWDY, D., SMITH, D., TAYLOR, S., AND WILLIAMS, A. The use of expanding spherical flames to determine burning velocities and stretch effects in hydrogen/air mixtures. *Symposium (International) on Combustion 23*, 1 (1991), 325–332.

[36] DRISCOLL, J. Turbulent premixed combustion: flamelet structure and its effect on turbulent burning velocities. *Progress in Energy and Combustion Science 34*, 1 (2008), 91–134.

[37] DZIEMINSKA, E., AND HAYASHI, A. Auto-ignition and DDT driven by shock wave-boundary layer interaction in oxyhydrogen mixture. *International Journal of Hydrogen Energy 38*, 10 (2013), 4185–4193.

[38] EDER, A. *Brennverhalten schallnaher und überschall-schneller Wasserstoff-Luft Flammen*. PhD thesis, Technische Universität München, 2001.

[39] EGOLFOPOULOS, F., AND DIMOTAKIS, P. A comparative numerical study of premixed and non-premixed ethylene flames. *Combustion Science and Technology 162*, 1 (2001), 19–35.

[40] EINSTEIN, A. Die Grundlage der allgemeinen Relativitätstheorie. *Annalen der Physik 49*, 7 (1916), 769–822.

[41] ERPENBECK, J. Stability of steady-state equilibrium detonations. *The physics of Fluids 5*, 5 (1962), 604–614.

[42] ERTESVAG, I., AND MAGNUSSEN, I. The eddy dissipation turbulence energy cascade model. *Combustion Science and Technology 159*, 1 (2000), 213–235.

[43] ETTNER, F. *Effiziente Numerische Simulation des Deflagrations-Detonations-Übergangs*. PhD thesis, Technische Universität München, 2013.

[44] EXPLOSION DYNAMICS LABORATORY. Shock and detonation toolbox. Last accessed May 20, 2021. https://shepherd.caltech.edu/EDL/PublicResources/sdt/.

[45] FAVRE, A. Equations des gaz turbulents compressibles. *J. de Mecanique 4*, 3 (1965), 361–390.

[46] FERZIGER, J., AND PERIC, M. *Computational methods for fluid dynamics*. McGraw-Hill, 2012.

[47] FUREBY, C. Towards the use of large eddy simulation in engineering. *Progress in Aerospace Sciences 44*, 6 (2008), 381–396.

[48] GAMEZO, V., DESBORDES, D., AND ORAN, E. Two-dimensional reactive flow dynamics in cellular detonation waves. *Shock Waves 9* (1999), 11–17.

[49] GARNIER, E., ADAMS, N., AND SAGAUT, P. *Large eddy simulation for compressible flows*. Springer, 2009.

[50] GEHRKE, B., WEILAGE, I., GULDEN, V., AND INGWERSEN, K. Branchenanalyse Chemieindustrie. *Hans Böckler Stiftung* (2018).

[51] GELFAND, B. E., SILNIKOV, M. V., MEDVEDEV, S. P., AND KHOMIK, S. V. *Thermo-gas dynamics of hydrogen combustion and explosion*. Springer Science and Business Media, 2012.

[52] GERLINGER, P. *Numerische Verbrennungssimulation*. Springer, 2005.

[53] GEXCON. Fire and explosion safety consultants. Last accessed August 2, 2021. https://www.gexcon.com/.

[54] GIFFORD, M. *The role of hot-spots in the ignition and growth of explosion*. PhD thesis, Cambridge University, 2000.

[55] GOLOVITVHEV, V., NORDIN, N., JARNICKI, R., AND CHOMIAK, J. 3-D diesel spray simulations using a new detailed chemistry turbulent combustion model. *Society of Automotive Engineers Transactions 109*, 4 (2000), 1391–1405.

[56] GONZALEZ, M., BORGHI, R., AND SAOUAB, A. Interaction of a flame front with its self-generated flow in an enclosure. *Combustion and Flame 88*, 2 (1992), 201–220.

[57] GOODWIN, D., SPETH, R., MOFFAT, H., AND WEBER, B. Cantera: an object-oriented software toolkit for chemical kinetics, thermodynamics and transport processes. Last accessed June 10, 2021. https://www.cantera.org.

[58] GOULIER, J., COMANDINI, A., HALTER, F., AND CHAUMEIX, N. Experimental study on turbulent expanding flames of lean hydrogen/air mixtures. *Proceedings of the Combustion Institute 36*, 2 (2017), 2823–2832.

[59] HAN, W., GAO, Y., AND LAW, C. Flame acceleration and deflagration-to-detonation transition in micro- and macro-channels: an integrated mechnistic study. *Combustion and Flame 176* (2017), 285–298.

[60] HAN, W., WANG, C., AND LAW, C. Numerical simulation on mechanism of flame acceleration and deflagration to detonation transition for ethylene-oxygen system. *Proceedings of the 25th International Colloquium on the Dynamics of Explosions and Reactive Systems* (2015).

[61] HASSAN, M., AUNG, K., KWON, O., AND FAETH, G. Properties of laminar premixed hydrocarbon/air flames at various pressures. *Journal of Propulsion and Power 14*, 4 (1998).

[62] HASSLBERGER, J. *Numerical simulation of deflagration-to-detonation transition on industry Scale*. PhD thesis, Technische Universität München, 2017.

[63] HAWKES, E., SANKARAN, R., AND CHEN, J. Estimates of three-dimensional flame surface density and every term in its transport equation from two-dimensional measurements. *Proceedings of the Combustion Institute 33*, 1 (2011), 1447–1454.

[64] HE, L. A scaling analysis of the critical conditions for a deflagration-to-detonation transition. *Combustion Theory and Modelling 4*, 2 (2000), 107–122.

[65] HIRSCHFELDER, J., CURTISS, C., AND BIRD, R. *Molecular theory of gases and liquids*. John Wiley and Sons, Inc, 1948.

[66] HUO, J., SHU, T., REN, Z., AND LAW, C. Extrapolation of laminar ethylene/air flame speeds at elevated pressures with flame chemistry analysis. *Journal of Propulsion and Power 35*, 2 (2018).

[67] IACCARINO, G., ODOI, A., DURBIN, P., AND BEHNIA, M. Reynolds averaged simulation of unsteady separated flow. *International Journal of Heat and Fluid Flow 24*, 2 (2003), 147–156.

[68] ISSA, R. Solution of the implicitly discretised fluid flow equations by operator-splitting. *Journal of Computational Physics 62*, 1 (1986), 40–65.

[69] IVANOV, M., KIVERIN, A., AND LIBERMAN, M. Flame acceleration and DDT of hydogen-oxygen gaseous mixtures in channels with no-slip walls. *International Journal of Hydrogen Energy 36*, 13 (2011), 7714–7727.

[70] IVANOV, M., KIVERIN, A., YAKOVENKO, I., AND LIBERMAN, M. Hydrogen-oxygen flame acceleration and deflagration-to-detonation transition in three-dimensional rectangular channels with no-slip walls. *International Journal of Hydrogen Energy 38*, 36 (2013), 16427–16440.

[71] JASAK, H. Numerical solution algorithms for compressible flow. Lecture notes 2006, University of Zagreb. Last accessed November 17, 2021. https://1library.net/document/z1v1xmdz-numerical-solution-algorithms-for-compressible-flows.html.

[72] JO, Y., AND CROWL, D. Explosion characteristics of hydrogen-air mixtures in a spherical vessel. *Process Safety Progress 29*, 3 (2009), 216–223.

[73] JOMAAS, G., ZHENG, X., ZHU, D., AND LAW, C. Experimental determination of counterflow ignition temperatures and laminar flame speeds of c2-c3 hydrocarbons at atmospheric and elevated pressures. *Proceedings of the Combustion Institute 30*, 1 (2005), 193–200.

[74] JONES, W., AND LAUNDER, B. The prediction of laminarization with a two-equation model of turbulence. *International Journal of Heat and Mass Transfer 15*, 2 (1972), 301–314.

[75] JONES, W., AND LAUNDER, B. Ten years of industrial experience with the SST model. *Turbulence, Heat and Mass Transfer 4* (2003), 625–632.

[76] JOUGUET, E. Sur la propagation des reactions chmiques dans les gaz. *Journal de Mathematiques Pures et Appliquees 2* (1905), 5–86.

[77] KATZY, P. *Combustion model for the computation of flame propagation in lean hydrogen-air mixtures at low turbulence.* PhD thesis, Technische Universität München, 2020.

[78] KIM, W., MOGI, T., KUWANA, K., AND DOBASHI, R. Self-similar propagation of expanding spherical flames in large scale gas explosions. *Proceedings of the Combustion Institute 35*, 2 (2015), 2051–2058.

[79] KLEIN, R., BREITUNG, W., COE, I., HE, L., OLIVIER, H., REHM, W., AND STUDER, E. Models and criteria for prediction of deflagration-to-detonation transition (DDT) in hydrogen-air steam systems under severe accident conditions. *Forschungszentrum Jülich* (2000).

[80] KOLMOGOROV, A. Local structure of turbulence in incompressible visous fluid at very large reynolds number. *Doklady Akademiya Nauk SSSR 30* (1941).

[81] KOLMOGOROV, A. A refinement of previous hypotheses concerning the local structure in turbulence in viscous incompressible fluid at high reynolds number. *Journal of Fluid Mechanics 13*, 1 (1962), 82–85.

[82] KRISTENSEN, T. A factual clarification and chemical-technical reassessment of the 1921 Oppau explosion disaster - the unforeseen explosivity of porous ammonium sulfate nitrate fertilizer. *Norwegian Defence Research Establishment, FFI Rapport 16* (2016).

[83] KRIVOSHEYEV, P., PENYAZKOV, O., AND SAKALOU, A. Analysis of the final stage of flame acceleration and the onset of detonation in a cylindrical tube using high-speed stereoscopic imaging. *Combustion and Flame 216* (2020), 146–160.

[84] KUDRIAKOV, S., DABBENE, F., STUDER, E., AND ET. AL. The Tonus CFD code for hydrogen risk analysis: physical models, numerical schemes and validation matrix. *Nuclear Engineering and Design 238*, 3 (2008), 551–565.

[85] KUMAR, K., MITTAL, G., SUNG, C., AND LAW, C. An experimental investigation of ethylene/o2/diluent mixtures: laminar flame speeds with preheat and ignition delays at high pressures. *Combustion and Flame 153*, 3 (2008), 343–354.

[86] KUZNETSOV, M., ALEKSEEV, V., MATSUKOV, I., AND DOROFEEV, S. DDT in a smooth tube filled with a hydrogen-oxygen mixture. *Shock Waves 14* (2005), 205–215.

[87] KUZNETSOV, M., LIBERMAN, M., AND MATSUKOV, I. Experimental study of the preheat zone formation and deflagration to detonation transition. *Combustion Science and Technology 182*, 11-12 (2010), 1628–1644.

[88] LANEY, C. *Computational gasdynamics*. Cambridge University Press, 1998.

[89] LAW, C. *Combustion physics*. Cambridge University Press, 2006.

[90] LEE, J. *The detonation phenomenon*. Cambridge University Press, 2008.

[91] LI, X., FU, D., MA, Y., AND LIANG, X. Direct numerical simulation of compressible turbulent flows. *Acta Mechnanica Sinica 26*, 6 (2010), 795–806.

[92] LUO, Z., YOO, C., RICHARDSON, E., CHEN, J., LAW, C., AND LU, T. Chemical explosive mode analysis for a turbulent lifted ethylene jet flame in highly-heated coflow. *Combustion and Flame 159*, 1 (2012), 265–274.

[93] MENTER, F. Two-equation eddy-viscosity turbulence models for engineering applications. *AIAA Journal 32*, 8 (1994), 1598–1605.

[94] MENTER, F., AND ESCH, T. Elements of industrial heat transfer predictions. In *16th Brazilian Congress of Mechanical Engineering (COBEM)* (2001).

[95] MICHEL, J.-B., COLIN, O., AND ANGELBERGER, C. On the formulation of species reaction rates in the context of multi-species CFD codes using complex chemistry tabulation techniques. *Combustion and Flame 157*, 4 (2010), 701–714.

[96] MIDDHA, P., AND HANSEN, O. Predicting deflagration to detonation transition in hydrogen explosions. *American Institute of Chemical Engineers Process Safety Progress 27*, 3 (2007), 192–204.

[97] MUPPALA, S., ALURI, N., DINKELACKER, F., AND LEIPERTZ, A. Development of an algebraic reaction rate closure for the numerical calculation of turbulent premixed methane, ethylene and propane/air flames for pressures up to 1.0 MPa. *Combustion and Flame 140*, 4 (2005), 257–266.

[98] NOLL, B., SCHÜTZ, H., AND AIGNER, M. Numerical simulation of high-frequency flow instabilities near an airblast atomizer. *ASME Turbo Expo, New Orleans*, 2001-GT-0041, V002T02A008 (2001).

[99] O'CONAIRE, M., CURRAN, H., SIMMIE, J., PITZ, W., AND WESTBROOK, C. A comprehensive modeling study of hydrogen oxidation. *International Journal of Chemical Kinetics 36*, 11 (2004), 603–622.

[100] OPENFOAM. User guide. Last accessed August 9, 2021. https://cfd.direct/openfoam/user-guide/.

[101] ORAN, E., AND GAMEZO, V. Origins of the deflagration-to-detonation transition in gas-phase combustion. *Combustion and Flame 148*, 1-2 (2007), 4–47.

[102] ORAN, E., AND KHOKHLOV, A. Deflagrations, hot spots and the transition to detonation. *Philosophical Transactions of the Royal Society of London A 357*, 1764 (1999), 3539–3551.

[103] PATANKAR, S. *Numerical heat transfer and fluid flow*. Taylor and Francis, 1980.

[104] PENG-KÄRRHOLM, F. *Numerical modelling of diesel spray injection, turbulence interaction and combustion*. PhD thesis, Chalmers University of Technology, 2008.

[105] PETERS, N. The turbulent burning velocity for large-scale and small-scale turbulence. *Journal of Fluid Mechanics 384* (1999), 107–132.

[106] PETERS, N. *Turbulent combustion*. Cambridge University Press, 2000.

[107] POLING, B., PRAUSNITZ, J., O'CONNELL, J., AND ET AL. *The properties of gases and liquids*, vol. 5. McGraw-Hill New York, 2001.

[108] POPE, S. PDF methods for turbulent reactive flows. *Progress in Energy and Combustion Science 11*, 2 (1985), 119–192.

[109] POPE, S. *Turbulent flows*. IOP Publishing, 2001.

[110] QIAO, L., KIM, C., AND FAETH, G. Suppression effects of diluents on laminar premixed hydrogen/oxygen/nitrogen flames. *Combustion and Flame 143*, 1-2 (2005), 79–96.

[111] RADE, L., AND WESTERGREN, B. *Springers Mathematische Formeln*, 3 ed. Springer, 1995.

[112] SALAMANDRA, G., BAZHENOVA, T., AND NABOKO, I. Formation of detonation wave during combustion of gas in combustion tube. *Symposium (International) on Combustion 7*, 1 (1958), 851–855.

[113] SCHELKIN, K. Occurrence of detonation in gases in rough-walled tubes. *Soviet J. Tech. Phys. 17*, 5 (1947).

[114] SCHILDBERG, H.-P. The course of the explosions of combustible/o2/n2 mixtures in vessel-like geometry. *Forschung im Ingenieurwesen 73*, 1 (2009), 33–65.

[115] SCHILDBERG, H.-P. Experimental determination of the static equivalent pressures of detonative explosions of stoichiometric h2/o2/n2-mixtures in long and short pipes. *Proceedings of the ASME 2015 Pressure Vessels and Piping Conference*, PVP2015-45286 (2015).

[116] SCHILDBERG, H.-P. Experimental determination of the static equivalent pressures of detonative explosions of ethylene/o2/n2-mixtures and cyclohexane/o2/n2-mixtures in long and short pipes. *Proceedings of the ASME 2018 Pressure Vessels and Piping Conference*, PVP2018-84493 (2018).

[117] SCHILDBERG, H.-P., AND EBLE, J. Experimental determination of the static equivalent pressures of detonative explosions of cyclohexane/o2/n2-mixtures in long and short pipes (part 1 of 3). *Chemical Engineering Transactions 77* (2019), 1045–1050.

[118] SCHILDBERG, H.-P., AND EBLE, J. Experimental determination of the static equivalent pressures of detonative explosions of cyclohexane/o2/n2-mixtures in long and short pipes (part 2 of 3). *Chemical Engineering Transactions 77* (2019), 1051–1056.

[119] SCHILDBERG, H.-P., AND EBLE, J. Experimental determination of the static equivalent pressures of detonative explosions of cyclohexane/o2/n2-mixtures in long and short pipes (part 3 of 3). *Chemical Engineering Transactions 77* (2019), 1057–1062.

[120] SCHLICHTING, H., AND GERSTEN, K. *Boundary-layer theory*. Springer, 2017.

[121] SPALDING, D. Mixing and chemical reaction in steady confined turbulent flames. *Symposium (International) on combustion 13*, 1 (1971).

[122] SPERBER, A., SCHILDBERG, H.-P., AND SCHLEHLEIN, S. Dynamic load on a pipe caused by acetylene detonations - experiments and theoretical approaches. *Shock and Vibration 6*, 1 (1999), 29–43.

[123] SPIEGEL. Verletzte und Vermisste bei Vorfällen in BASF-Werken. Last accessed July 14, 2021. https://www.spiegel.de/panorama/basf-mehrere-verletzte-bei-verpuffung-und-explosion-in-basf-werken-a-1116954.html.

[124] STUTTGARTER NACHRICHTEN. Explosionsunglück erschüttert BASF. Last accessed July 14, 2021. https://web.archive.org/web/20100730190203/http://content.stuttgarter-nachrichten.de/stn/page/1771827_0_9223_-vor-60-jahren-explosionsunglueck-erschuettert-basf.html.

[125] SUN, C., SUNG, C., HE, L., AND LAW, C. Dynamics of weakly stretched flames: quantitative description and extraction of global flame parameters. *Combustion and Flame 118*, 1-2 (1999), 108–128.

[126] T. POINSOT, D. V. *Theoretical and numerical combustion.* RT Edwards Inc., 2005.

[127] TAYLOR, G. The formation of a blast wave by a very intense explosion. *Philosophical Transactions of the Royal Society of London A 201*, 1065 (1950), 159–174.

[128] TAYLOR, S. *Burning velocity and the influence of flame stretch.* PhD thesis, University of Leeds, 1991.

[129] THIJE-BOONKKAMP, J. The conservation equations for reacting gas flow. *Eindhoven University of Technology* (1993).

[130] THOMAS, G. Some observations on the initiation and onset of detonation. *Philosophical Transactions of the Royal Society of London A 370*, 1960 (2012), 715–739.

[131] TORO, E., SPRUCE, M., AND SPEARES, W. Restoration of the contact surface in the HLLC riemann solver. *Shock Waves 4* (1994), 25–34.

[132] TSE, S., ZHU, D., AND LAW, C. Morphology and burning rates of expanding spherical flames in h_2/o_2 inert mixtures up to 60 atmospheres. *Proceedings of the Combustion Institute 28*, 2 (2000), 1793–1800.

[133] TURNS, S. *An introduction to combustion.* Springer, 1996.

[134] UMWELTBUNDESAMT. Zentrale Melde- und Auswertestelle für Störfälle und Störungen. Last accessed July 14, 2021. https://www.umweltbundesamt.de/themen/wirtschaft-konsum/anlagensicherheit/zentrale-melde-auswertestelle-fuer-stoerfaelle.

[135] VELIKORODNY, A., STUDER, E., KUDRIAKOV, S., AND BECCANTINI, A. Combustion modeling in large scale volumes using Europlexus code. *Journal of Loss Prevention in the Process Industries 35* (2015), 104–116.

[136] VERSTEEG, H., AND MALALASEKERA, W. *An indtrodution to computational fluid dynamics: the finite volume method.* Pearson, 2007.

[137] VON NEUMANN, J. *Theory of detonation waves.* John von Neumann, Collected Works. Macmillan, 1942.

[138] VYAZMINA, E., AND JALLAIS, S. Validation and recommendations for FLACS CFD and engineering approaches to model hydrogen vented explosions: effects of concentration, obstruction vent area and ignition position. *International Journal of Hydrogen Energy 41*, 33 (2016), 1–9.

[139] WELLER, H. The development of a new flame area combustion model using conditional averaging. *Technical Report, Thermo-Fluids Section Report TF/9307, Imperial College London* (1993).

[140] WELLER, H., MAROONEY, C., AND GOSMAN, A. A new spectral method for calculation of the time-varying area of a laminar flame in homogeneous turbulence. *Symposium (International) on Combustion 23*, 1 (1991), 629–636.

[141] WELLER, H., TABOR, G., JASAK, H., AND FUREBY, C. A tensorial approach to computational continuum mechanics using object-oriented techniques. *Computers in Physics 12*, 6 (1998), 620–631.

[142] WHITE, F., AND CORFIELD, I. *Viscous fluid flow*. McGraw-Hill, 2006.

[143] WIELAND, C., SCHARF, F., SCHILDBERG, H.-P., HOFERICHTER, V., EBLE, J., HIRSCH, C., AND SATTELMAYER, T. Efficient simulation of flame acceleration and deflagration-to-detonation transition in smooth pipes. *Journal of Loss Prevention in the Process Industries 71* (2021), 104504.

[144] WILCOX, D. *Turbulence modeling for CFD*. DCW Industries, 2006.

[145] WILKE, C. A viscosity equation for gas mixtures. *The journal of chemical physics 18*, 4 (1950), 517–519.

[146] WILKENING, H., AND HULD, T. An adaptive 3-D CFD solver for modeling explosions on large industrial environmental scales. *Nuclear Engineering and Design 149* (1999), 361–387.

[147] WILLIAMS, F. *Combustion theory*, vol. 2. Benjamin/Cummings, 1985.

[148] WU, C., AND LAW, C. On the determination of laminar flame speeds from stretched flames. *Symposium (International) on Combustion 20*, 1 (1985), 1941–1949.

[149] XIAO, H., MAKAROV, D., SUN, J., AND MOLKOV, V. Experimental and numerical investigation of premixed flame propagation with distorted tulip shape in a closed duct. *Combustion and Flame 159*, 4 (2012), 1523–1538.

[150] XIAO, J., BREITUNG, W., KUZNETSOV, M., AND ET. AL. Gasflow-MPI: a new 3-D parallel all-speed CFD code for turbulent dispersion and combustion simulations part II: first analysis of the hydrogen explosion in Fukushima Daiichi unit 1. *International Journal of Hydrogen Energy 42*, 12 (2017), 8369–8381.

[151] XIAO, J., KUZNETSOV, M., AND TRAVIS, J. Gasflow-MPI: a new 3-D parallel all-speed CFD code for turbulent dispersion and combustion simulations part I: models, verification and validation. *Internation Journal of Hydrogen Energy 42*, 12 (2017), 8346–8368.

[152] ZDF. Nach Explosion in Chempark Leverkusen: Drei weitere Tote geborgen. Last accessed July 30, 2021. https://www.zdf.de/nachrichten/panorama/chempark-leverkusen-explosion-polizei-100.html.

[153] ZELDOVICH, Y. On the theory of propagation of detonation in geseous systems. Translation from zhurnal eksperimental' noi i eoreticheskoi fiziki. Tech. rep., National Advisory Committee for Aeronautics, 1960.

[154] ZIMONT, V., POLIFKE, W., BETTELINI, M., AND WEISENSTEIN, W. An efficient computational model for premixed turbulent combustion at high reynolds numbers based on a turbulent flame speed closure. *Journal of engineering of gas turbines and power 120*, 3 (1998), 526–532.

A Appendix

A.1 Derivation of the Pressure Correction Equation

The derivation of the pressure correction equation (Eq. 3.37) follows the procedure for a laminar flow, as described in [46]. For reasons of compact notation, the laminar stress terms and the Reynolds Stresses from the Reynolds-averaged momentum equation (Eq. 3.22) are combined to an effective shear stress $\bar{\tau}_{ij,\,\mathrm{eff}}$, which can be formulated by incorporating Eq. 3.3 and Eq. 3.24

$$\bar{\tau}_{ij,\,\mathrm{eff}} = \bar{\tau}_{ij} - \bar{\rho}\,\widetilde{u_i'' u_j''} = \mu_{\mathrm{eff}}\left(\frac{\partial \widetilde{u}_i}{\partial x_j} + \frac{\partial \widetilde{u}_j}{\partial x_i} - \frac{2}{3}\delta_{ij}\frac{\partial \widetilde{u}_m}{\partial x_m}\right) - \frac{2}{3}\delta_{ij}\bar{\rho}k. \tag{A.1}$$

Accordingly, Eq. 3.22 can be rewritten as

$$\frac{\partial \bar{p}}{\partial x_i} = -\frac{\partial}{\partial x_j}\left(\bar{\rho}\,\widetilde{u}_i\widetilde{u}_j\right) + \frac{\partial \bar{\tau}_{ij,\mathrm{eff}}}{\partial x_j} + \bar{\rho}\widetilde{g}_i - \frac{\partial}{\partial t}\left(\bar{\rho}\,\widetilde{u}_i\right). \tag{A.2}$$

Applying the divergence operator on Eq. A.2 provides

$$\frac{\partial}{\partial x_i}\left(\frac{\partial \bar{p}}{\partial x_i}\right) = -\frac{\partial}{\partial x_i}\left[\frac{\partial}{\partial x_j}\left(\bar{\rho}\,\widetilde{u}_i\widetilde{u}_j - \bar{\tau}_{ij,\mathrm{eff}}\right)\right] + \frac{\partial\left(\bar{\rho}\widetilde{g}_i\right)}{\partial x_i} - \frac{\partial}{\partial x_i}\frac{\partial}{\partial t}\left(\bar{\rho}\,\widetilde{u}_i\right). \tag{A.3}$$

In addition, applying the temporal derivative on the continuity equation (Eq. 3.21)

$$\frac{\partial^2 \bar{\rho}}{\partial t^2} + \frac{\partial}{\partial t}\frac{\partial}{\partial x_i}\left(\bar{\rho}\,\widetilde{u}_i\right) = 0 \tag{A.4}$$

and Schwarz' theorem yields

$$\frac{\partial}{\partial x_i}\frac{\partial}{\partial t}\left(\bar{\rho}\,\widetilde{u}_i\right) = \frac{\partial}{\partial t}\frac{\partial}{\partial x_i}\left(\bar{\rho}\,\widetilde{u}_i\right). \tag{A.5}$$

Finally, the pressure correction equation can be derived from Eq. A.3 and Eq. A.4

$$\frac{\partial}{\partial x_i}\left(\frac{\partial \bar{p}}{\partial x_i}\right) = -\frac{\partial}{\partial x_i}\left[\frac{\partial}{\partial x_j}\left(\bar{\rho}\,\widetilde{u}_i\,\widetilde{u}_j - \bar{\tau}_{ij,\,\mathrm{eff}}\right)\right] + \frac{\partial\left(\bar{\rho}\,\widetilde{g}_i\right)}{\partial x_i} + \frac{\partial^2 \bar{\rho}}{\partial t^2}. \tag{A.6}$$

A.2 Coefficients for the Calculation of Unburnt Properties

The coefficients for the calculation of the species unburnt dynamic viscosity μ_i and the species unburnt thermal conductivity λ_i in Sec. 3.5.1.1 are listed in the following for stoichiometric $H_2/O_2/N_2$ and $C_2H_4/O_2/N_2$ mixtures.

A.2.1 $H_2/O_2/N_2$ Mixtures

Table A.1: Coefficients for the calculation of μ_i for $H_2/O_2/N_2$ mixtures.

Coefficient	H_2	O_2	N_2
C_1	-6.67979e-06	-4.310786e-05	-3.827945e-05
C_2	4.488563e-04	2.938155e-03	2.608715e-03
C_3	-1.132362e-02	-7.598193e-02	-6.734753e-02
C_4	0.3116929	1.068172	0.9651040
C_5	-14.29116	-16.76182	-16.43404

Table A.2: Coefficients for the calculation of λ_i for $H_2/O_2/N_2$ mixtures.

Coefficient	H_2	O_2	N_2
D_1	4.539177e-05	-3.693416e-05	-3.070967e-05
D_2	-3.331300e-03	6.371494e-04	1.994952e-03
D_3	9.983502e-02	-2.931303e-02	-2.920039e-02
D_4	-1.515643	5.784523e-01	1.338794e-01
D_5	11.76991	-5.000365	6.071041e-01
D_6	39.31307	11.53163	-9.539258

A.2.2 $C_2H_4/O_2/N_2$ Mixtures

Table A.3: Coefficients for the calculation of μ_i for $C_2H_4/O_2/N_2$ mixtures.

Coefficient	C_2H_4	O_2	N_2
C_1	-4.709413e-07	-1.18850e-05	-1.052915e-05
C_2	2.059828e-04	8.837941e-04	7.846824e-04
C_3	-1.321918e-02	-2.536152e-02	-2.249501e-02
C_4	4.317	1.068172	0.4227412
C_5	-15.05667	-13.9007	-13.83811

Table A.4: Coefficients for the calculation of λ_i for $C_2H_4/O_2/N_2$ mixtures.

Coefficient	C_2H_4	O_2	N_2
D_1	-5.508706e-05	-3.693416e-05	-3.070967e-05
D_2	4.215873e-03	6.371494e-04	1.994952e-03
D_3	-1.293698e-01	-2.931303e-02	-2.920039e-02
D_4	1.977737	5.784523e-01	1.338794e-01
D_5	-14.67813	-5.000365	6.071041e-01
D_6	37.42355	11.53163	-9.539258

A.3 Laminar Flame Speeds of C_2H_4/Air Mixtures

In order to validate the reaction mechanism of Lu [92] for C_2H_4/air and stoichiometric $C_2H_4/O_2/N_2$ mixtures, the prediction of laminar flame speeds is compared with experimental C_2H_4/air data. Fig. A.3 depicts the temperature influence, while the impact of pressure is analysed in Fig. A.3.

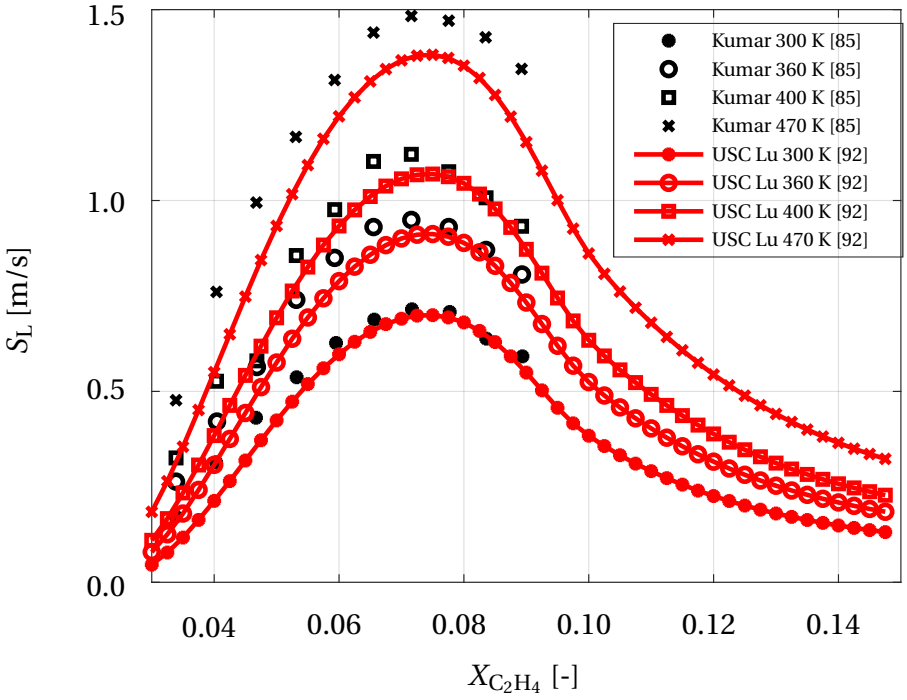

Figure A.1: Temperature influence on laminar flame speed of C_2H_4/air mixtures. Experimental data from Kumar [85]. Reaction mechanism of Lu [92] used for Cantera [57] calculations.

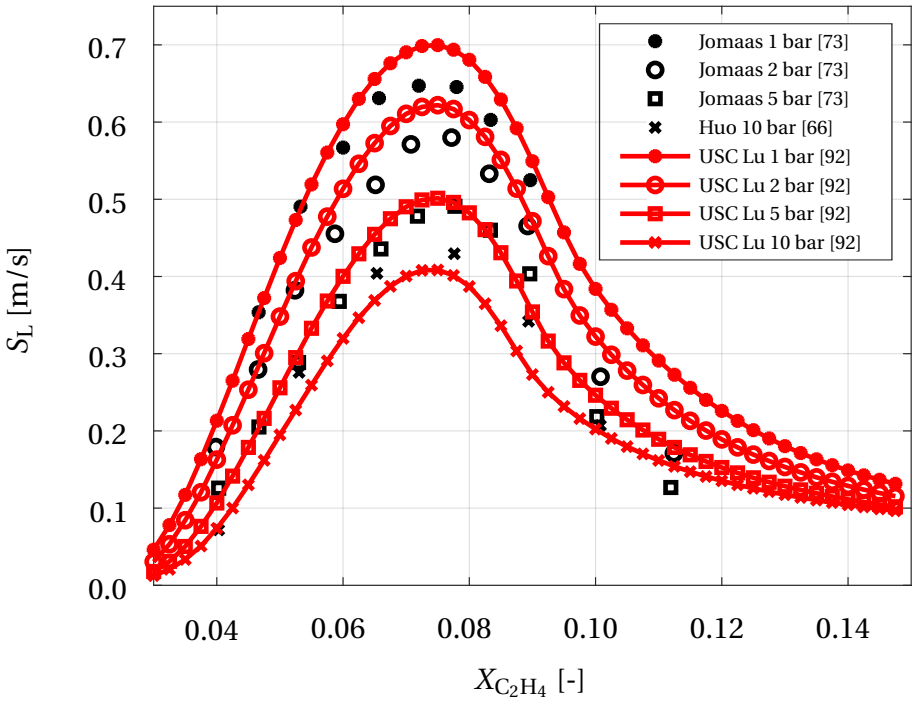

Figure A.2: Pressure influence on laminar flame speed of C_2H_4/air mixtures. Experimental data from Jomaas [73] and Huo [66]. Reaction mechanism of Lu [92] used for Cantera [57] calculations.

Previous Publications

Teile dieser Dissertation wurden vom Autor bereits vorab als Zeitschriftenbeitrag veröffentlicht oder sind noch als Konferenzbeitrag eingereicht. Alle Vorveröffentlichungen sind entsprechend der gültigen Promotionsordnung ordnungsgemäß gemeldet und anschließend aufgeführt. Sie sind deshalb nicht zwangsläufig im Detail einzeln referenziert. Vielmehr wurde bei der Referenzierung eigener Vorveröffentlichungen Wert auf Verständlichkeit und inhaltlichen Bezug gelegt.

Parts of this Ph.D. thesis have been published by the author beforehand in a journal paper or are currently submitted as a conference contribution. All of these prior printed publications are registered according to the valid doctoral regulations and listed below. Therefore, they are not necessarily quoted explicitly in the text. Whether they were referenced, depended on maintaining comprehensibility and providing all necessary context.

Wieland, C., Scharf, F., Schildberg, H.-P., Hoferichter, V., Eble, J., Hirsch, C., Sattelmayer, T., Efficient simulation of flame acceleration and deflagration-to-detonation transition in smooth pipes. *Journal of Loss Prevention in the Process Industries 71* (2021), 104504

Wieland, C., Hirsch, C., Sattelmayer, T., Scharf, F., Hoferichter, V., Schildberg, H.-P., Simulation of Flame Acceleration and Deflagration to Detonation Transition in Components of Chemical Plants. Submitted to 28th ICDERS 2022